The Changing Hydrology of Lhù'ààn Mān - Kluane Lake - under Past and Future Climates and Glacial Retreat

---

Centre for Hydrology Report No. 15

Youssef Loukili and John W Pomeroy
Centre for Hydrology, University of Saskatchewan
101-121 Research Drive, Saskatoon, Saskatchewan S7N 1K2

The Changing Hydrology of Lhù'ààn Mān - Kluane Lake - under Past and Future Climates and Glacial Retreat

---

Centre for Hydrology Report No. 15

Youssef Loukili and John W Pomeroy
Centre for Hydrology, University of Saskatchewan
101-121 Research Drive, Saskatoon, Saskatchewan S7N 1K2

November 30, 2018

Prepared for Government of Yukon, Yukon Community Services, Infrastructure Branch, Whitehorse, Yukon

Contact:
Distinguished Professor John Pomeroy
Director, Centre for Hydrology
University of Saskatchewan
101 – 121 Research Drive,
Saskatoon, Saskatchewan, Canada
S7N 1K2

john.pomeroy@usask.ca
www.usask.ca/hydrology

Table of Contents

Executive Summary

The diversion of the Slims River, Ä'äy Chù, headwaters due to the Kaskawulsh Glacier retreat is one of the most extraordinary and dramatic hydrological changes due to climate change observed in Canada in the 21st C. The Slims River flows north from the terminus of the Kaskawulsh Glacier to Kluane Lake, Lhù'àän Mān – the largest lake in Yukon – and receives most of its inflow from the glacier meltwaters. The Kaskawulsh Glacier has been retreating rapidly since at least the 1950s. In May 2016, this retreat permitted ponded meltwaters at its terminus to erode a new channel through an ice dam at the valley fork and flow eastwards through a 30-metre tall canyon towards the Kaskawulsh River. Since then, Kluane Lake has experienced lower peak summer water levels. This event was widely covered in the news and described by some as "river piracy", in that the meltwaters that used to flow northward into the White and Yukon Rivers towards the Bering Sea, were redirected eastward to feed the Alsek River, which discharges southward in the Gulf of Alaska.

This is not the first time that this diversion has happened. Partial and transient diversions of glacial meltwater from the Kaskawulsh Glacier into the Kaskawulsh River rather than to the Slims River occurred in 1953, 1967, 1970, and 1989, due to a combination of ice dynamics and glacial melt hydrology and hydraulics around the terminus (Bryan ,1972; Barnett, 1974 Johnson, 1986). Bryan (1972) asserted that "*If these diversions continue to happen, and if the headward erosion of the Kaskawulsh River is sufficient to pirate the Slims River system, then it is possible that the entire drainage system could be redirected in a manner described by Bostock*". Shugar et al. (2017) estimated a 99.5% probability that the Kaskawulsh Glacier retreat, which triggered the piracy, can be attributed to human-caused global warming.

The goal of this report is to estimate the variability and changes in the lake levels of Kluane Lake over the historical period and into the future climates of the 21st C, with and without the Kaskawulsh Glacier contribution. The study diagnoses the causes of variability of lake levels in the past and evaluates the impact of deglaciation on lake levels in the future in the context of climate change. The methods use a combination of weather data from observations and global climate models to drive a detailed glacio-hydrological prediction model, which calculates streamflows in the Slims River and other inflows to Kluane Lake, lake evaporation and outflows and then the lake level. Historical Kluane Lake levels during the 20th C and future lake levels under global warming projections for the rest of the 21st C were predicted - with and without the Kaskawulsh Glacier contribution to the Slims River. The Canadian glacio-hydrological water prediction model MESH, which couples the Canadian Land Surface Scheme with both surface and subsurface runoff on slopes and river routing, was used to model the hydrology of the Kluane Lake Basin for these predictions. The adjacent gauged Duke River Basin was also included in the model to provide opportunities to evaluate the model performance in this region against gauged streamflows. Model parameterisations of topography, land cover, glacier cover, soil type and runoff directions were made and used to set up the model on various sub-basins flowing into Kluane Lake, including the Slims River Basin.

In order to reproduce historical conditions back to the early 20th C, meteorological forcing inputs from the European Union "WATCH" Project meteorological dataset were used to drive

model runs for 1901-2001. Simulated snow regimes, lake levels and Kluane River flows were compared and calibrated to observations available from 1953 onwards. To compare lake levels and hydrology between recent climates and those expected from future climate change, MESH was driven by outputs from the Weather Research and Forecasting (WRF) atmospheric weather model at 4-km resolution, under 2000-2015 conditions and the RCP8.5 "business as usual" greenhouse gas emission scenario for 2085-2100. In all model runs, the lake levels and basin hydrology were calculated with and without the Kaskawulsh Glacier contribution.

Analysis of the modelling results shows that for all periods examined, winter/spring/fall lake levels are not strongly affected by diversion of the glacier meltwaters, but summer peak lake levels are reduced by 1.6 m on average, from the observed median 781.2 m a.s.l. (above sea level) to the predicted median 779.6 m a.s.l. This is consistent with recent lake level observations by Environment and Climate Change Canada. Model analysis for the previous century documents the natural variability of the lake, including a few short-term temporary diversions of glacier outflow from or to the Slims River caused by glacier hydrodynamics at its terminus.

Results show that lake levels are very sensitive to conditions at the outflow of the lake into the Kluane River as represented by the rating curve of the river. From 1995 to 2015 the estimated rating curve changed such that average lake levels dropped 0.25 m during open water conditions. This drop in water levels is due to degradation of the outflow channel of Kluane Lake at Kluane River. It is strongly recommended that regular measurement of this rating curve be re-established in the Kluane River so that future changes can be quantified.

MESH modelling scenarios for the 20th C show a substantial seasonal drop in Kluane Lake levels from June to October when the glacier discharge is excluded, reaching a maximum difference of 1.7 m during August from those lake levels calculated with the glacier outflows. In the absence of the glacier, median inflows to Kluane Lake via the Slims River drop from more than 350 $m^3 s^{-1}$ to around 60 $m^3 s^{-1}$ during the month of July. Without the glacier inputs, the modelled summer peaks in lake levels are lower and summer median levels reach barely 779.4 m using the most recent rating curve. MESH results for the early 21st C without the Kaskawulsh Glacier inputs are realistic for the current lake level regime, with minimum, median and maximum peak levels of 779.4, 779.65 and 780.5 m respectively using the most recent rating curve. Until a modern, regularly measured rating curve for Kluane Lake is produced and maintained, these results can be used as guidance for the expected levels and flows by local design and hydrology projects. Model results for the late 21st C under substantial climate change, provide similar Kluane Lake levels without the glacier contributions. The future projections predict a forward shift in timing of peak levels from July to early June but are otherwise not notably higher or lower than the current projections. Model analysis for the late 21st C shows that lake levels are not further reduced or increased by anticipated shifts in the climate of the region. However, as the future rating curve on the Kluane River is unknown, there is uncertainty in these results that could be reduced by resumption of streamflow discharge measurements and measurement of new rating curves on the Kluane River. There is no indication whatsoever from the modelling scenarios of the Kluane River going dry or the flow reversing from Kluane Lake up the Slims River and down

the Kaskawulsh River – under current and foreseeable conditions such events are highly improbable.

The results drawn from this study are intended to answer important questions posed by Kluane First Nation of Burwash Landing, residents of Destruction Bay and surrounding areas and Yukon Government on the history and the future of Kluane Lake levels. Furthermore, the study will help inform water management and infrastructure design around Kluane Lake, and other environmental and aquatic conservation and adaptation efforts in the region. While the models employed here represent the "state-of-the-art", there is uncertainty in the predictions. This uncertainty could be reduced in future prediction efforts by resuming Kluane River discharge measurements, which were discontinued in 1994.

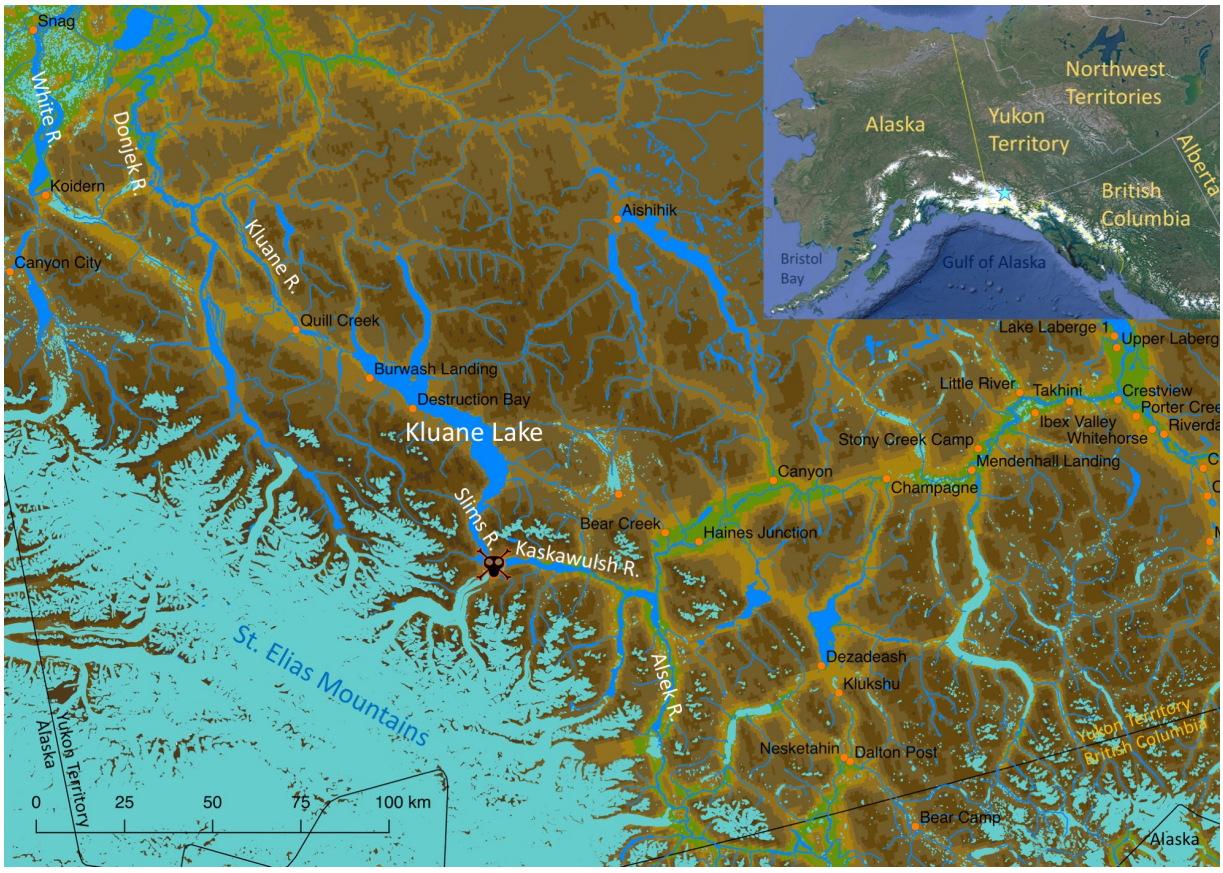

Figure 1. Location of Kluane Lake and piracy point.

List of Figures

List of Acronyms

C	Century
CaPA	Canadian Precipitation Analysis
CEC	Commission for Environmental Cooperation
CLASS	Canadian Land Surface Scheme
CRU	Climate Research Unit
DEM	Digital Elevation Model
ECCC	Environment and Climate Change Canada
ECMWF	European Centre for Medium-Range Weather Forecasts
EU	European Union
FAO	Food and Agriculture Organization
GEM	Global Environmental Multiscale model
GIS	Geographical Information Systems
GMTED2010	Global Multi-resolution Terrain Elevation Data 2010
GRU	Group Response Unit
HLSS	Hydrological Land Surface Scheme
LCCS	Land Cover Classification System
LSS	Land Surface Scheme
m a.s.l.	meters above sea level
MESH	Modélisation Environnementale Communautaire - Surface Hydrology
NALCMS	North American Land Change Monitoring System
NCAR	National Center for Atmospheric Research
NGA	National Geospatial-Intelligence Agency
NRCC	National Research Council Canada
NOAA	National Oceanic and Atmospheric Administration
NSF	National Science Foundation
PGC	Polar Geospatial Center
PGW	Pseudo Global Warming
RC	Rating Curve
RCP8.5	Representative Concentration Pathway 8.5
US	United States
USGS	United States Geological Survey
WATCH	Integrated Project Water and Global Change
WFD	WATCH Forcing Data
WRF	Weather Research and Forecasting

1. Introduction

1.1 Overview of the study and objectives

Changing climate has resulted in the rapid melt and retreat of the Kaskawulsh Glacier, diverting its flows southeast into the Alsek River Basin and away from the northward flowing Slims River and its contribution to Kluane Lake. Since May 2016, the Slims River has made a very small contribution of water to Kluane Lake (Figure 2). As a result of this and of lower mountain snowpack in the rest of the basin draining into Kluane Lake, lake levels dropped dramatically in summer 2016 from their historical normal levels. Since then, lake levels have not fully recovered and are now around 1.6 m below normal values in summer months. This drop is affecting the use of standing docks and harbours amongst other concerns. There is uncertainty as to the future lake level regime due to the lack of discharge from the Kaskawulsh Glacier to the Slims River and due to changing climate in the region as this influences runoff into the lake from its drainage basin (Figures 3, Table 1 and 2). These uncertainties leads to uncertainty in parameters for harbour and water access redesigns which are of interest to Yukon Community Services, Infrastructure Development Branch.

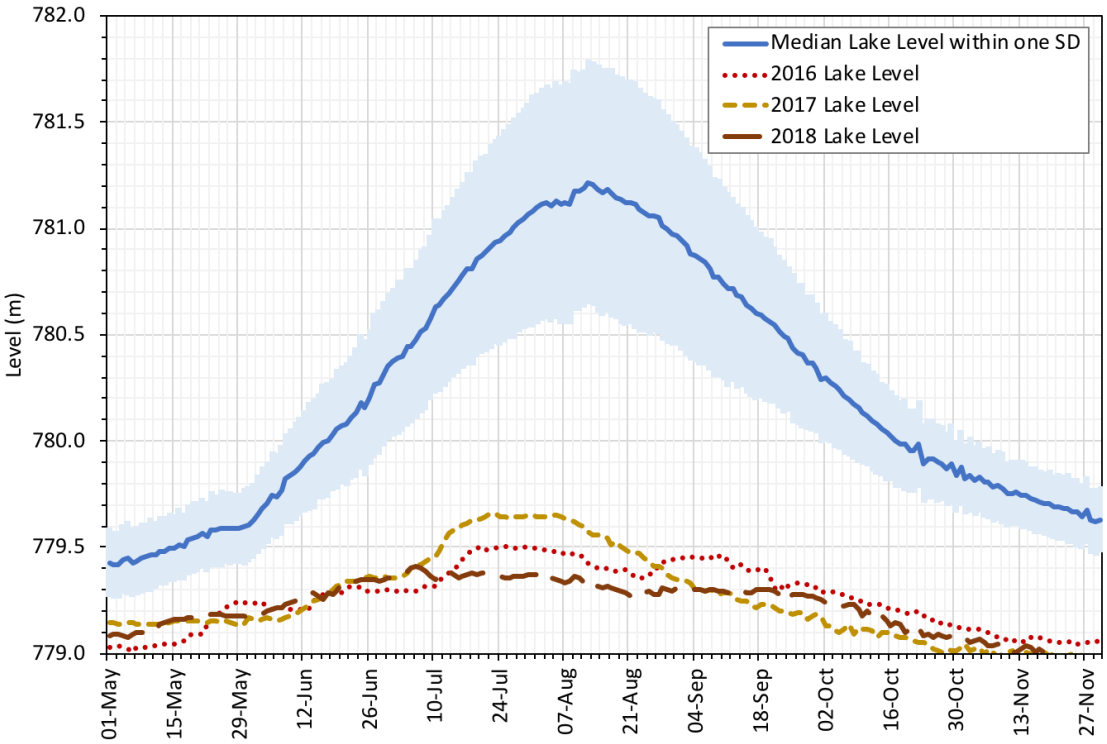

Figure 2. Water Survey of Canada measurements of lake levels for Kluane Lake near Burwash Landing (09CA001), showing the 63-year long-term (1953-2015) median lake level plotted within one standard deviation (shading) and stage measurements since 2016.

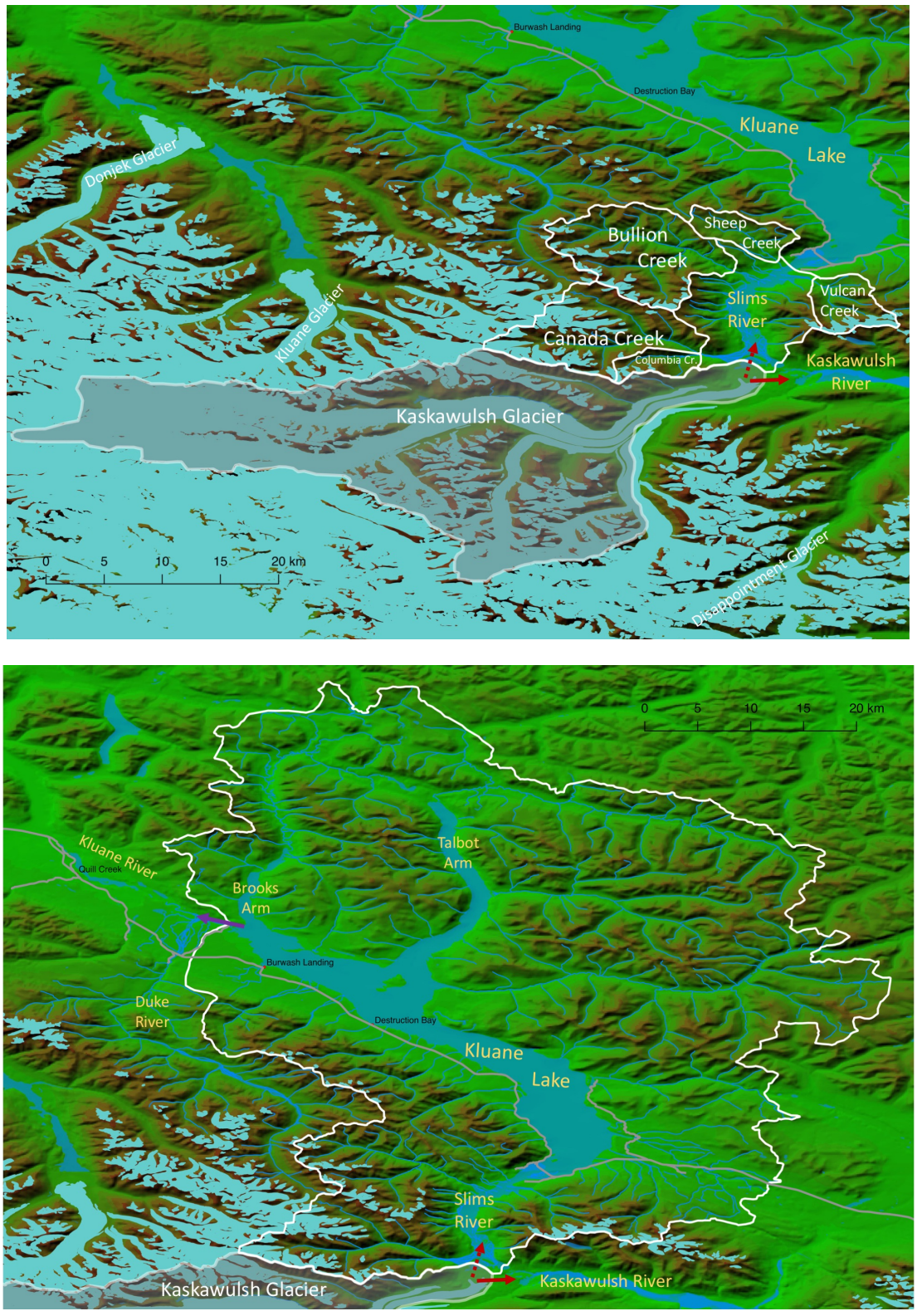

Figure 3. Top: Slims River Basin at Kluane Lake, showing sub-basins and the Kaskawulsh Glacier with red arrows showing former flow and current flow direction of discharge from the glacier. Bottom: Kluane Lake Drainage Basin showing the hydrography and topography.

Kluane Lake	432
Kaskawulsh Glacier	1,147
Slims River Basin with Glacier	1,778
Slims River Basin without Glacier	631
Kluane Lake Basin with Glacier	5,969
Kluane Lake Basin without Glacier	4,822
Duke River Basin	730

Table 1. Kluane Lake and drainage basin areas with and without Kaskawulsh Glacier (km^2).

Elevation bin (m a.s.l.)	Basin area with Glacier (km^2)	Basin area without Glacier (km^2)
700 – 800	542	542
800 – 1000	766	749
1000 – 1200	684	657
1200 – 1400	739	711
1400 – 1600	816	732
1600 – 1800	785	685
1800 – 2000	551	432
2000 – 2200	327	197
2200 – 2400	258	92
2400 – 2600	301	45
2600 – 2800	156	14
2800 – 3000	59	1
3000 – 3200	24	0
3200 – 3500	3	0

Table 2. Histogram table showing the lost drainage areas at different elevations.

The objectives of this study are to

i) Develop hydrological datasets for the Kluane Lake Basin, with and without Kaskawulsh Glacier contributions, under historical and future climate scenarios.
ii) Produce lake level estimates for Kluane Lake with and without the Kaskawulsh Glacier, under historical and future climate scenarios.
iii) Diagnose the mechanism(s) that have and will drive variations in lake levels, how they have changed historically and how they may change in the future, including an assessment of risk from future climate changes and droughts.

The methodology that this study employs is as follows.

Setup and parameterize a cold regions glacio-hydrological model, Environment Canada's MESH (Modélisation Environnementale communautaire - Surface Hydrology) model (Figure 4) on the Kluane Lake Basin (Figure 3), including the necessary cold regions processes (blowing snow, glacier melt, frozen soil infiltration, energy balance melt on slope/aspect). Parameterization included parameter selection, calibration and selection of process options within MESH. Parameter selection considered both high and low water stage simulations. The MESH setup for the Kluane Lake Basin is based upon advice from ECCC's National Hydrological Service and Yukon Environment's Water Resources Branch.

Run MESH on the Kluane Lake Basin using three different meteorological forcing datasets. MESH reproduces the water cycling and levels of Kluane Lake, including periods before hydrometric measurements began and into the future.

To reproduce historical conditions, MESH was run on Kluane Lake Basin using the European Union WATCH Project http://www.eu-watch.org/ meteorological dataset, which is available for the years 1901 to 2001. The model simulations of lake level were compared to existing lake level observations that are partially available since 1953. The causes of high and low lake levels over this period, with and without the Kaskawulsh Glacier were diagnosed.

To determine recent lake levels and hydrological variability, MESH was run on the Kluane Lake Basin driven by outputs from the US-NOAA Weather Research and Forecasting (WRF) atmospheric weather model, in recent historical mode from 2000 to 2015 for the current climate, with and without the Kaskawulsh Glacier. WRF outputs were downscaled using Centre for Hydrology empirical and physically based algorithms for distributing meteorological fields in complex terrain. WRF outputs were also bias corrected using multivariate quantile mapping against results of Environment and Climate Change Canada's (ECCC) GEM-CaPA model reanalysis product – GEM CaPA is considered the most reliable gridded meteorological dataset in North America as it is reset daily from observations to calculate the meteorological variables from atmospheric physics and the precipitation outputs are further corrected by assimilation of ground station, radar and satellite information. High and low lake level stages with and without the Kaskawulsh Glacier were calculated for the current climate.

To assess climate change impacts on lake level and hydrological variability, MESH is run on the Kluane Lake Basin using the WRF atmospheric weather model in Pseudo Global Warming (PGW) mode (2086-2100). The 4-KM WRF PGW meteorological outputs are dynamically downscaled from GCMs for a future climate condition equivalent to the end of the 21st C, using the business-as-usual RCP8.5 greenhouse gas emission scenario.

The results will show likely future lake levels without the Kaskawulsh Glacier and so indicate the vulnerability of the lake to future droughts and low flow situations as these will evolve under climate warming.

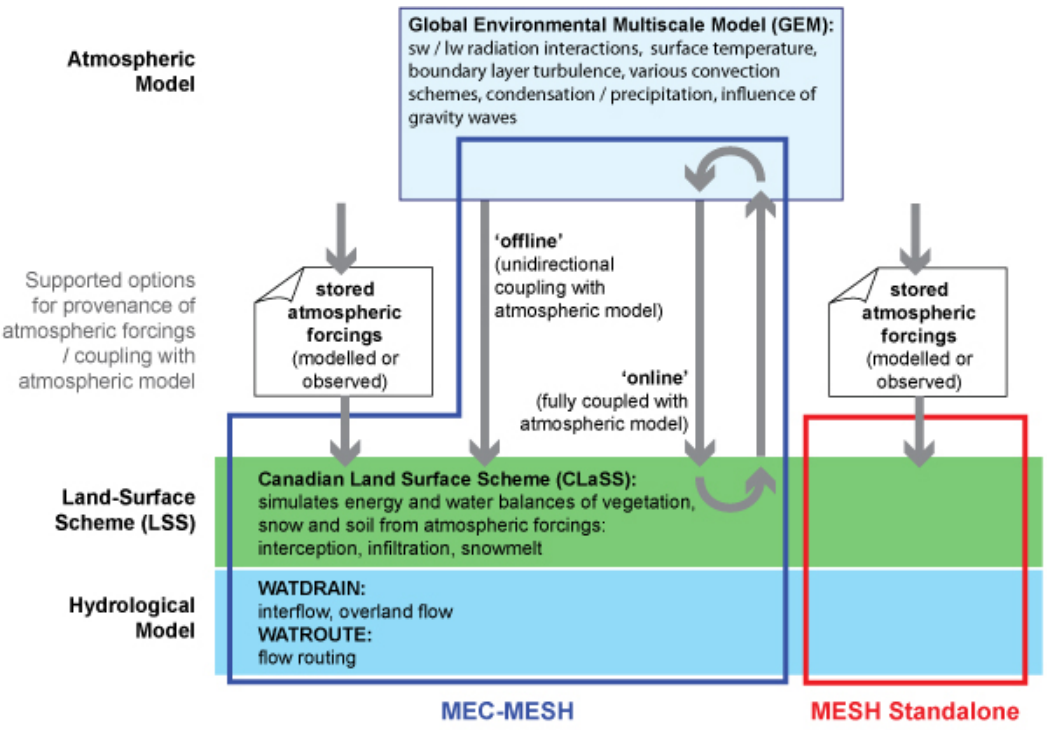

Figure 4. Conceptual diagram of Environment and Climate Change Canada's MESH (Modélisation Environnementale communautaire - Surface Hydrology) model. MESH Standalone is used when driven by WATCH or WRF atmospheric forcing data.

2. Hydrometric data and rating curves

2.1 Kluane Lake levels, outflows and inflows

The ECCC Water Survey of Canada started gauging Kluane Lake levels in December 1952 (Station 09CA001) using an assumed datum of 777.304 metres above sea level (m a.s.l.). There are missing levels between 1987 and 1992. These and missing higher levels in 1993 were reconstructed using a combination of two rating curves processed using 1986 and 1993 lake and Kluane River data. Daily water levels fluctuated between 1.7 and 4.6 m (779.0 and 781.9 m a.s.l.) (Figure 5 and 6). A trend analysis shows declining yearly mean levels which already dropped roughly 0.6 m from 1953 to the piracy year, 2016. These were mainly dropping due to lower minimum annual lake levels (in winter) – there is no trend in maximum summer lake levels (Figure 7).

Kluane River streamflow (discharge) was also gauged close to the lake outlet by the Water Survey of Canada between December 1952 to 1995 (Station 09CA002) and were deemed to properly represent the lake outflow. A rating curve derived from 1995 data (1995 RC in Figure 12) was used to reconstruct lake outflows after 1995. The range of daily outflow is from 0 to 455 m^3/s (Figure 8). Locations of the outflow, Kluane River gauging station 09CA002 and Kluane Lake level measurement station 09CA001 are shown in Figure 32.

A calculation of Kluane Lake inflows was carried out using a centred approximation of the storage conservation equation, where

$$A_{Lake}\ \Delta L / \Delta T = \text{Inflow} - \text{Outflow} \qquad (1)$$

Where A_{Lake} is the lake area, L is lake level and T is time. To ensure a reasonable stability, lake levels and stream outflows were conditioned here to their seven-day moving averages. Estimated inflows range between 0 and 720 m^3/s (Figure 9).

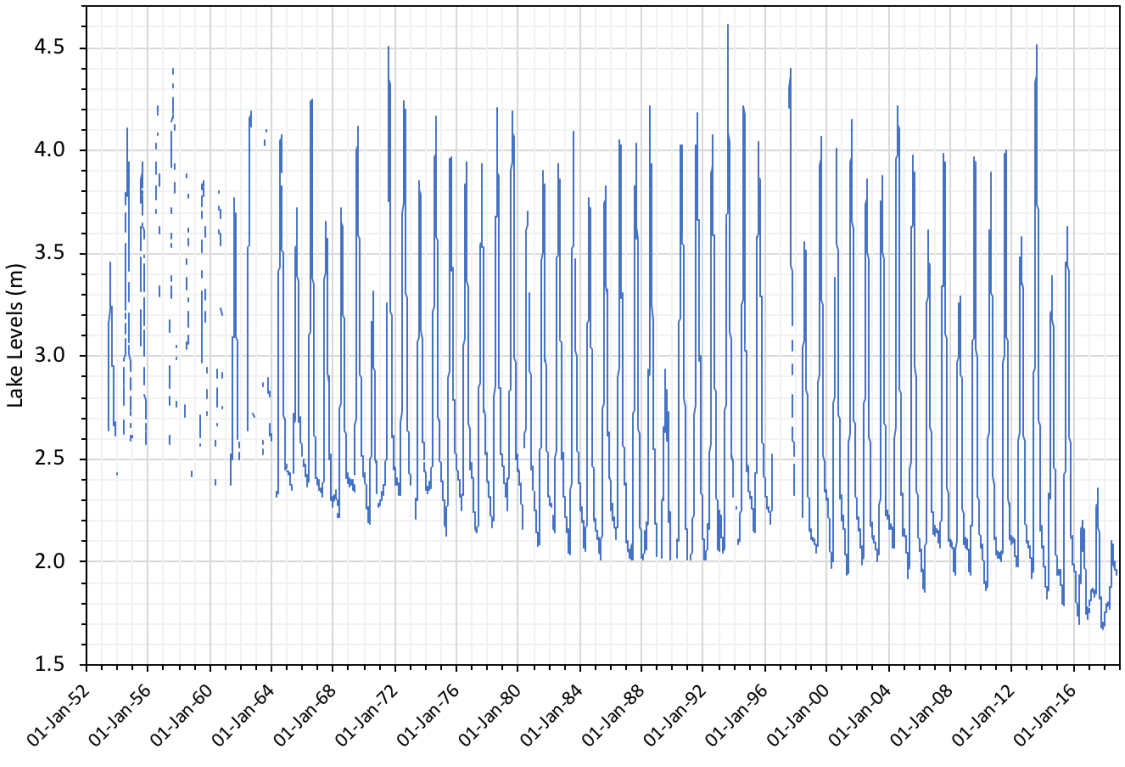

Figure 5. Kluane Lake observed lake levels for 1953-2018 (WSC Station 09CA001) – Datum 777.304 m.

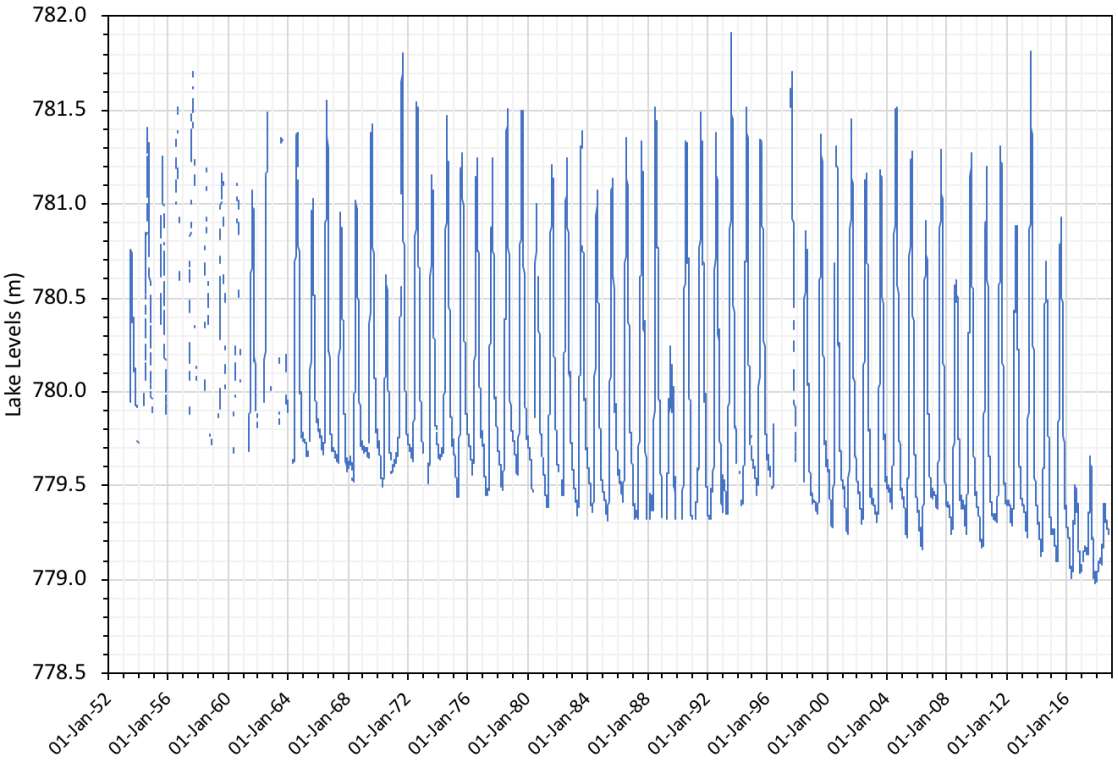

Figure 6. Kluane Lake observed lake levels (WSC Station 09CA001) m a.s.l.

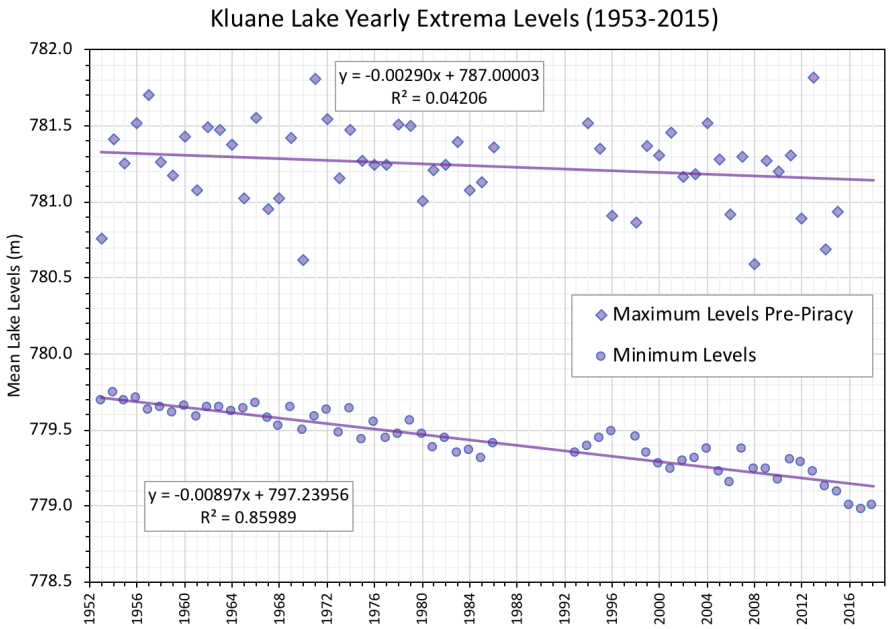

Figure 7. Kluane Lake yearly high and low levels.

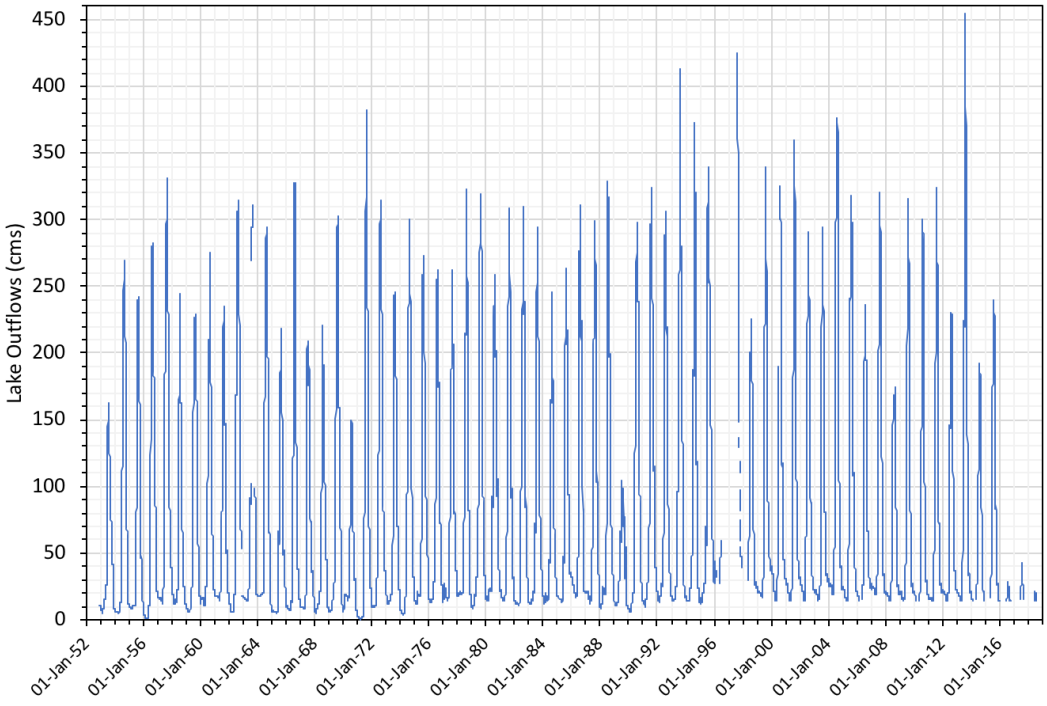

Figure 8. Observed and calculated (post-1995) flows in the Kluane River at the outlet of Kluane Lake.

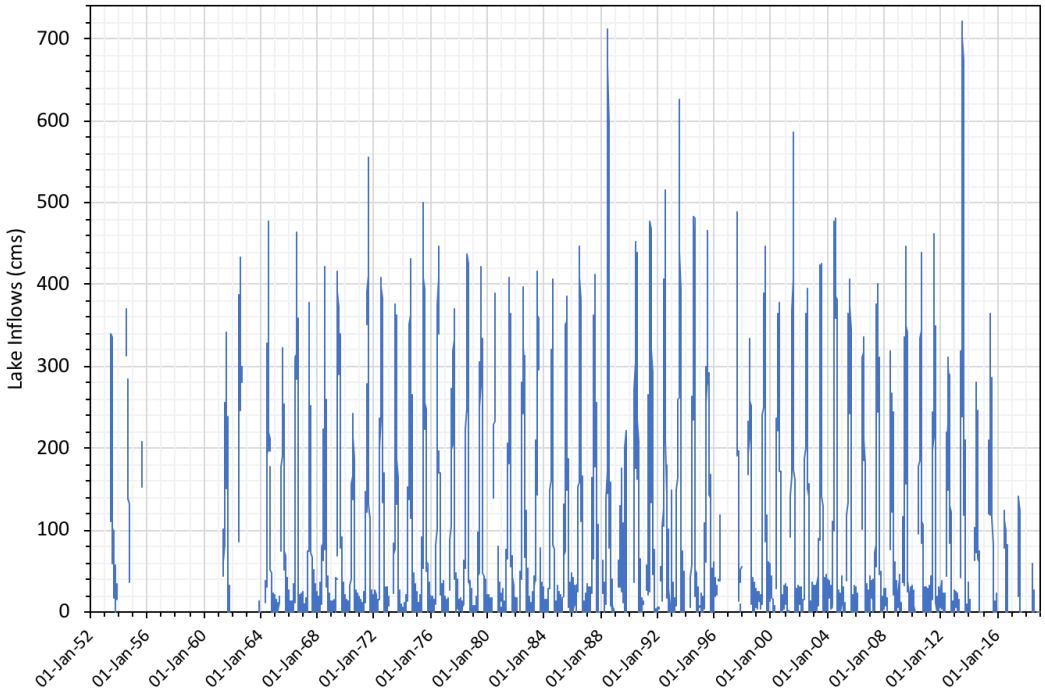

Figure 9. Kluane Lake calculated inflows.

2.2 Kluane Lake rating curves

Due to active sedimentation and evolving lake bed and stream channel patterns, the correspondence between lake levels and outflows as represented by the Kluane River rating curve has been changing yearly. Additionally, wind affected lake levels and freezing and thawing conditions around the lake outlet, not to mention sporadic gauging device or human errors and even geological activity, all contribute to the contrast and randomly scattered outliers in the observations used to develop the rating curves (RC). In this case, in order to contain this random variability, lake levels and outflows were smoothed by their seven-day averages to compile the Kluane Lake RC (Figure 10).

A detailed analysis of this data confirmed continuous shift of Kluane Lake RCs, indicating river bed and/or bank erosion at the outlet, and this is clearly visible in Figure 11. Hence, as shown in Figure 12, five RCs corresponding to various time periods were interpolated and extrapolated and used in MESH modeling in the case with the Kaskawulsh Glacier contributing to streamflow: Pre-1960s, 1960s, 1970s, 1980s and post-1980s (1995). In the MESH modelling case without the Kaskawulsh Glacier, two RCs were constructed: a slightly shifted Estimated Open Water 1995 RC to reproduce lake levels had the river piracy happened in the past century; and a post-1995 Estimated Open Water Current RC considering both the continuous shift and the most probable current and near-future flow situation under open water conditions.

As low summer lake levels are likely to prevail in the future and in order to reduce uncertainty in changing rating curves, it is suggested that future studies of lower lake levels be supported by resuming regular Kluane River discharge measurements and redevelopment of RCs.

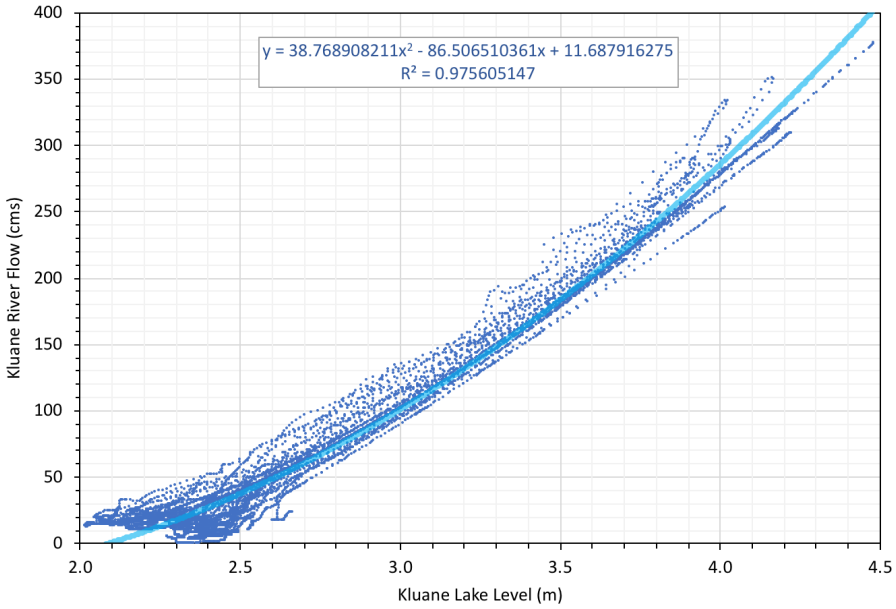

Figure 10. Measurements of lake level and river flow and the resulting best-fit Kluane Lake Rating Curve using 1953-95 data.

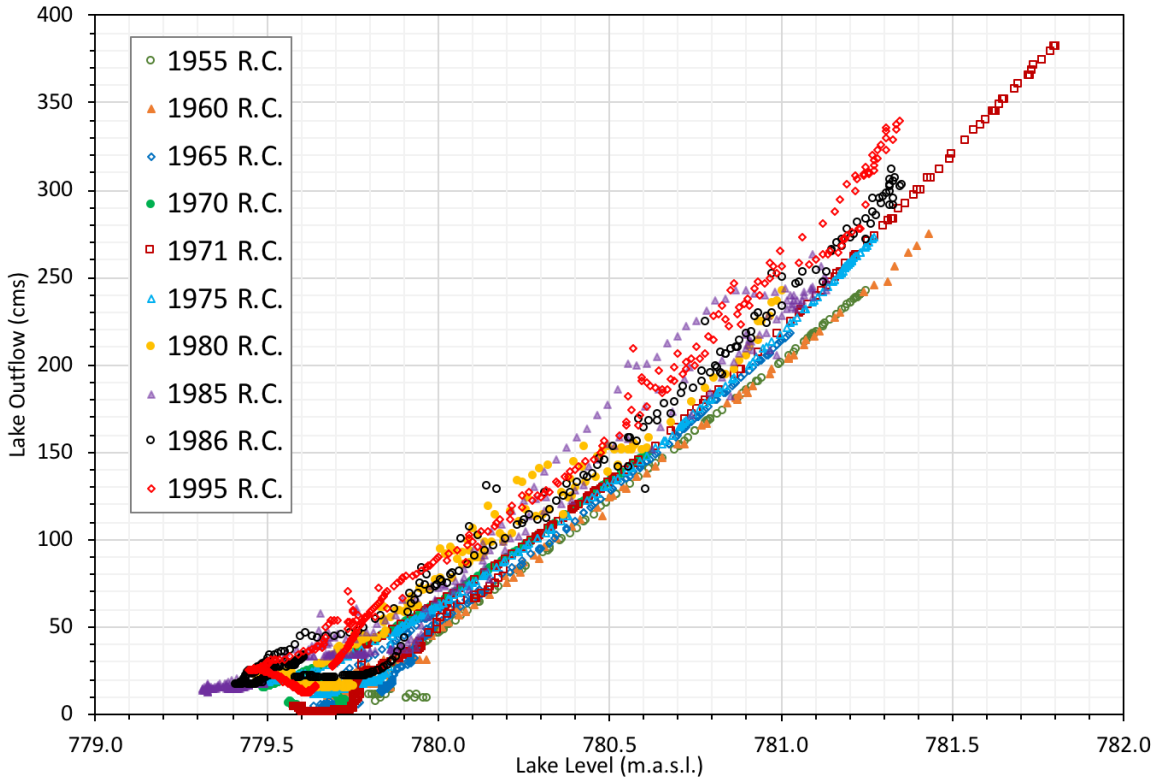

Figure 11. Evolving RCs of Kluane Lake from 1955 to 1995.

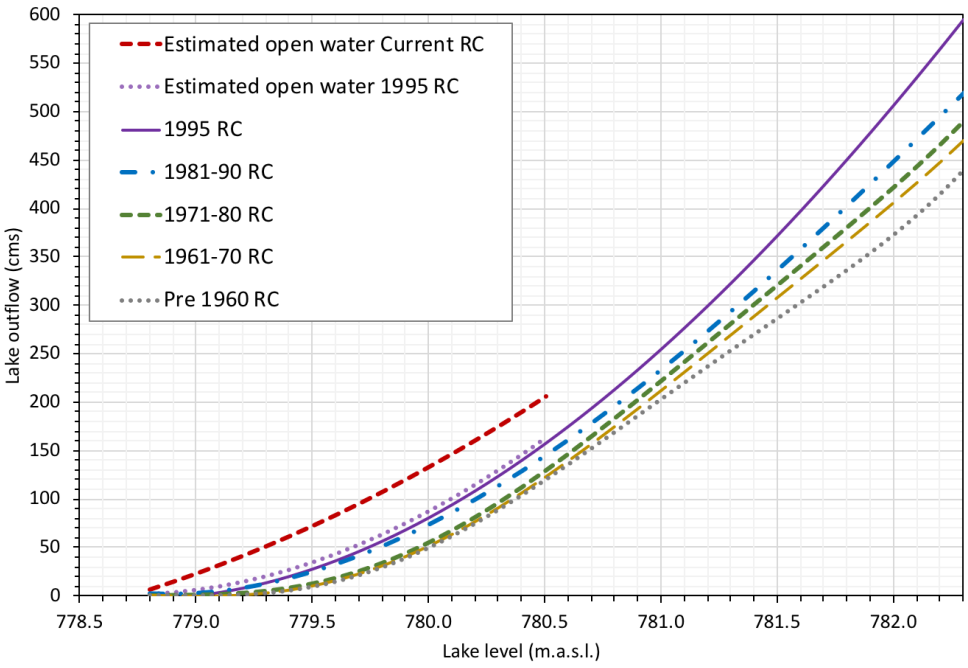

Figure 12. Kluane Lake Rating Curves used in MESH modeling.

2.3 Slims River flows

While numerous studies concentrated on suspended sediments in the Slims River and deposition in its delta confluence with Kluane Lake, only a few discharge measurements of the Slims River accompanied these studies. Table 1 summarizes most of this rare hydrometric information, where measurements in and prior to 1970 were reported by Bryan (1972), some of which are averaged here from two or three values reported for different times of the day. 1983 measurements were extracted from graphs in the work of Johnson (1986).

Year	Date	Reported discharge CFS	Reported discharge CMS	Reference
1955	25 May	873	24.72	Bryan 1972 (after Ramsden, personal communication 1970 and Fahnestock 1969
1962	27 Jun	6400	181.23	
	09 Aug	8890	251.74	
	16 Aug	11200	317.15	
	27 Sep	133	3.77	
1963	21 Feb	8	0.23	
	03 Jul	6330	179.25	
	07 Aug	9600	271.84	
1964	06 May	125	3.54	
	27 May	956	27.07	
1965	27 Jul	3750	106.19	
	28 Jul	4300	121.76	
	31 Jul	7550	213.79	
	08 Aug	9400	266.18	
	11 Aug	9900	280.34	
1970	30 Jun	3840	108.74	Barnett 1974
	05 Jul	4300	121.76	
	06 Jul	4900	138.75	
	08 Jul	5200	147.25	
	09 Jul	3639	103.05	
	15 Jul	6949	196.77	
	19 Jul	4000	113.27	
	20 Jul	4250	120.35	
	30 Jul	3961	112.16	
	04 Aug	730	20.67	
	05 Aug	870	24.64	
	06 Aug	868	24.58	
	07 Aug	725	20.53	
	08 Aug	860	24.35	
	12 Aug	601	17.02	
1983	17 Jun	6463	183	Johnson 1986
	18 Jun	6604	187	
	28 Jun	7240	205	
	29 Jun	7169	203	
	30 Jun	6780	192	
	01 Jul	6886	195	
	02 Jul	6886	195	

Table 3. Slims River discharge measurements.

3. Summary of meteorological data

Sited above 61°N in the rain shadow of the St. Elias Mountains, the Kluane Lake Basin has a dry, cold continental climate, mostly influenced by Arctic air masses. The long very cold winters in this region bring as little as four hours of daylight (not accounting for mountain shading), while the cool to warm summers have as long as 19 hours of daylight. Due to steep meteorological gradients towards the alpine glaciers, highly variable weather conditions prevail at higher elevations in all seasons. In this section, the general seasonal and annual patterns of precipitation and temperature over Kluane Lake region are reported and analyzed. There is a weather station at Burwash Airport with records dating back to 1966, and its observed data can be compared to that generated from the gridded surface weather forcings used to run MESH. The EU WATCH and WRF-GEM-CaPA precipitation and temperature summaries are rather representative of the basin averages, and they carry a strong imprint of the station data that was assimilated into their creation.

3.1 Burwash Landing station data (1967-2018)

The town of Burwash Landing, at historic Milepost 1093 on Alaska Highway, is located in the Shakwak Valley at the foothill of Kluane Ranges, along the northwestern shores of Kluane Lake. Burwash Airport weather station is run by ECCC and has a continuous record of meteorological variables since October 1966 (Table 2). These include daily minimum, mean and maximum temperatures, heat degree days, total rain, snow and precipitation, snow on the ground, and direction and speed of maximum gust. The Adjusted and Homogenized Canadian Climate Data (AHCCD) is an enhanced ECCC product which integrates a number of adjustments applied to the original station data to address shifts due to changes in instruments and in observing procedures. AHCCD is therefore considered a more reliable data source for climate research and climate change studies.

Station name	Burwash A	Burwash A	Burwash Airport Auto BC
Period of record	1966-2015	2012-18	2013-18
Latitude	61.37	61.37	61.37
Longitude	-139.05	-139.04	-139.02
Elevation (m .a.s.l.)	806.2	805.3	807
Climate Id.	2100182	2100181	2100184

Table 4. Detail of ECCC's meteorological stations at Burwash.

For filling some missing yearly precipitation data in Burwash AHCCD (1979, 1987, 2001-02, 2005, and 2009-17), a linear bias of the difference between station and AHCCD data is used

in these years to provide a complete yearly precipitation from 1967 to 2017 (Figure 13). The mean and median of yearly precipitation for this period of record are respectively 337 and 350 mm. The partitioning of precipitation into rainfall and snowfall is also displayed in Figure 14 for the period 1967-2013, and further analysis of the trends of proportions of type to total precipitation shows a decrease of snowfall from 40% to 35% compensated by an increase of rainfall from 60 to 65% during this period (Figure 15). This shift in precipitation phase is due to climate warming.

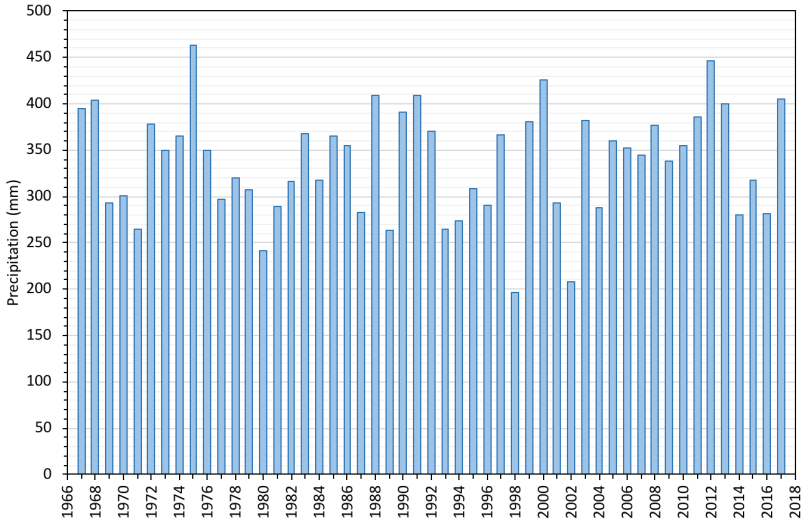

Figure 13. Burwash yearly total precipitation for 1967-2017 from AHCCD and bias corrected historical data.

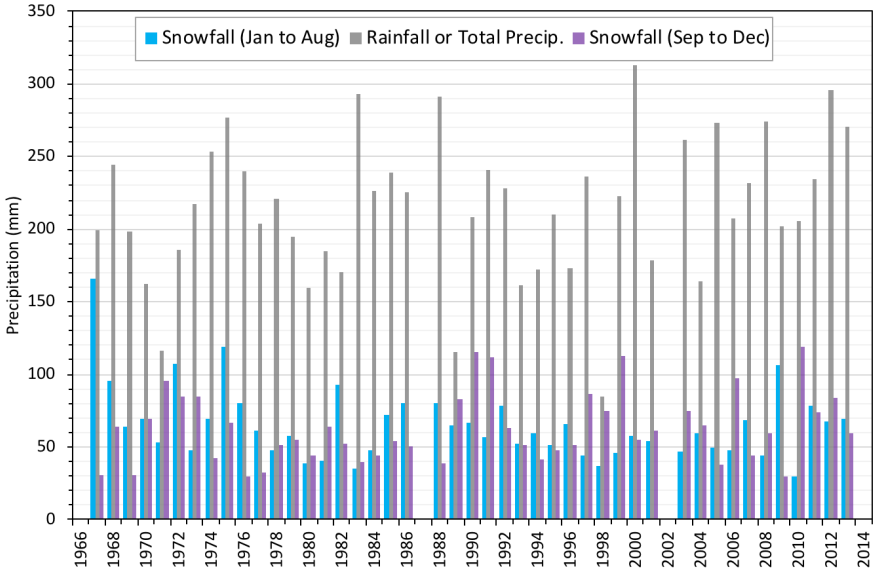

Figure 14. Burwash yearly precipitation partitioning for 1967-2013 from AHCCD and bias corrected historical data.

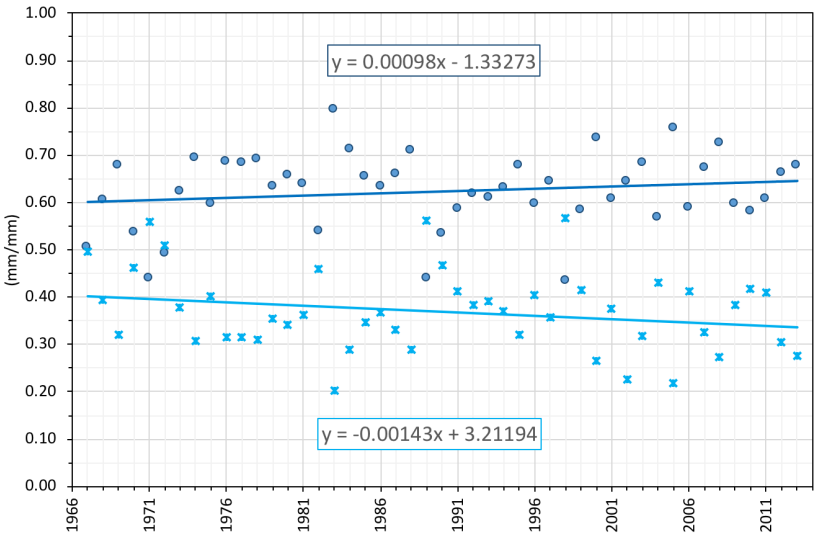

Figure 15. Burwash yearly proportions of rainfall and snowfall to total precipitation for 1967-2013 (AHCCD data).

The average AHCCD's climatological monthly temperatures for Burwash for 1967 to 2017 is shown in Figure 16. Winter temperatures are typical of the subarctic and vary between -28 and -15 °C in January, while cool summer temperatures range between 6 and 19 °C in August. Examination of AHCCD's seasonal means of homogenized daily maximum, minimum and mean surface air temperatures at Burwash (Figure 17) reveals that climate warming is causing the rainfall proportion to rise and is of a magnitude such that it is likely to be an important driver of glacial retreat. There is a substantial warming evident in the region over the past fifty years. The observed trends indicate that since 1967, winter, spring and summer temperatures have increased by 5.0 °C, 1.0 °C and 1.5 °C respectively. Autumn minimum temperatures also showed a smaller increase of 0.7 °C.

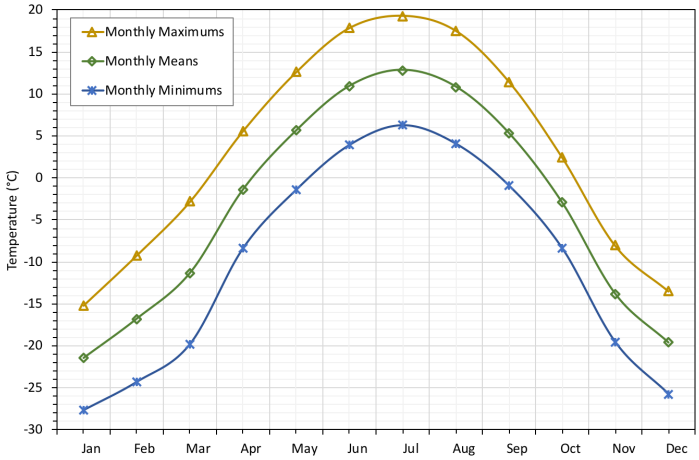

Figure 16. Mean, minimum and maximum monthly mean temperatures for Burwash Airport for 1967-2017 (AHCCD data).

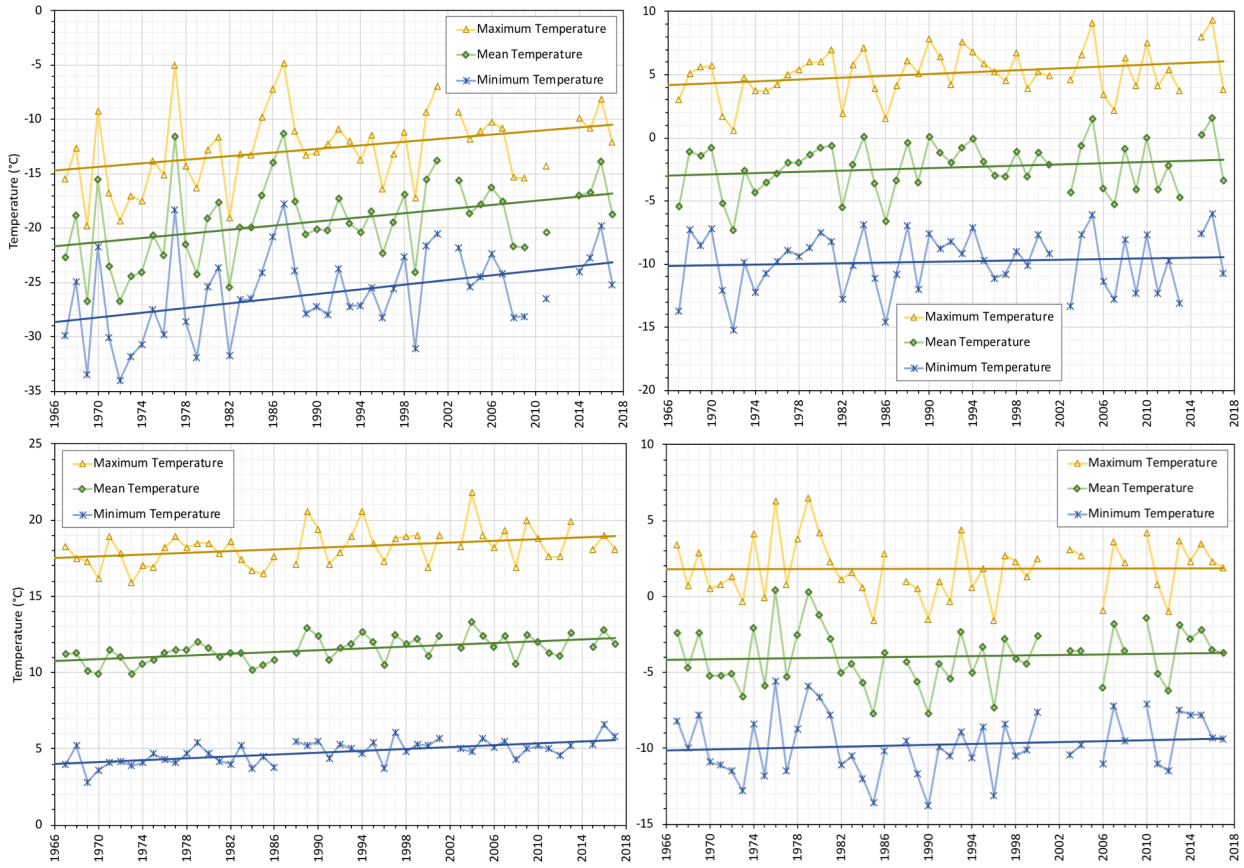

Figure 17. Seasonal means of daily mean, maximum and minimum temperatures and their trends for Burwash for 1967-2017. Winter (top left) Spring (top right) Summer (bottom left) Autumn (bottom right).

3.2 EU WATCH data (1901-2001)

The European Union Integrated Project Water and Global Change (EU WATCH, 2007-11, www.eu-watch.org) concentrated on the evaluation of terrestrial water cycle in the twentieth- and twenty first-centuries using land surface models and global hydrological models. Scientific contributions related to this project covered, among other topics, the assessment of land use change, evaporation, soil moisture and runoff; the potential vulnerability of water supply; and the role of global anthropogenic greenhouse gas emissions in increasing floods. WATCH resulted in the development of new data sets, maps and models which support improved understanding, analysis and prediction in global and regional hydrology.

WATCH Forcing Data (WFD) for the 20th C resolves the full diurnal cycle at a sub-daily time frame on a half-degree resolution regularly gridded globe domain (Weedon et al., 2010, 2011). It is derived from re-ordered ERA-40 reanalysis data for 1901-1957 and from the

surface variables of the ERA-40 reanalysis for 1958-2001. A detailed description of the ERA-40 reanalysis product by the European Centre for Medium-Range Weather Forecasts (ECMWF) is documented by Uppala et al. (2005). WFD comprises rainfall and snowfall rates, air temperature at 2 m, wind speed at 10 m, specific humidity at 2 m, surface pressure, downward longwave radiation flux and downward shortwave radiation flux. The precipitation rates and shortwave radiation are stored at 3-hourly time steps, whereas the other variables are stored at 6-hourly time steps. The topographic land-sea mask considered here was developed by the Climate Research Unit (CRU) of the University of East Anglia, and gives an average elevation for the Kluane Lake Basin of 1,600 m a.s.l.

The average WFD yearly precipitation amounts used in Kluane Lake basin simulations are presented in Figure 18. They range between 285 and 560 mm with a median value of 410 mm, which higher than the 283 mm median of measured annual precipitation at Burwash station. Viewing that the difference in elevation between basin CRU and Burwash amounts to 800 m, this 45% precipitation difference (127 mm) is in accordance with a lapse rate of 8% increase for every 100-m increase of elevation up to a maximum within the interval 1,500-2,000 m a.s.l. (Wahl, 2004). Further comparison of WFD and AHCCD precipitation for 1967-2001 is displayed in Figure 19 and the data provide a median difference of 96 mm.

Comparison of AHCCD and WFD mean winter and summer temperatures for their intersecting period 1967-2001 lead to interesting correlations, displayed in Figure 20, having 0.99 and 0.88 as coefficients of determination for winter and summer, respectively. These allowed for the extension of WFD data up to 2017 and consequently it was possible to quantify the evolution of climatological 30 years means of mean winter and mean summer temperature from 1930 to 2017 (Figure 21). The variation of temperature climatological means was less than 1°C up to 1970 for winters and up to 1990 for summers. The winters cooled by 1°C in the mid-1970s to recover by the late-1980s; and thereafter, from the 1990s to present, both winter and summer mean temperatures have increased steadily 1.7 and 1.2°C above their previous maximums.

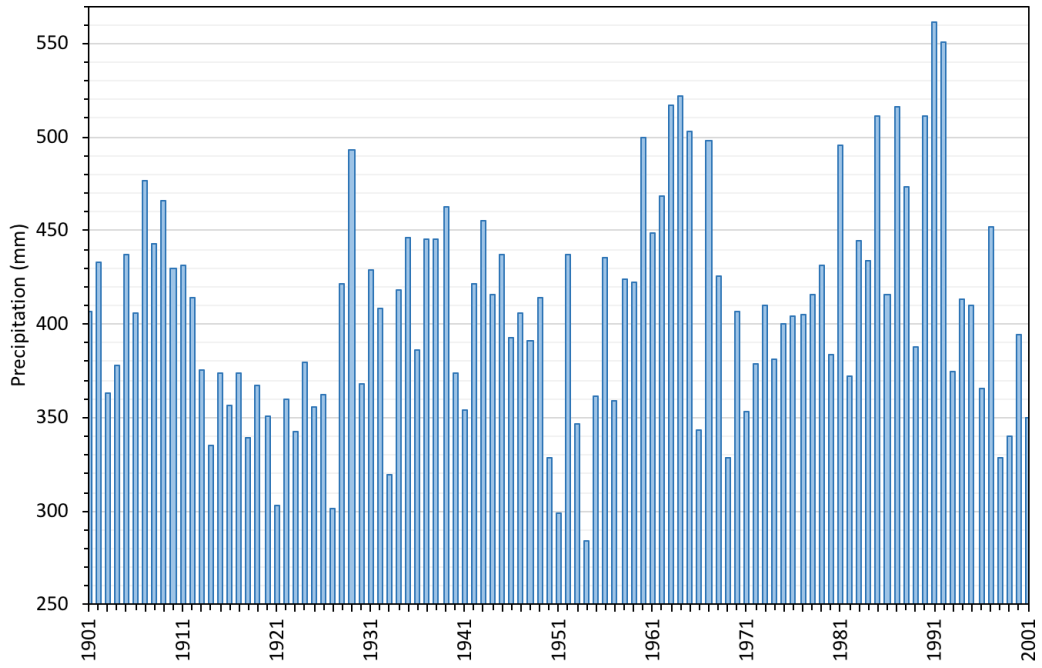

Figure 18. Kluane Lake Basin's average yearly total precipitation from WFD for 1901-2001.

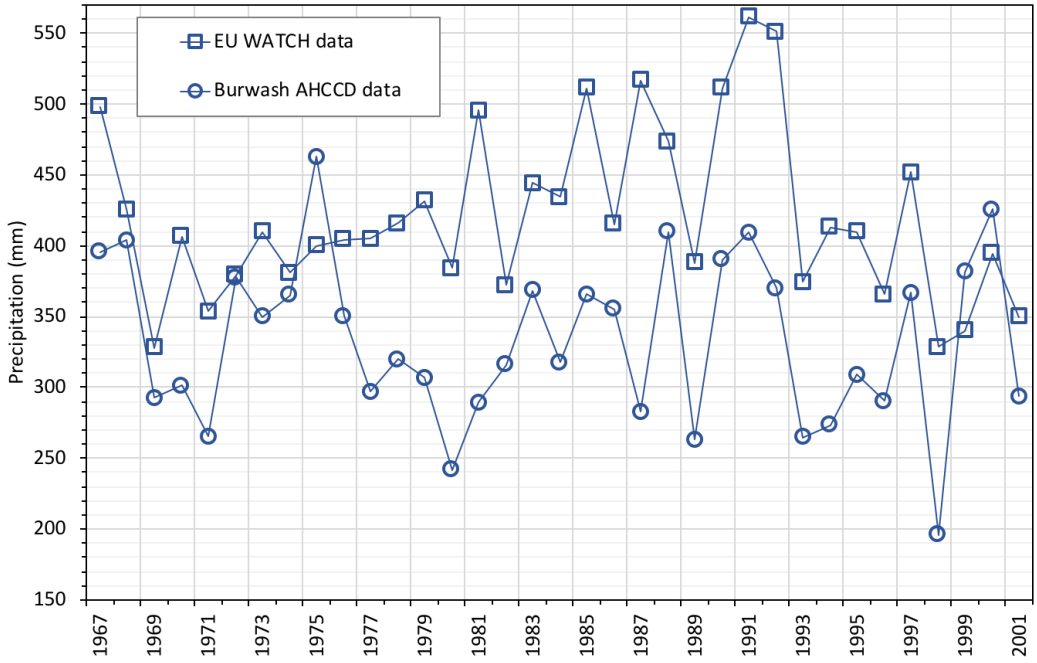

Figure 19. Contrasting yearly total precipitation from WFD and Burwash AHCCD (1967-2001).

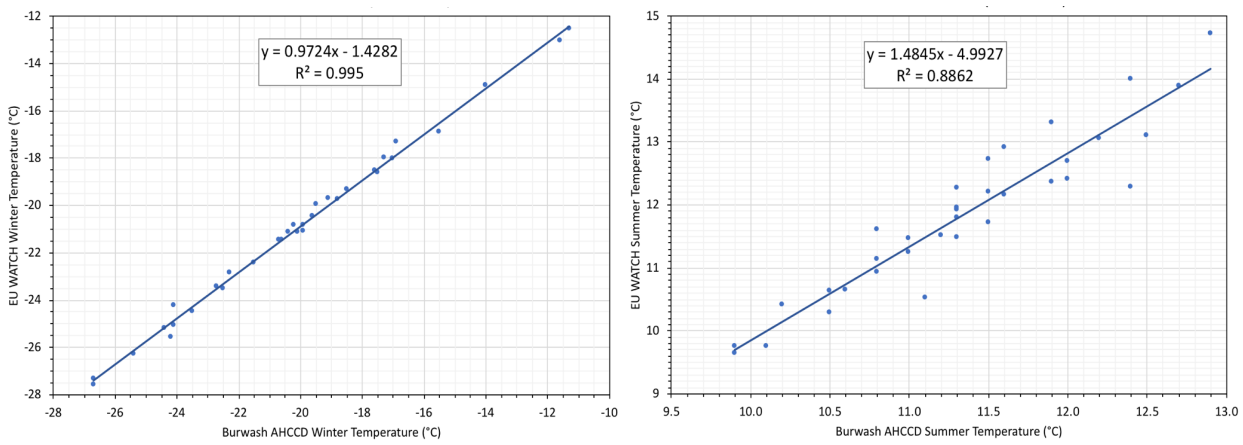

Figure 20. Correspondence between WFD and Burwash AHCCD mean winter (left) and mean summer (right) temperatures, for 1967-2001.

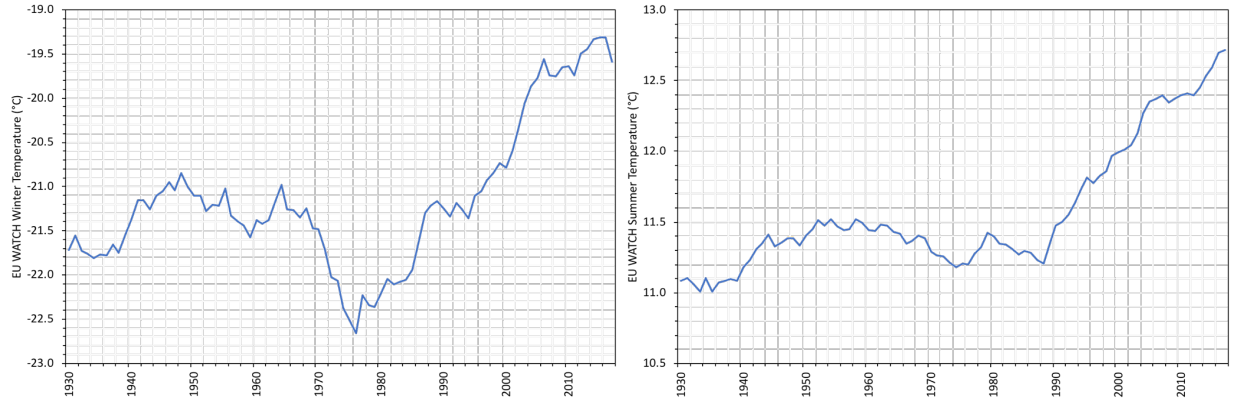

Figure 21. Evolution of climatological 30 years mean of mean winter (left) and mean summer (right) temperatures over Kluane Lake Basin for 1930-2017.

3.3 Current (2000-2015) and Future PGW (2086-2100) climate WRF-GEM-CaPA data

The Weather Research and Forecasting (WRF) is a numerical weather prediction and atmospheric simulation system developed within a collaborative partnership of the National Center for Atmospheric Research (NCAR), the NOAA's National Centers for Environmental Prediction (NCEP) and other government agencies and research organizations (Skamarock et al., 2008; https://www.mmm.ucar.edu/weather-research-and-forecasting-model). WRF is used in dynamical downscaling and nested Regional Climate Models (RCMs) to capture key regional and local climate processes, such as precipitation and temperature, and has the skill of a high-resolution 4-km convection resolving RCM. As a next-generation mesoscale

prediction model with data assimilation capabilities, it serves both atmospheric research and operational forecasting applications across different scales.

Recently, Li et al. (2018) conducted two regional climate 4-km WRF simulations over a domain covering the whole of western Canada: the first one, Current WRF, involves a retrospective run (2000-2015) with initial and boundary conditions from ERA-interim; and the second, Future PGW WRF, considers a 15-year future climate condition equivalent to the end of the 21st C in pseudo-global warming (PGW) mode (2086-2100). The PGW mode is processed with modified reanalysis-derived initial and boundary conditions through adding the CMIP5 ensemble-mean high-end emission scenario climate change, which is the ensemble-mean difference (1976–2005 and 2071–2100) for RCP8.5 greenhouse gas emission scenario. Furthermore, using the multivariate quantile mapping developed by Cannon (2018), this data has been bias corrected against ECCC's Global Environmental Multiscale (GEM) model and Canadian Precipitation Analysis (CaPA), resulting in new weather forcings referred here to as Current WRF-GEM-CaPA and Future WRF-GEM-CaPA (Elshamy M., personal communication, 2018). There is some loss of spatial resolution (4 km to 10 km) and the bias-corrected levels are 40 m rather than surface observations The reduced uncertainty in using a data set that is bias-corrected to a model that assimilates observed precipitation and is driven sub-daily from initial observed weather conditions is felt to be greater than the increased uncertainty in reduced spatial resolution. MESH is designed to be run with 40 m driving meteorology so there is no uncertainty introduced with that level.

The average annual precipitation amounts over Kluane Lake Basin from both Current and Future WRF-GEM-CaPA are shown in Figure 22. Modelled and measured precipitation show similar interannual variability. Calculation of the medians of differences between these and Burwash AHCCD annual precipitation gives respectively 101 mm for current climate and 154 mm for future climate. Differences with Burwash data are due to location and elevational differences between a point station and the whole Kluane Lake Basin. Winter and summer temperatures over Kluane Lake Basin are shown in Figure 23. Current winter temperatures are warmer in the model than for Burwash due to inversions near the lake (Wahl, 2004) and the higher height used in the model (40 m above the surface), whilst summer temperatures are comparable. The variability of modelled and measured data is comparable.

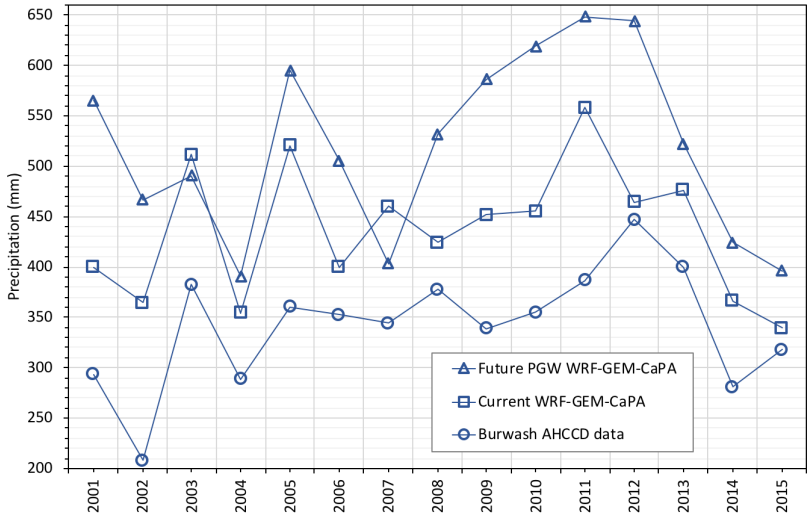

Figure 22. Kluane Lake Basin's yearly precipitation from Current and Future WRF-GEM-CaPA, compared to Burwash AHCCD data.

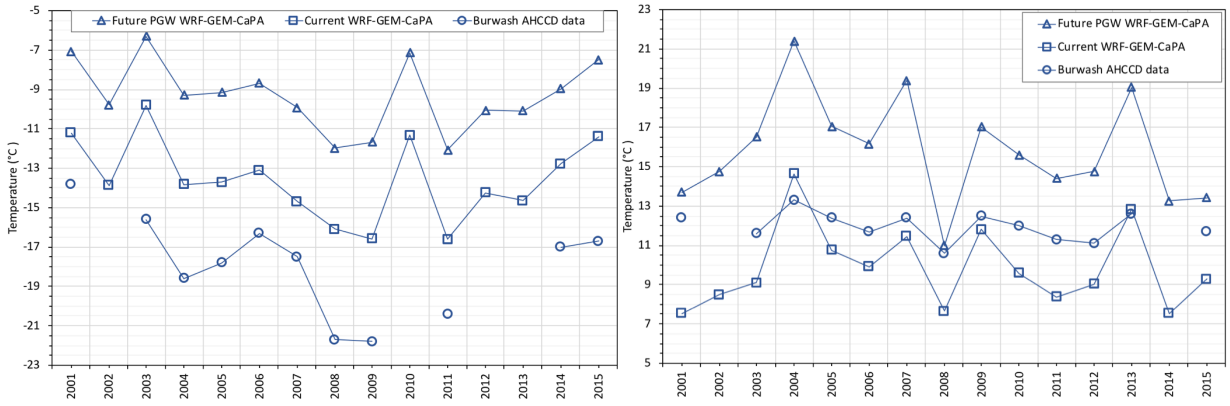

Figure 23. Kluane Lake Basin's mean winter (left) and mean summer (right) temperatures from Current and Future WRF-GEM-CaPA (40 m height) compared to Burwash AHCCD data (2 m height).

4. Hydrological modelling of the Kluane Lake basin

4.1 Canadian LAnd Surface Scheme (CLASS)

The Canadian Land Surface Scheme (CLASS: Verseghy, 1991; Verseghy et al., 1993) is described in detail in the Appendix with material drawn from Pomeroy et al. (2016). In summary, CLASS calculates separate vertical energy and water balances for four subareas: canopy over snow, canopy over bare ground, bare ground and snow-covered ground. Physically based algorithms are used to calculate: evaporation and evapotranspiration; evapotranspiration and sublimation from vegetation canopy; interception, throughfall and drip of rainfall and snowfall; freezing and thawing of liquid and frozen water on the canopy and in soil layers; surface ponding and freezing of ponded water; sublimation from the snowpack; snowmelt; infiltration of rain into the snowpack; infiltration into soil; soil water movement between soil layers in response to gravity and suction forces; and temporal variation of snow albedo and density. Four vegetation types are included in CLASS: needleleaf trees, broadleaf trees, crops and grass. Each vegetation type is assigned a background value for physiological parameters such as albedo, roughness length, maximum and minimum leaf area index, etc. Certain physiological parameters vary throughout a simulation using annual or diurnal functions. Figure 24 displays a schematic diagram of hydrological processes, energy processes, mass and energy fluxes, stores and control volumes as conceptualized in CLASS (Verseghy, 1991).

As noted by Pomeroy et al. (2016), LSS operated in isolation struggle to calculate realistic water budgets at river basin scales. This is partly because of the large number of unconstrained parameters that must be set from sparse or non-existent observations or from ecosystem-type lookup tables. It is also because LSS are essentially 1D representations of the water budget that attempt to homogenize vast swaths of the Earth's surface, whereas in nature, 3D interactions and ecosystem variety are important to the hydrological cycle. The next section will examine this variability and how hydrological models such as MESH address it without becoming overwhelmed with physical equations and uncertain and poorly constrained parameter values.

4.2 Coupled Hydrological Land Surface Scheme MESH

Pomeroy et al. (2016) note that recent development of coupled hydrological land surface schemes has blurred the lines between land surface and hydrological models, offering complementary advantages of the vertical and horizontal flux focus of each approach, the physical rigor of the LSS and the catchment conceptualization of the hydrological models. An example of a HLSS is the MESH model. As part of the MEC (Modélisation Environmentale Communautaire) developed by Environment Canada, the MESH (MEC - Surface and Hydrology; Pietroniro et al., 2007) is a stand-alone land surface hydrological model configuration of MEC that couples a LSS (CLASS) with hydrological routing schemes. Representation of spatial heterogeneity is based on a mosaic approach using the Group Response Unit (GRU) concept of hydrological landscape units (Soulis et al., 2000). The routing scheme was developed by Soulis et al. (2000; 2005) and is shown in Figure 25. It

includes the adaptation of CLASS to sloped terrain drainage functions and its coupling to the routing scheme of the WATFLOOD model (Kouwen, 1993). This involved the inclusion of physically based transfer functions between the soil column and the micro-drainage system within each GRU. The fundamental drainage element is conceptualized by an assembly of sloped blocks connected to a stream and with the drainage system. A GRU is viewed as a mosaic of slope tiles, drained by a system of micro channels. Excess surface water drains to the micro-drainage system as overland flow, q_{over}, represented by Manning's equation (Figure 26).

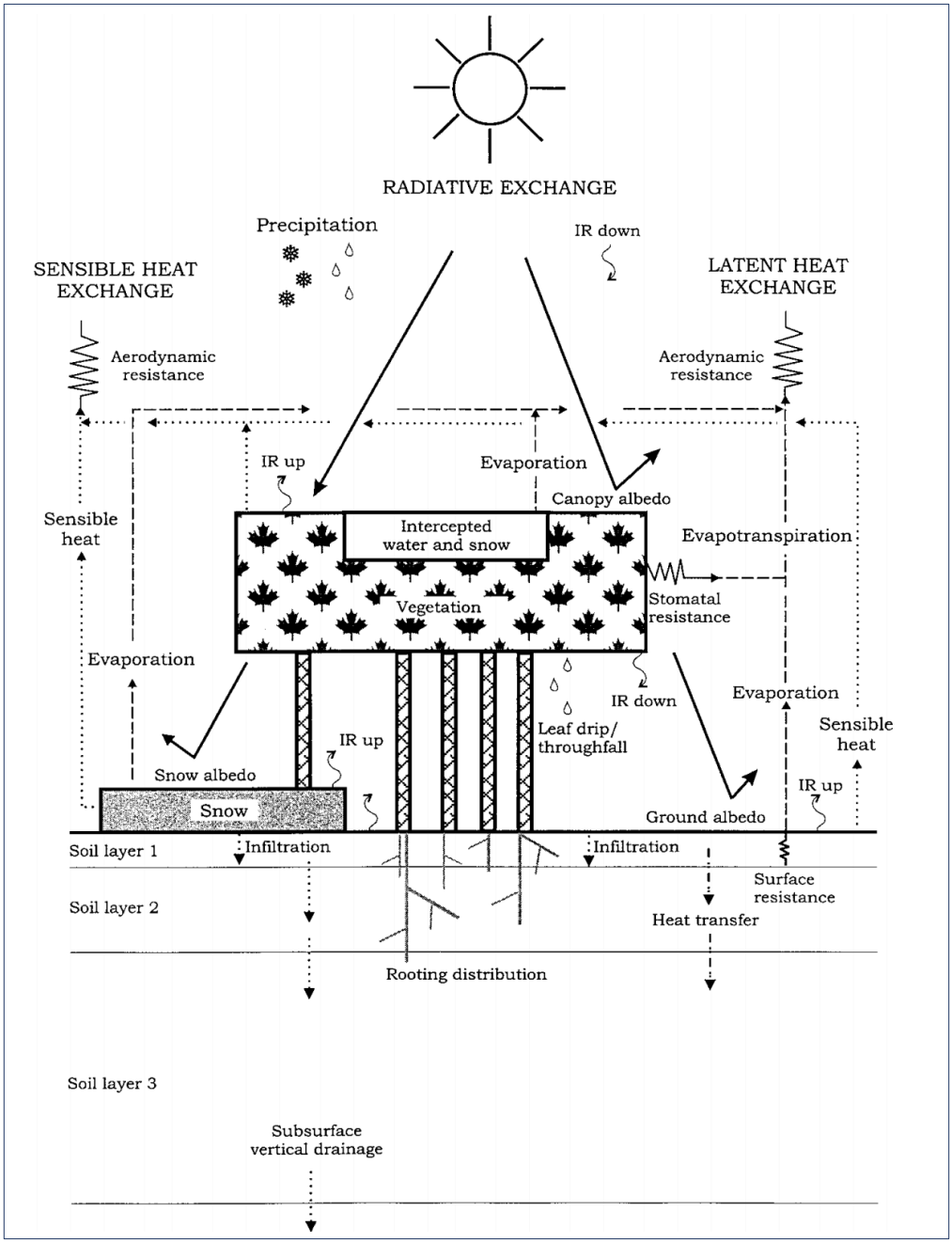

Figure 24. Schematic diagram of CLASS (Verseghy, 2000).

Figure 27 shows how the interflow or horizontal near-surface flow occurs through the soil matrix and the macropore structure, leaving the control volume through the seepage face. The conceptualization interflow as shown here was introduced by Soulis et al. (2000) and uses a shallow aquifer flow model, assuming that interflow occurs almost entirely when soil moisture is between saturation and field capacity. However, rather than solving the Richard's equations with the added complexity of highly variable hydraulic conductivities in the upper soil layer, the shallow aquifer is forced to fit a simpler power law that relates the total outflow at the seepage face and the average volumetric moisture content stored in a control volume, θ. This approach assumes an initial condition where the seepage face is fully saturated. With time, the water table drops below the surface of the face and the interflow becomes a mixture of saturated and unsaturated flow. Behind and above the water table, saturation declines in both time and space.

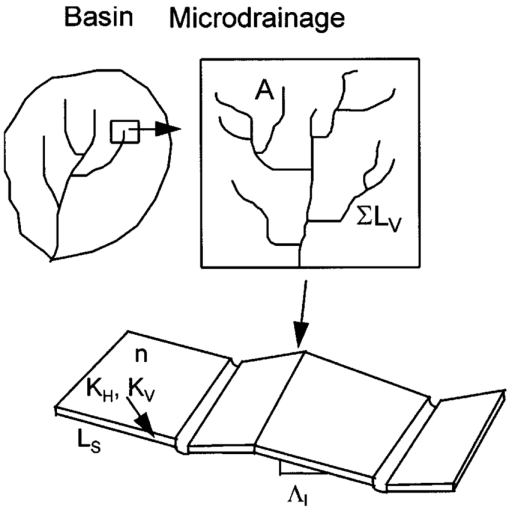

Figure 25. Schematic of the topography of a grid element in a watershed as adopted in the MESH hydrological land surface scheme (Soulis et al., 2000).

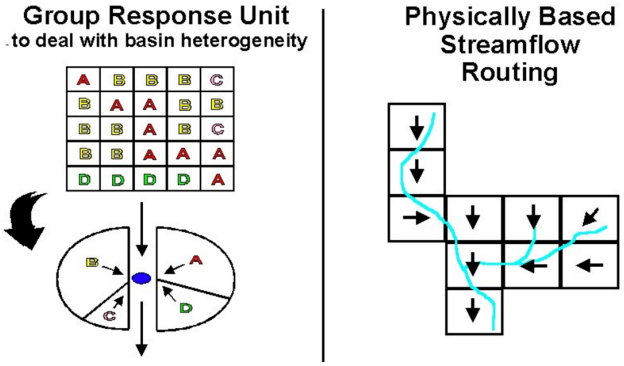

Figure 26. Group response unit and runoff routing concept (Donald, 1992).

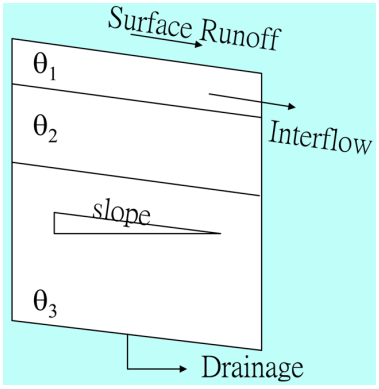

Figure 27. Soil water balance in the MESH hydrological land surface scheme.

The gravitational movement of water between the soil layers is governed by a finite difference solution of Richard's equation for unsaturated flow in porous media. The relation between horizontal and vertical hydraulic conductivity in slopes is assumed to be less than 10%, so the Dupuit–Forscheimer approximation is valid and the V_x can be calculated using a one-dimension Richard's equation. Variation of the hydraulic conductivity with depth follows an exponential form similar to TOPMODEL, whereas the variation of hydraulic conductivity in unsaturated conditions uses the Clapp–Hornberger soil physics.

River or streamflow routing in MESH is based on a storage routing method originally implemented in the WATFLOOD model (Kouwen, 1988). This is a simple technique since storage is calculated solely as a function of outflow. The implementation is based on the continuity equation for each river reach where the inflow consists of overland flow, interflow, baseflow and channel flow from all contributing upstream basin elements, whereas outflow is related to the storage through Manning's formula. Channel cross-section area is related to storage by dividing the storage by the channel length, and channel storage is calculated using a relation such that the channel cross-section area is given as a function of drainage area. The roughness coefficient incorporates a channel shape and width-to-depth ratio as well as Manning's *n*.

4.3 Kluane Lake MESH model setup

The preparation of input data for complex distributed hydrologic models is a challenging and critical step towards the success of land surface water and energy simulations. Local knowledge of terrain properties, measurements and river basin information, all help in choosing the parameterization framework within which the computational model is expected to simulate land atmosphere water and energy exchanges and water flow regime patterns. Geographical Information Systems (GIS) have become very helpful computerized mapping tools for visualizing and preprocessing a wide-ranging variety of terrestrial data. Here, QGIS and its GRASS-linked Toolbox were used to prepare hydrological input layers.

Digital Elevation Model (DEM)

The Global Multi-resolution Terrain Elevation Data 2010 (GMTED2010) at its finer 7.5-arc-second spatial resolution, produced by the U.S. Geological Survey (USGS) and the National Geospatial-Intelligence Agency (NGA), was used here to represent thoroughly the Kluane Lake Basin topography. GMTED2010 incorporates new data sources including global Digital Terrain Elevation Data (DTED) from the Shuttle Radar Topography Mission (SRTM), Canadian elevation data, Spot 5 Reference3D data, and data from the Ice, Cloud, and land Elevation Satellite (ICESat). Since the study area is above 60^{o}N, the consistency and vertical accuracy of GMTED2010 is uncertain.

The ArcticDEM, implemented through the Polar Geospatial Center (PGC), is a National Geospatial-Intelligence Agency (NGA)-National Science Foundation (NSF) public-private initiative to automatically produce high-resolution, high quality, digital surface model of the Arctic using optical stereo imagery, high-performance computing, and open source photogrammetry software. It encompasses all land area north of 60°N. The PGC creates and delivers 5-metre mosaic DEM in 50 km x 50 km tiles assembled from multiple time-dependent strip DEMs, which generates a more consistent and comprehensive product over larger areas. Eight ArcticDEM tiles covering the study domain were merged and used as guidance in drawing/correcting the delineation of the basin and sub-basins boundaries. The frequent occurrence of void areas and obvious errors in the ArcticDEM caused some limitations in processing and analysis.

Figure 28 shows GMTED2010 processed for Kluane Lake and Duke River basin, and Figure 29 displays the performance of ArcticDEM in depicting the Glacier terminus and the piracy location at the valley fork.

Land cover

A 2010 land cover map, at 7.5-arc-second spatial resolution, from the North American Land Change Monitoring System (NALCMS) is used here. This dataset is made available by the Commission for Environmental Cooperation (CEC) between Canada, Mexico, and the United States. It accommodates nineteen land cover classes defined by the Land Cover Classification System (LCCS) standard developed by the Food and Agriculture Organization (FAO) of United Nations. For this study domain, NALCMS land cover was reclassified into eight classes to be considered as GRUs in MESH: Needleaf forest, Broadleaf forest, Mixed forest, Shrubs/grass, Alpine, Wetland, Water and Glacier (Figure 30). The data show that the disconnection of Kaskawulsh Glacier from Kluane Lake drainage decreased the glacier's area from 908 to 63 km^2 and the alpine's area from 1,241 to 947 km^2.

Water courses and waterbodies

The water courses and waterbodies from the geospatial CanVec data series published by Natural Resources Canada were used here. At present, CanVec is deemed to be the most current, accurate, and consistent, and it complies with international geomatics standards. This GIS information is mapped for Kluane Lake and Duke River Basins in Figure 31 and

helped with the support of the DEM in digitizing the boundaries of 19 sub-watersheds in Kluane Lake basin.

Kaskawulsh sub-glaciers delineation

The detailed but incomplete ArcticDEM encouraged in the exploration of the Kaskawulsh Glacier hydrological connections. Although there is some subjectivity related to the DEM representing glacial surface, unclear divides on the western limit of the glacier and mostly unknown and dynamically changing meltwater flow lines, it is still imperative to provide a computational spatially distributed flow model such as MESH with feasible flow lines and directions. For this purpose, it was assumed that both surface and moulin meltwater flows follow the same directions induced by the glacier's topography and that the dynamics of their homogenized sum can be approximated by the routing modelling in MESH at the considered discretization scale. Figure 31 displays the digitized meltwater flow lines and boundaries of five sub-glaciers: North Arm, Central Arm, Stairway, South Arm and Lower Arm.

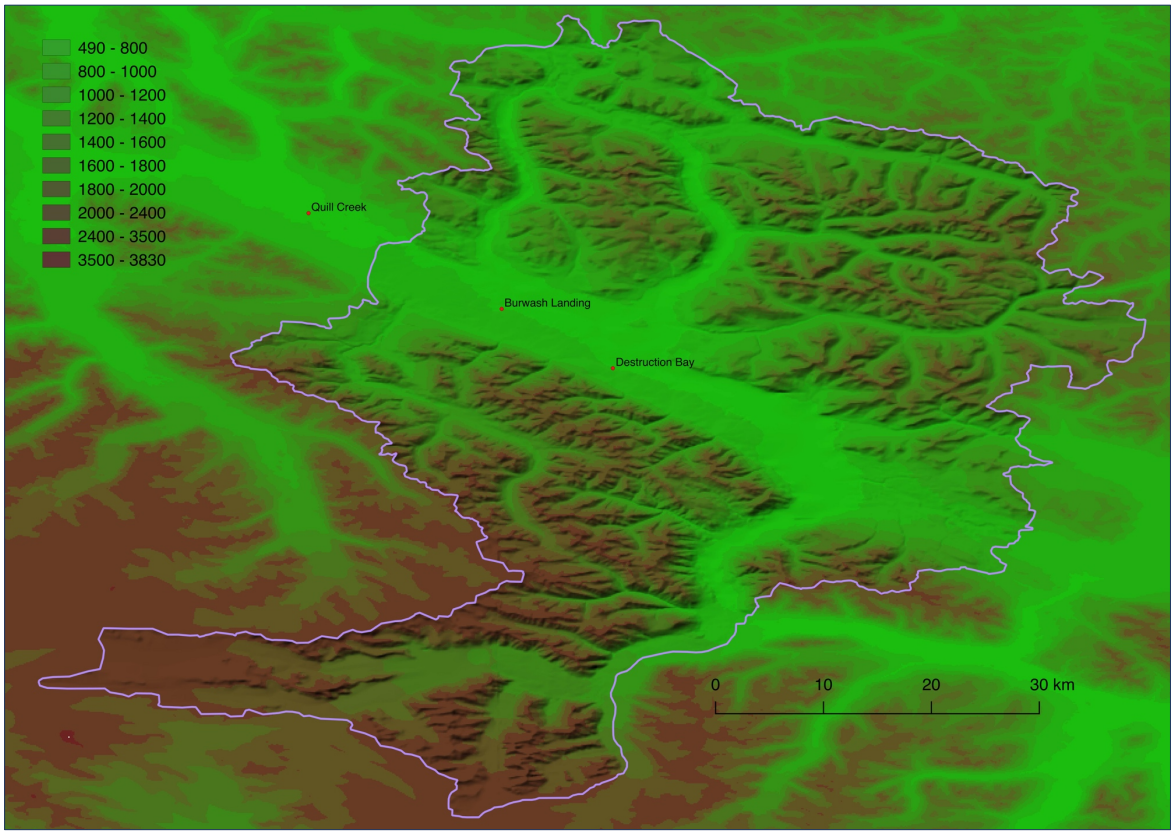

Figure 28. Kluane Lake and Duke River basins Elevation from GMTED2010.

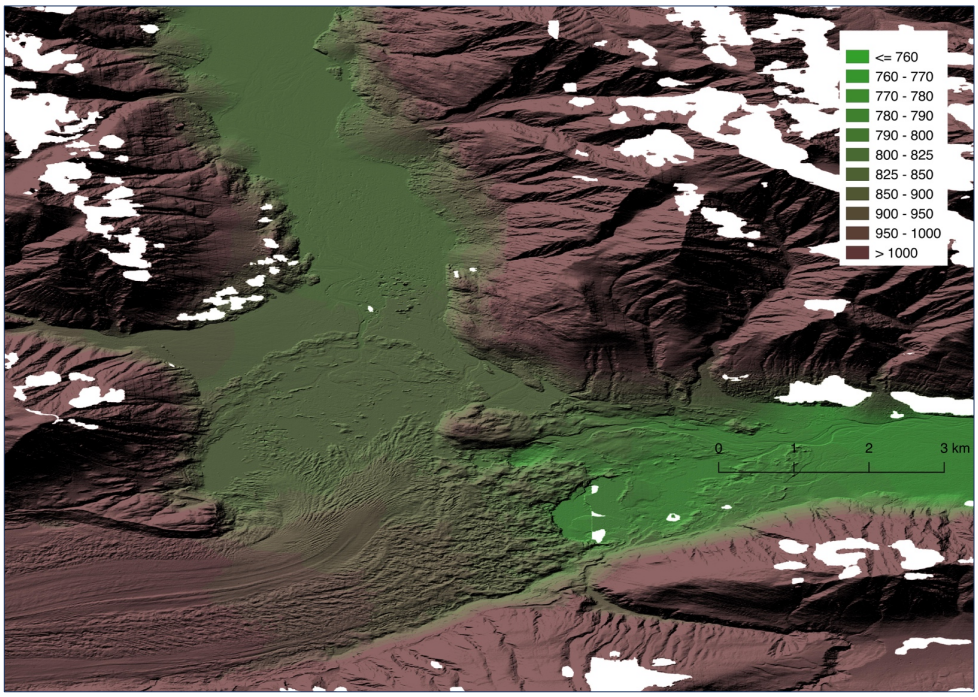

Figure 29. A view of the Glacier terminus and piracy point at the valley fork.

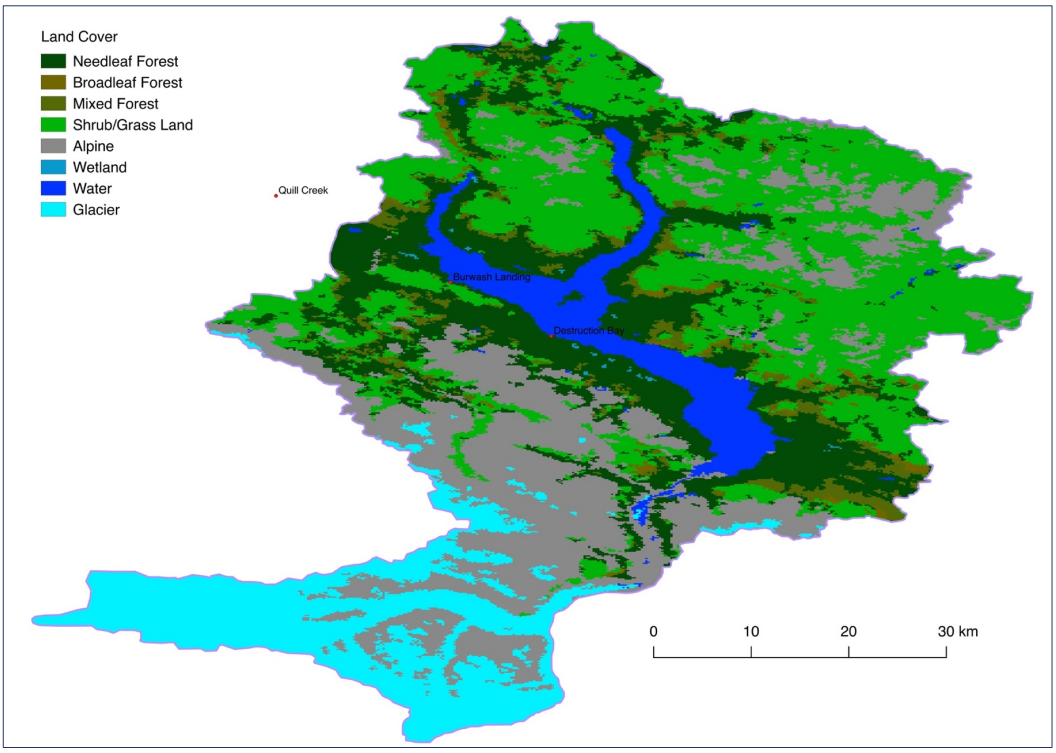

Figure 30. Land cover classification in Kluane Lake and Duke River basins.

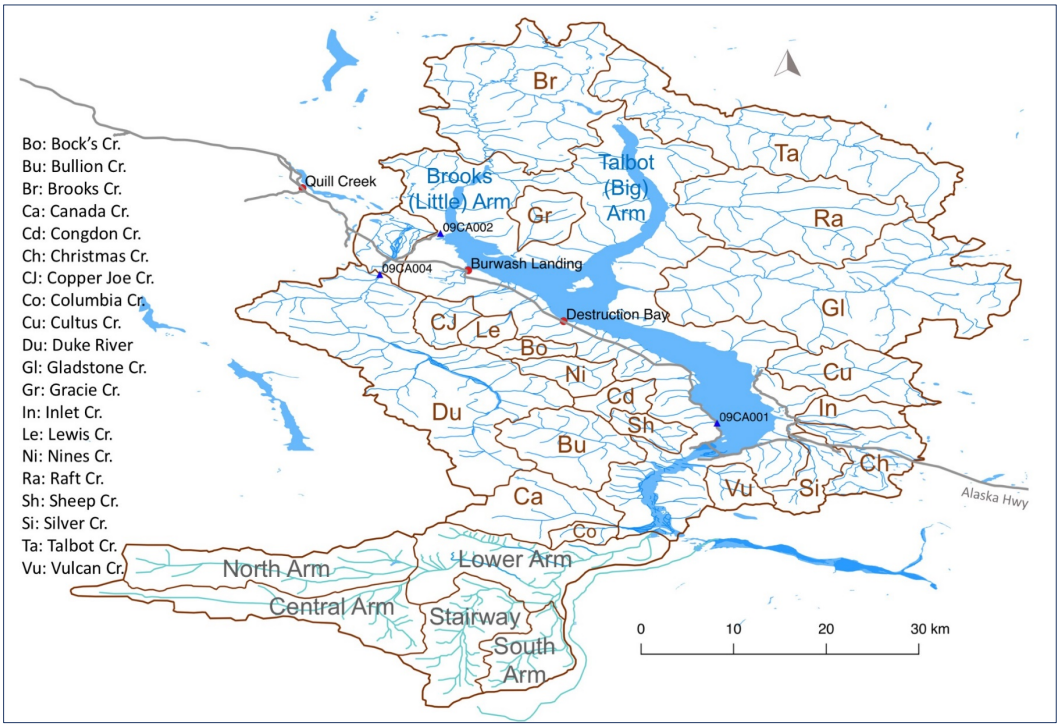

Figure 31. Sub-basins in the study domain.

Soil type

Brabets et al. (2000) described many soils, environmental and hydrological aspects of the Yukon River Basin. Their soil map shows that

a- "Rough Mountain Land" covers all the area west and south of Kluane Lake and south of the Duke River delta;
b- Gelisols cover a small area of the study domain north of the lake two arms skewed to the east;
c- Brunisols cover the eastern part of the domain, the western shores of the lake, the area west of Burwash Landing and the sandurs of Slims River.

Linking this information to the land cover, the soils of the Alpine GRU were classified as exposed rock and the rest of the domain as Brunisolic soils. Smith et al. (2011) studied the genesis, distribution and classification of this specific soil type in Canada. Over southern Yukon, they reported that in areas of lower elevations and lighter precipitation below 350 mm, Eutric Brunisols dominate the land surface; whilst at higher elevations with greater precipitation, Dystric Brunisols are more prevalent. Guided by the layering and soil composition of these two Brunisols types (Smith et al., 2011 – Table 1), Brunisols in this MESH setup are described as (54% sand, 3% clay and 43% silt) for the top 10 cm layer (leaning to Dystric), and (68% sand, 10% clay and 22% silt) for all lower layers (leaning to Eutric).

Study domain discretization

As noted in the introduction, both Kluane Lake and the adjacent Duke River basins were included in the study domain which lies within the latitude/longitude mask box [60.4,61.9]-degree North / [139.9,137.8]-degree West. The spatial discretization chosen was based on 0.025 degrees for both dimensions and yielded a relatively fine grid having 60 x 84 cells (Figure 32). At this geographical location, the length (along latitude) and width (along longitude) of each cell is around 2.79 and 1.35 km, respectively, giving an approximate cell area of 3.766 km^2.

The National Research Council Canada (NRCC)'s Green Kenue hydrological analysis and visualization software (https://www.nrc-cnrc.gc.ca/eng/solutions/advisory/green_kenue_index.html) was used to map topography and land cover onto the discretized domain, and to create flow directions and drainage areas and drainage densities as well, for 1982 cells representing the modelled domain. Flow directions were quality controlled and corrected to comply with the hydrology in sub-watersheds and sub-glaciers (Figure 33).

Due to code limitations, soil depth was input as the standard CLASS constant of 4.1 m all over. Meanwhile, a better resolving soil discretization was selected as it additionally helped stabilize MESH runs by preventing sporadic crashes. That is, eight layers of thicknesses from top to bottom 10, 10, 20, 20, 50, 100, 100 and 100 m were chosen.

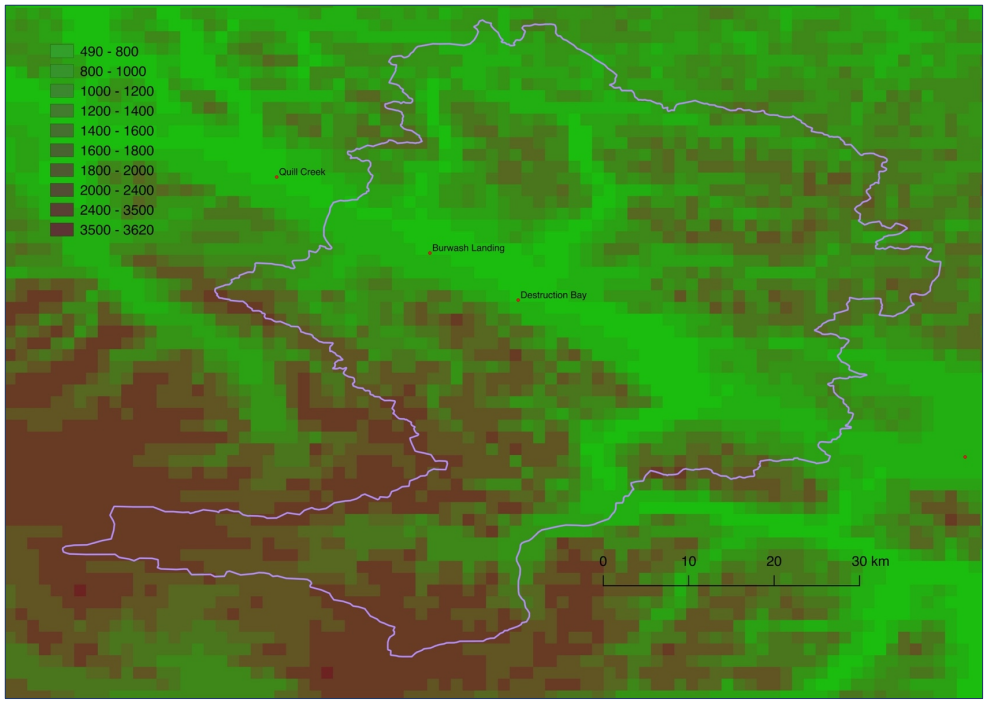

Figure 32. Map of the computational domain discretization for modeled terrain elevation.

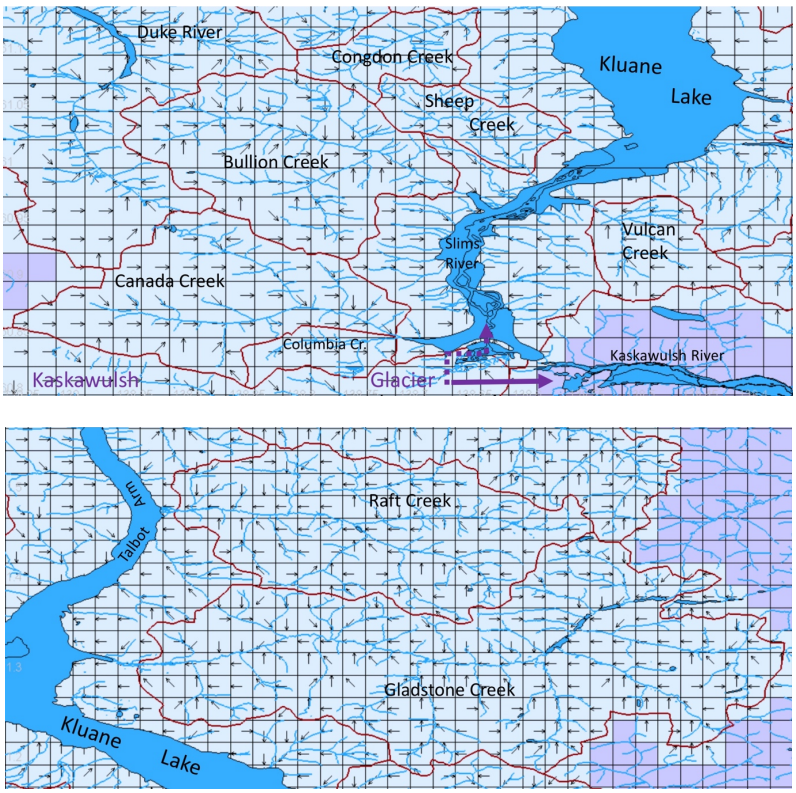

Figure 33. Examples of flow directions prescription in Slims River (top) and Raft and Gladstone Creeks (bottom).

Calibration of model parameters

As in all modelling exercises, proper determination of parameters was necessary here for obtaining acceptable computations of water flow and levels. In a first step, lake inflows calculated from storage helped as a guidance in the setting of some hydrology parameters. The choice of more than three soil layers also improved the stability of results and avoided some occasional execution crashes. Moreover, the glacier module parameterization was revisited and the ice albedo was decreased to 0.15 in order to account for both the current mixture of debris, dust and sediment-covered glacier and the impact of glacier moulins on reflectance. Certainly, the choice of a high resolution (~4 km^2) and the attentive manual correction of flow directions using mapped sub-basins and watercourses, also helped ensure that model reflected reality to the greatest degree possible and prevented unnecessary biases in the calibration exercise. The Appendix summarizes most of the important model parameters retained in this study. Vegetation input parameters are also given in Table 3.

Parameter	Needleaf Forest	Broadleaf Forest	Mixed Forest	Shrub/ Grass
Natural logarithm of maximum vegetation roughness length	-1.9	-1.6	-1.743	-4.6
Annual minimum vegetation leaf-area index	1.6	0.5	1.05	3
Annual maximum vegetation leaf-area index	2	6	4	4
Average visible albedo of vegetation category when fully-leafed	0.03	0.05	0.04	0.055
Average near-infrared albedo of vegetation category when fully-leafed	0.19	0.29	0.24	0.32
Annual maximum canopy mass for vegetation category [kg m^{-2}]	25	20	22.5	5
Annual maximum rooting depth of vegetation category [m]	1	2	1.5	1
Minimum stomatal resistance of vegetation category [s m^{-1}]	200	125	162.5	100
Reference value of incoming shortwave radiation (used in stomatal resistance calculation) [W m-2]	30	40	35	30

Table 5. Vegetation parameters used in the simulations.

5. Presentation and analysis of simulation results

The simulation results presented here correspond to the three processed meteorological forcing periods, namely the EU WATCH data (1901-2001), the Current WRF-GEM-CaPA Controlled data (2000-15) and the Future PWG WRF-GEM-CaPA Controlled data (2000-15). All the computational MESH workloads were executed in parallel mode on Compute Canada's Graham heterogeneous cluster using 32 cores on one node with 15GB RAM per CPU for the twentieth century runs and 3GB for the others.

5.1 Model Runs using EU WATCH data (1901-2001)

During this 20th C period, the model reproduced reasonable lake inflows and levels and this was apparent from the overall tracking of the normal snowmelt freshet timing, lake level rise and fall timing and rising and falling limbs of hydrographs. The application of those evolving RCs that have been identified for various sub-periods, as shown in Figure 12, improved the results and allowed better dynamical adjustment of winter lake levels relating to the partial effect of the outlet erosion. Figure S-1 shows the overall simulated lake levels. Figures S-2 to S-6 plot model and available observed levels over five decadal periods from 1952 to 2001. Compared to measured lake peak levels, computed peak levels fit very well for 14 years: 1954, 1956, 1957, 1959, 1963, 1965, 1969, 1972, 1979, 1994, 1997, 1999, 2000 and 2001. As mentioned above, there is evidence presented in past studies and this study that the meltwaters from Kaskawulsh Glacier historically have been shared between the Slims and the Kaskawulsh Rivers, but to a highly variable degree over the summer and from year to year. For instance, by analyzing Kluane River flow hydrographs, Johnson (1986) illustrated some periods of glacier discharge being split towards the two rivers and indicated that 1953, 1967 and 1970 were years when glacier discharge was diverted primarily to the Kaskawulsh River and Alsek River, whilst 1957, 1971 and 1980 were years when most glacier discharge flowed into the Slims River. This diagnosis can be extended using the MESH simulations. Diagnosis of the observed and simulated streamflows reveals that in 1989, the Slims experienced a previously unreported partial piracy into the Kaskawulsh River, more severe than that of 1970. The reconstruction of the 1989 lake levels by means of the RC suggests partial piracy and the corresponding streamflow increase in the Alsek River supports this (Figure S-7). In order to quantify the gain or loss of glacier flow to the Slims River, the fractional diversion was estimated on a yearly basis by trial and error fitting of the model, including all glacial outflows, to observed peak lake levels. The fractional diversion is an estimate of the degree of river piracy to or from the Slims River as estimated by the model and is shown in Figure S-8. A gain (positive diversion fraction) means that there is more streamflow than from the modelled glacier contributing area, 0 means no diversion and a loss (negative diversion fraction) means that there is less streamflow than from the modelled glacier contributing area. The results suggest that the historical diversion fractions are skewed towards piracy from the Slims River to the Kaskawulsh River. If the median fractional diversion (-0.12) is considered as a reference, then at least 10 years experienced piracy events away from the Slims River, namely 1953, 58, 61, 67, 70, 80, 85, 89, 90 and 98; and at least 8 years sustained piracy towards the Slims River, namely 1962, 66, 71, 74, 93, 94, 97 and 2001.

Since the 2016 piracy by the Kaskawulsh River, the recent Slims River flow is a vastly diminished contribution to Kluane Lake, but in the past, the Slims River was the major contributor to the lake. Simulating Slims River streamflow is therefore crucial to this analysis, and so the MESH model results were compared to the few available historical discharge measurements reported here in Table 1. Figure S-9 to S-15 correspond to 1955, 1962, 1963, 1965, 1970 and 1983 respectively, and give a summary of streamflows and lake inflows with the glacial inputs. These show a reasonable match between measured and modelled Slims River discharge. In particular, the model reproduced the 1970 discharge during both the normal flow period in July (with glacial melt included) and the piracy period (diverted glacial melt) in August.

A second round of MESH simulations involved the scenario with the complete subtraction of Kaskawulsh Glacier's flow contribution in order to predict the current state of the glacier and Slims River. Two cases were examined: one using an estimated open water RC representative of lake levels/outflows conditions during the 20th Century (Estimated open water 1995 RC), and a second using a projected open water RC extrapolating the historical shift in RCs forward by assuming continued erosion at the outlet to describe the flow regimes of the present and the future (Estimated open water 2015 RC). In Figure S-16, the model was used to compute lake levels without the Kaskawulsh Glacier outflow feed to the Slims River and hence to Kluane Lake. The average difference in levels between the case of Estimated open water 2015 RC and the case of Estimated open water 1995 RC is 0.25 m suggesting a drop in average water levels over 20 years due to degradation of the outflow channel of Kluane Lake at Kluane River.

The statistics of modelled flows and levels in the 20th Century presume either complete or no Kaskawulsh Glacier contribution (using Estimated open water 1995 RC) to Kluane Lake via the Slims River. Figure S-17 displays median lake levels within one standard deviation in both cases, and shows a substantial seasonal drop in levels from June to October when the glacier discharge is excluded, reaching a maximum difference of 1.6 m from levels with the glacier during the month of August. Diagnosis of the impact of glacier meltwater drainage on hydrology is shown with the median Slims River and lake inflow with and without the Kaskawulsh Glacier in Figure S-18. In the absence of the glacier, median inflows drop from more than 350 m^3s^{-1} to around 60 m^3s^{-1} during the month of July.

Figure S-19 also provides the output data extremes and the five percentiles of lake levels for the case without Kaskawulsh Glacier meltwater inputs using both 1995 and 2015 open water RCs. Without the glacier inputs, the summer peak in lake levels are smaller and summer median levels reach barely 779.8 and 779.4 m using the 1995 and 2015 open water RC, respectively. The post-piracy levels of 2016-18 manifested consecutive peaks of 779.5 779.65 and 779.4 m and are quite consistent with the 2015 open water RC.

5.2 Model Runs using Current and Future Climate WRF-GEM-CaPA (2001-2015)

For this simulation period, due to some technical challenges in model spin-up, only results starting from 2003 are presented in Figure S-20. Two years, 2009 and 2015, show an especially good fit to observed peak lake levels, whereas the comparison indicates the

dominance of Slims River glacier drainage intake in 2003, 2005-08 and 2010-14, and a negligible deficit in 2004. The Slims River drainage dominance shown in the early 21st C probably reflects the higher melt rates from the glacier as it ablated and warmed under climate change and its retreat as evidenced by the rapid growth of Slims Lake from no lake at all in 1990 to 1.1×10^6 m2 in 2000 and 3.9×10^6 m^2 in 2015 (Shugar et al., 2017).

Simulated Kluane Lake levels without the Kaskawulsh Glacier inputs are also plotted in the same graph for both 1995 and 2015 open water RCs, and their statistics are displayed in Figure S-21. The estimated 2015 RC seems to capture the current flow regime through the lake most realistically, giving minimum, median and maximum peaks around 779.4, 779.7 and 780.5 m a.s.l. respectively. Until a modern, regularly measured RC for Kluane Lake is produced and maintained, this 2015 RC can be used as guidance for the expected levels and flows by local design and hydrology projects.

Finally, the perturbed PGW future climate simulations project the impact of climate change following the RCP8.5 greenhouse gas emission scenario towards the end of this century on Kluane Lake, where peak levels around 782.2 m a.s.l. would have been the norm if the Kaskawulsh Glacier continued to feed into Kluane Lake (Figure S-22). Removing the glacial input from Kluane Lake, the model results show lake levels that are similar to those in the current climate. The statistics describing lake levels without the glacier contribution by late 21st C are minimum, median and maximum peaks around 779.4, 779.7 and 780.1 m a.s.l. respectively, using the estimated 2015 RC (Figure S-23). The future projections predict a forward shift in timing of peak levels from July to early June (Figure S-24).

These results can be interpreted in light of the speculation by Shugar et al. (2017) that the Kluane River could cease to flow in the future and that Kluane Lake might in time flow up the Slims River to drain via the Kaskawulsh River to the Alsek River Basin. The MESH model applies Newton's Law of Conservation of Mass and Energy (continuity) amongst other physical laws and results for the recent time and future show continued outflows of Kluane Lake through the Kluane River in all scenarios. These flows may increase in time as the RC responds to further erosion in the gravel bar just downstream of where the river departs the lake, but there is no indication whatsoever that Kluane River flows will cease in the future. The MESH model is not a geomorphology model and so does not calculate erosion, but the elevational difference along the Slims River from Kaskawulsh Glacier to its mouth would require substantial erosion. Rates of erosion along this channel are outside of the scope of this study and are not known with certainty, though it should be noted that further undercutting of the Slims River channel has not been reported. Current streamflows in the Slims River are low enough that any such erosion would likely take much longer than the two-century time periods that this study have examined.

6. Conclusions

River piracy due to diversion of the Kaskawulsh Glacier from the Slims River into the Alsek River drainage since 2016 has reduced peak Kluane Lake levels by up to 1.6 m in August from previously recorded lake levels. There is evidence of partial river piracy away from the Slims River in the past, specifically in 1953, 1958, 1961, 1967, 1970, 1980, 1985, 1989, 1990 and 1998; and at least 8 years show evidence of some piracy of glacial meltwaters towards the Slims River, namely 1962, 1966, 1971, 1974, 1993, 1994, 1997 and 2001. The MESH hydrological model driven by EU WATCH meteorological model data over the 20th C and bias-corrected WRF meteorological model data for the early and late 21st C with and without the Kaskawulsh Glacier contribution was used to estimate lake levels over a 2 century time span. Results show that lake levels are very sensitive to conditions at the outflow of the lake into the Kluane River as represented by the rating curve of the river. From 1995 to 2015 the estimated rating curve changed such that average lake levels dropped 0.25 m. This drop in water levels is due to degradation of the outflow channel of Kluane Lake at Kluane River. It is strongly recommended that regular measurement of this rating curve be re-established in the Kluane River so that future changes can be quantified.

MESH results for the 20th C show a substantial seasonal drop in Kluane Lake levels from June to October when the glacier discharge is excluded, reaching a maximum difference of 1.6 m from lake levels calculated with the glacier during August. In the absence of the glacier, median inflows to Kluane Lake via the Slims River drop from more than 350 $m^3 s^{-1}$ to around 60 $m^3 s^{-1}$ during the month of July. Without the glacier inputs, the modelled summer peaks in lake levels are lower and summer median levels reach barely 779.4 m using the most recent rating curve. The measured post-piracy peak lake levels of 2016-2017-2018 were 779.5, 779.65 and 779.4 m and are quite consistent with results of the model using the most recent rating curve.

MESH results for the early 21st C without the Kaskawulsh Glacier inputs are also realistic for the current lake level regime, with minimum, median and maximum peak levels of 779.4, 779.65 and 780.5 m respectively using the most recent rating curve. Until a modern, regularly measured rating curve for Kluane Lake is produced and maintained, these results can be used as guidance for the expected levels and flows by local design and hydrology projects. Model results for the late 21st C under substantial climate change, provide Kluane Lake levels without the glacier contribution with minimum, median and maximum peaks of 779.4, 779.7 and 780.1 m respectively, using the most recent rating curve. The future projections predict a forward shift in timing of peak levels from July to early June but are otherwise not notably higher or lower than the current projections. There is no indication from the MESH model in any scenario that the Kluane River will cease flows in the future, rather it is likely that further erosion of its bed will increase outflows from Kluane Lake over time.

7. Simulation figures

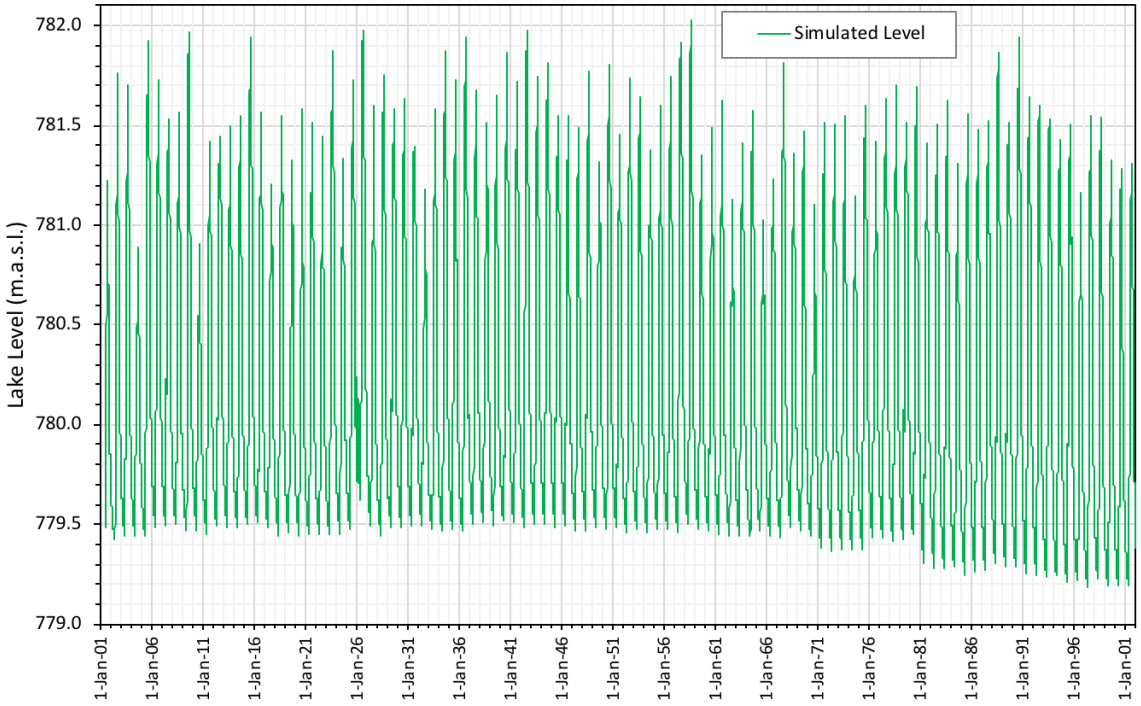

Figure S-1. Kluane Lake simulated levels with the Glacier contribution – 1901-2001.

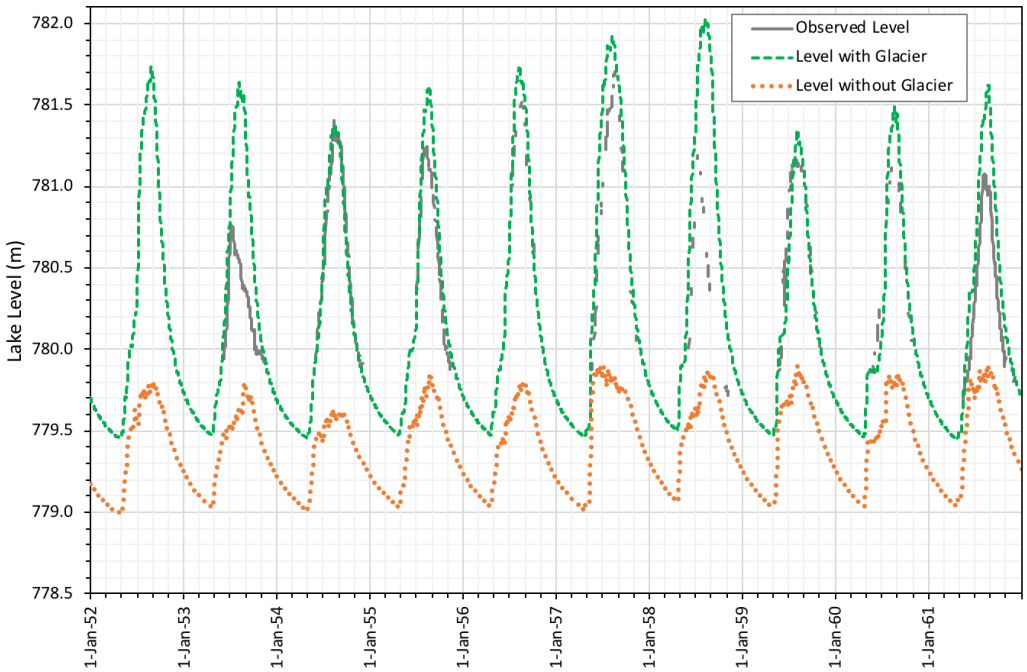

Figure S-2. Kluane Lake simulated versus observed levels – 1952-1961.

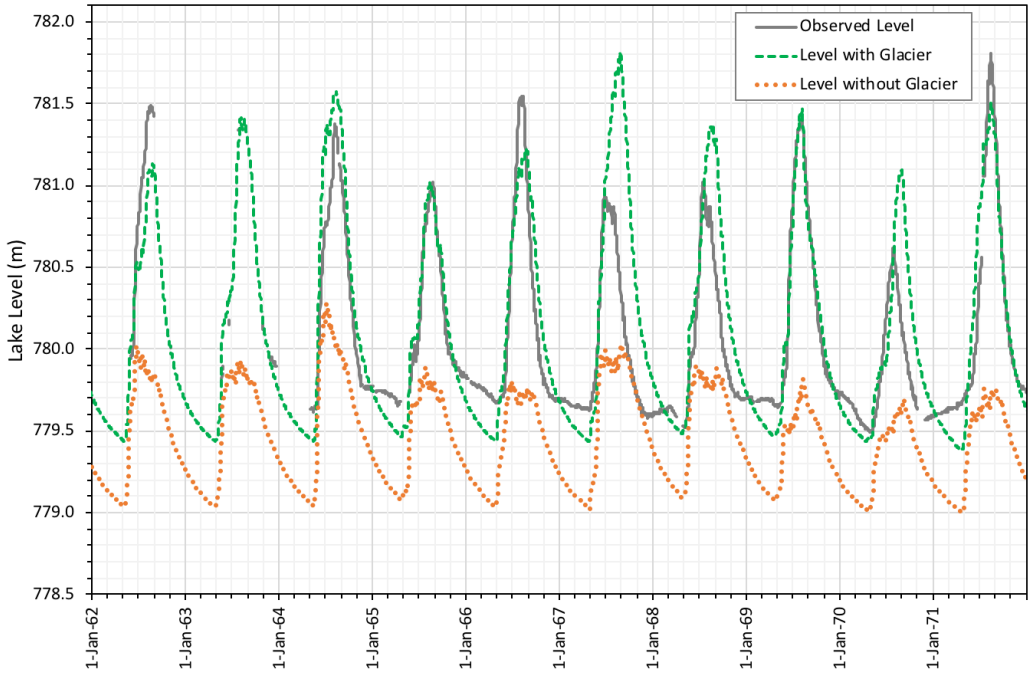

Figure S-3. Kluane Lake simulated versus observed levels – 1962-1971.

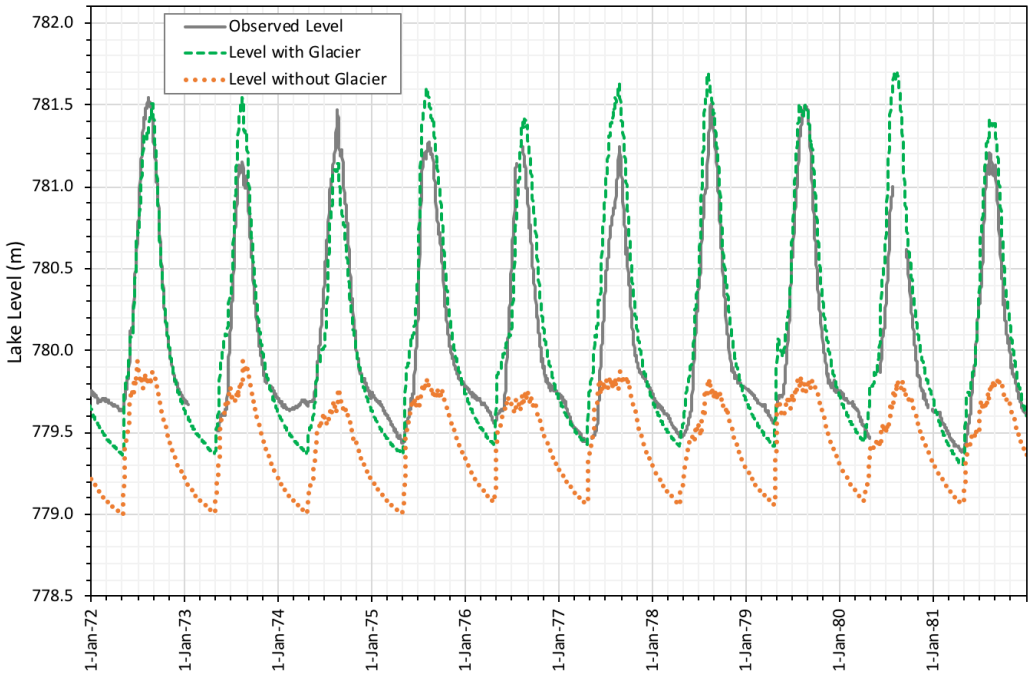

Figure S-4. Kluane Lake simulated versus observed levels – 1972-1981.

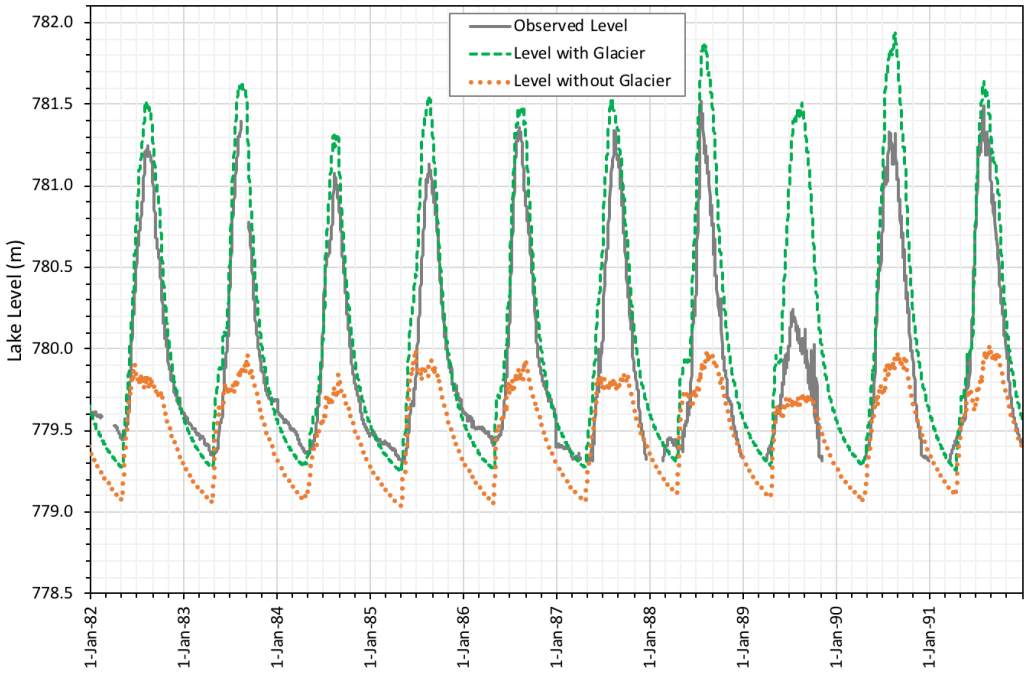

Figure S-5. Kluane Lake simulated versus observed levels – 1982-1991.

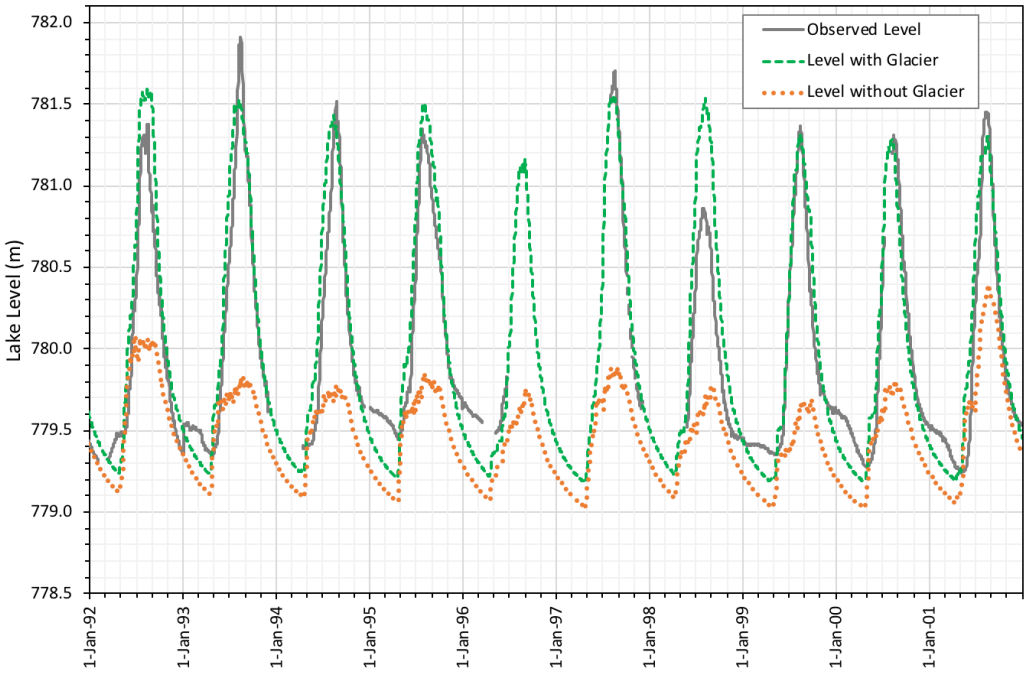

Figure S-6. Kluane Lake simulated versus observed levels – 1992-2001.

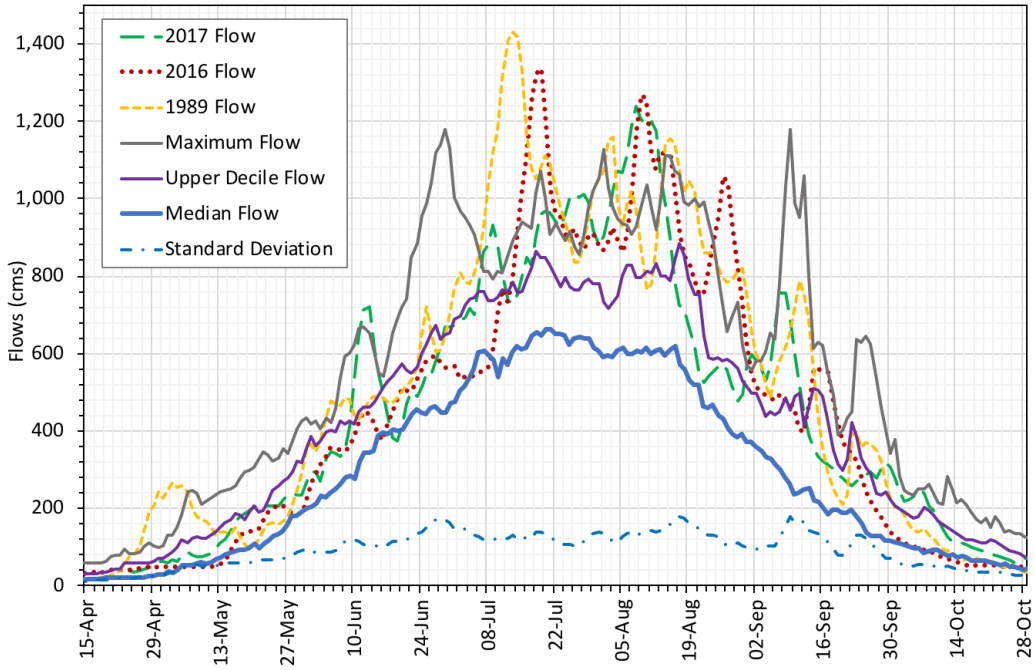

Figure S-7. Alsek River flow minus 1.2 times Dezadeash River flow: piracy years 1989, 2016 and 2017 contrasted to 1974–2015 statistics.

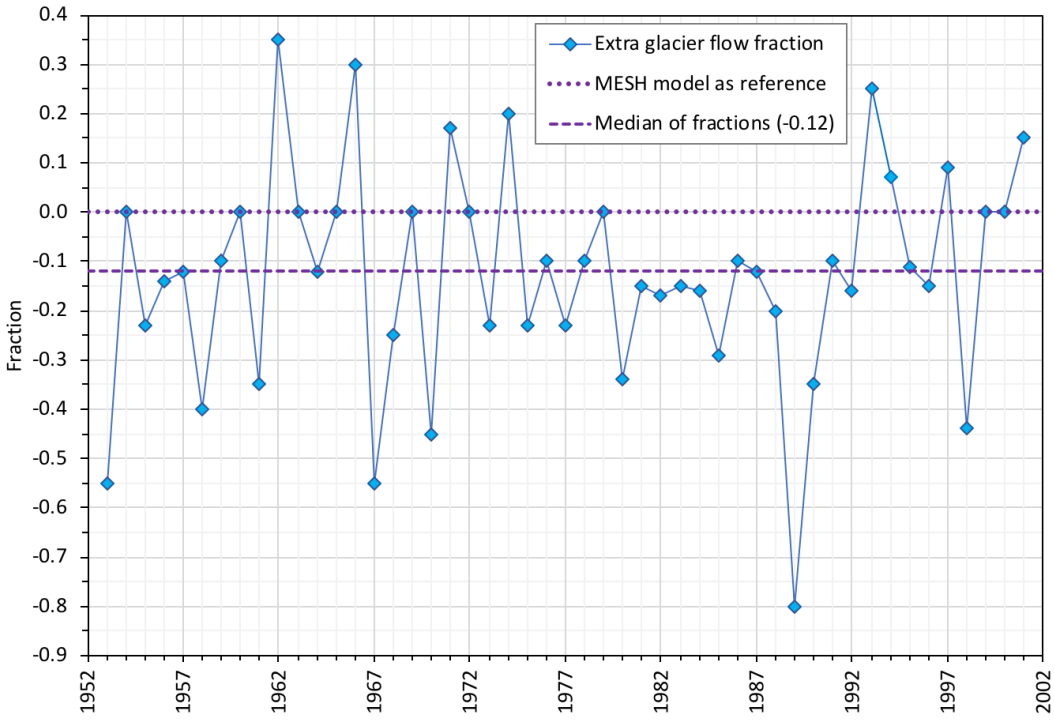

Figure S-8. Gained or lost fraction of Kaskawulsh Glacier flow towards Slims River.

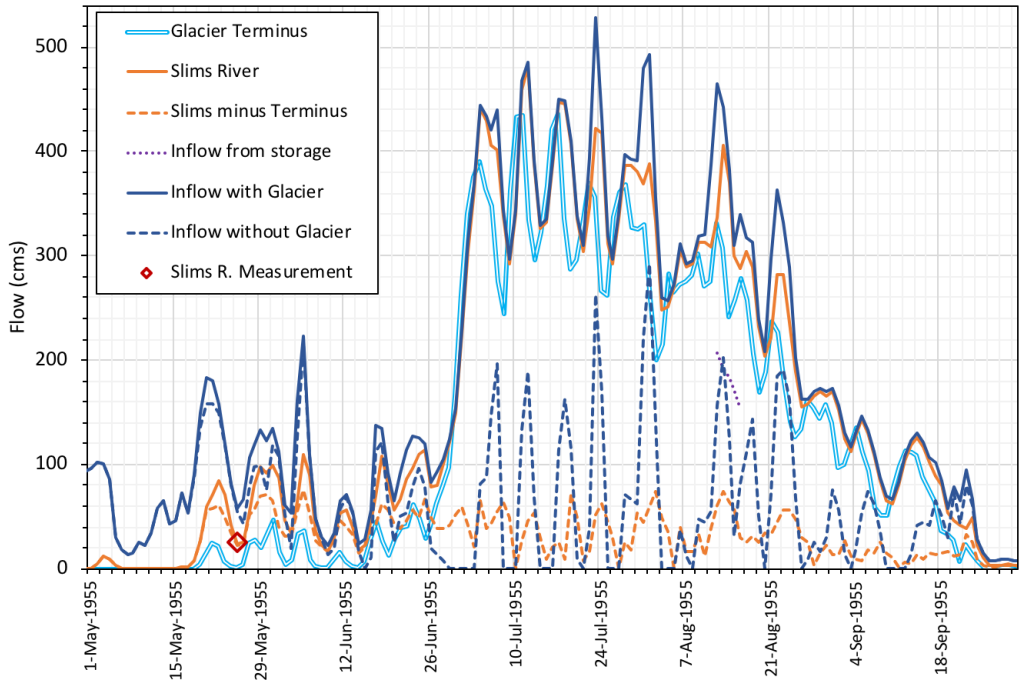

Figure S-9. MESH flow simulation results – 1955.

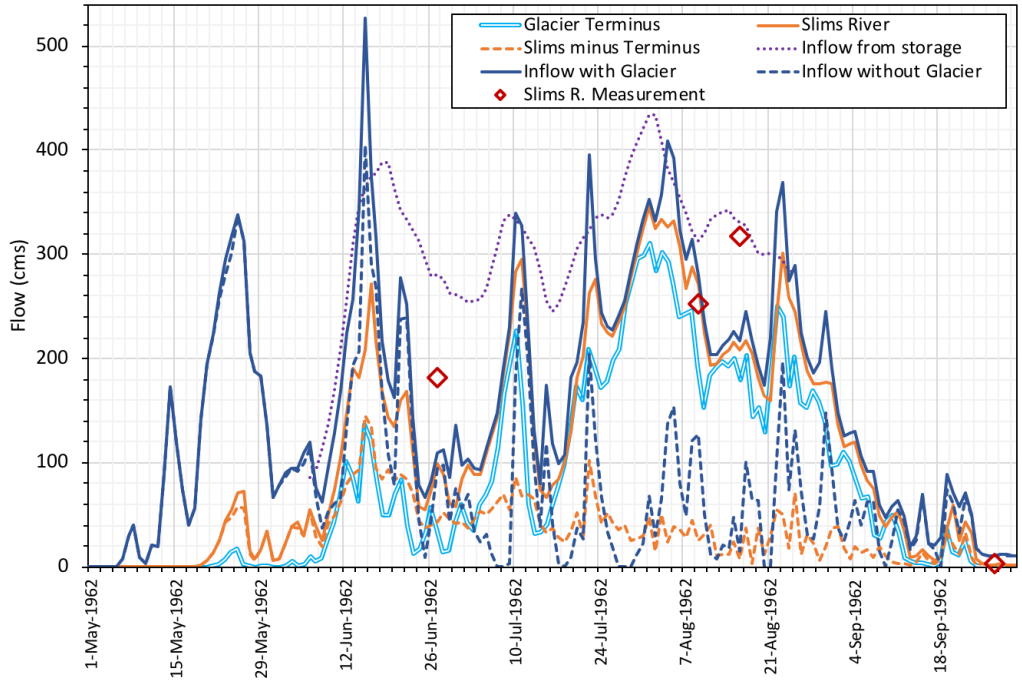

Figure S-10. MESH flow simulation results – 1962.

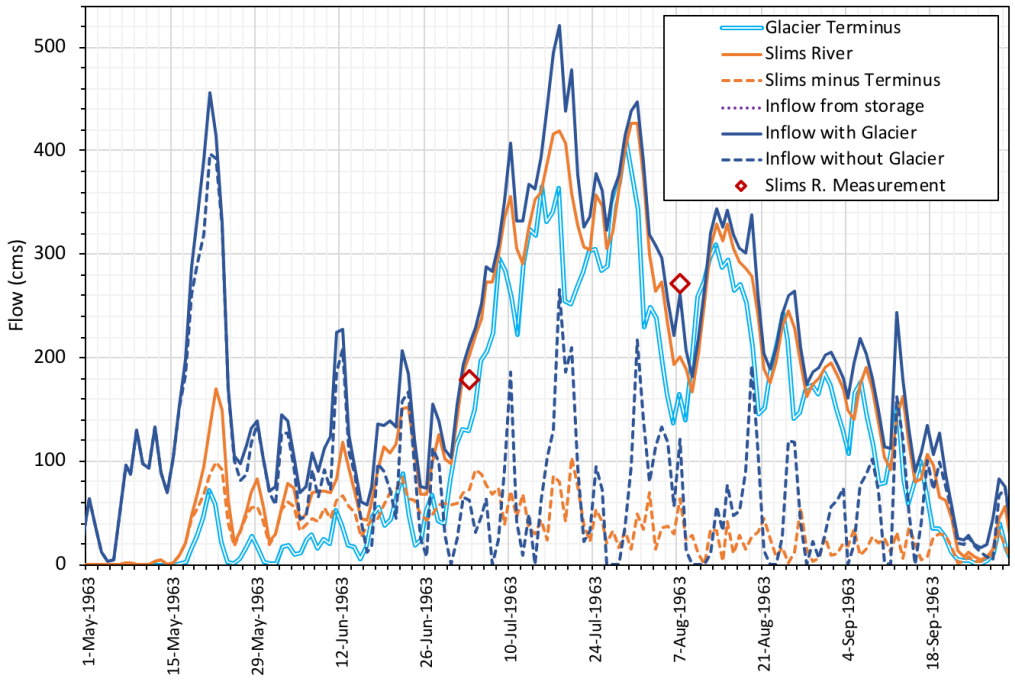

Figure S-11. MESH flow simulation results – 1963.

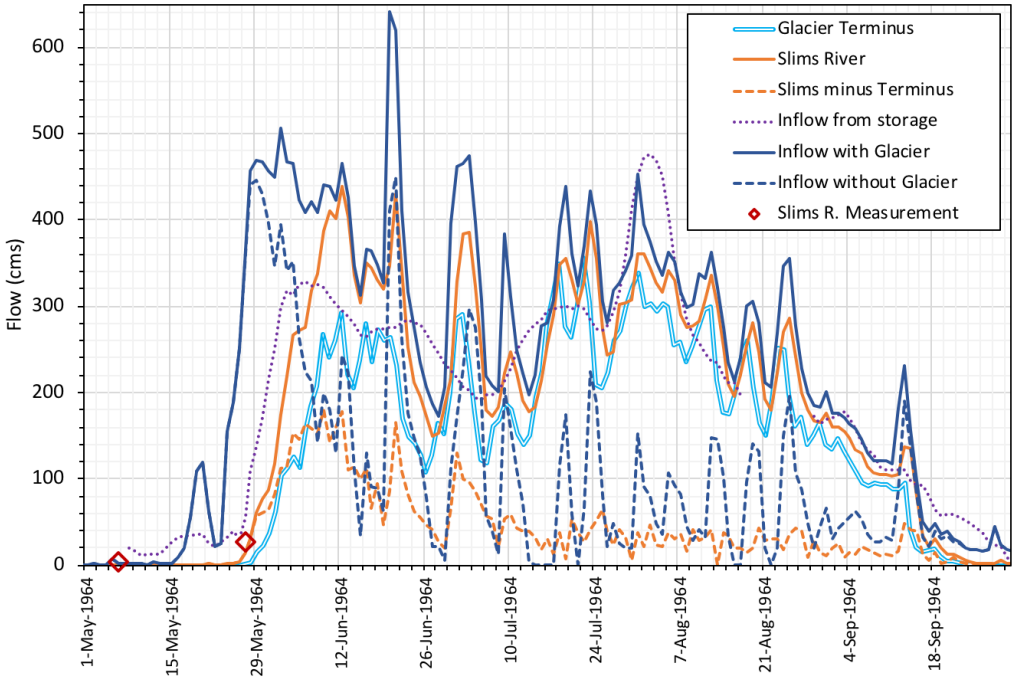

Figure S-12. MESH flow simulation results – 1964.

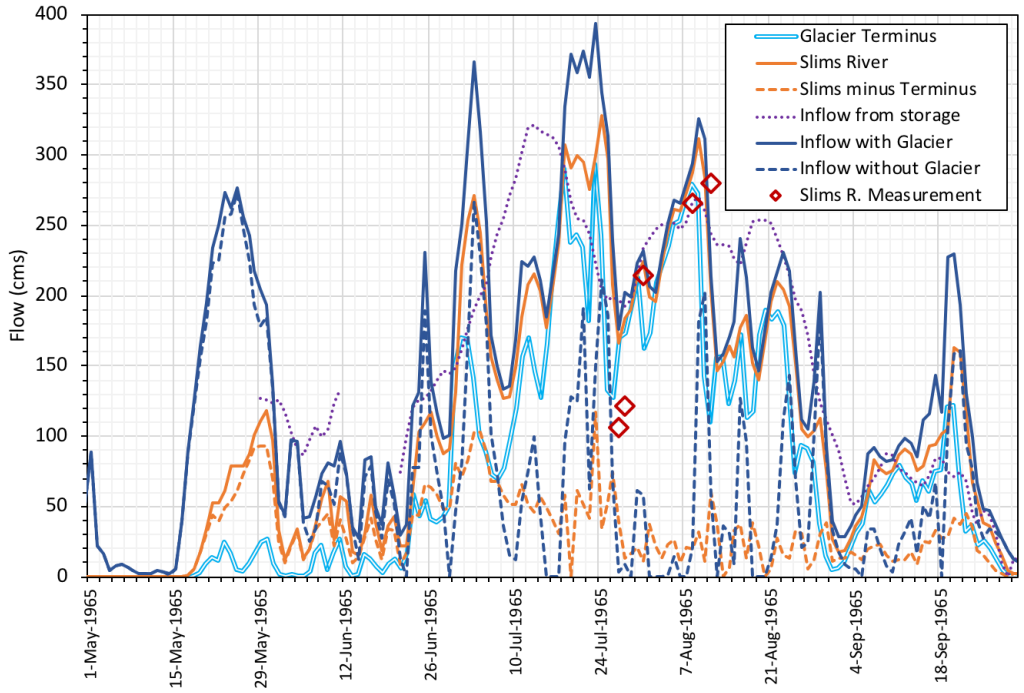

Figure S-13. MESH flow simulation results – 1965.

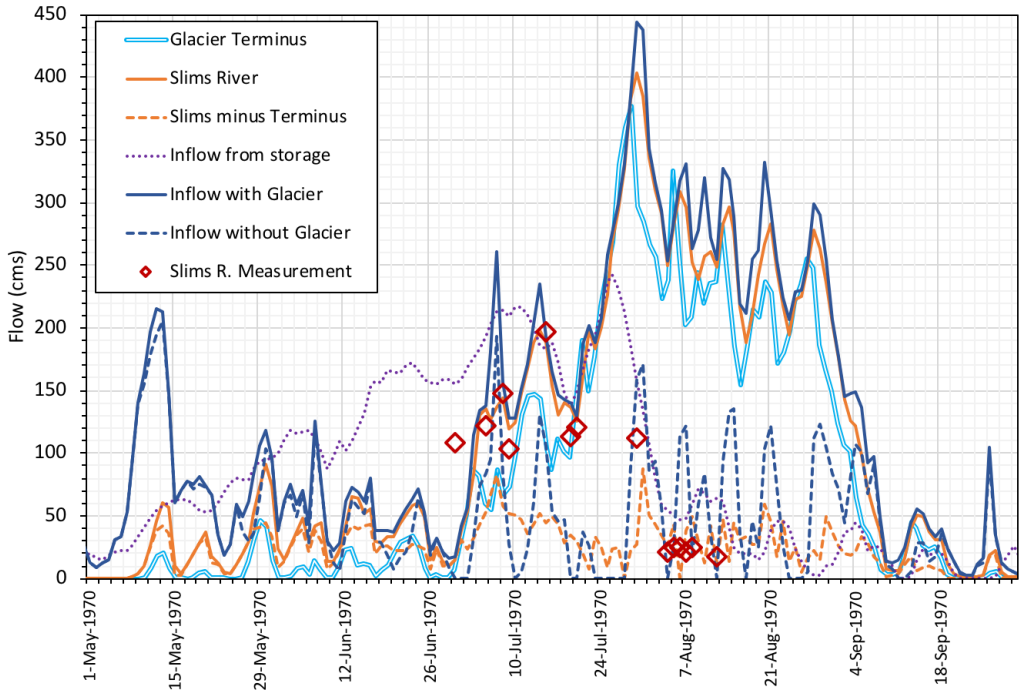

Figure S-14. MESH flow simulation results – 1970.

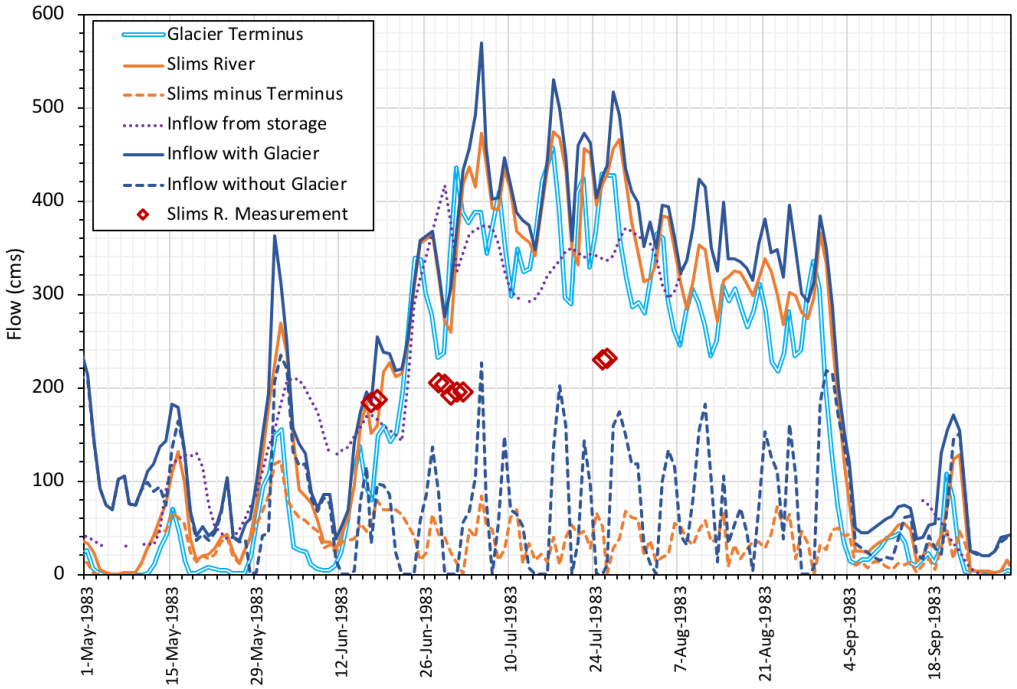

Figure S-15. MESH flow simulation results – 1983.

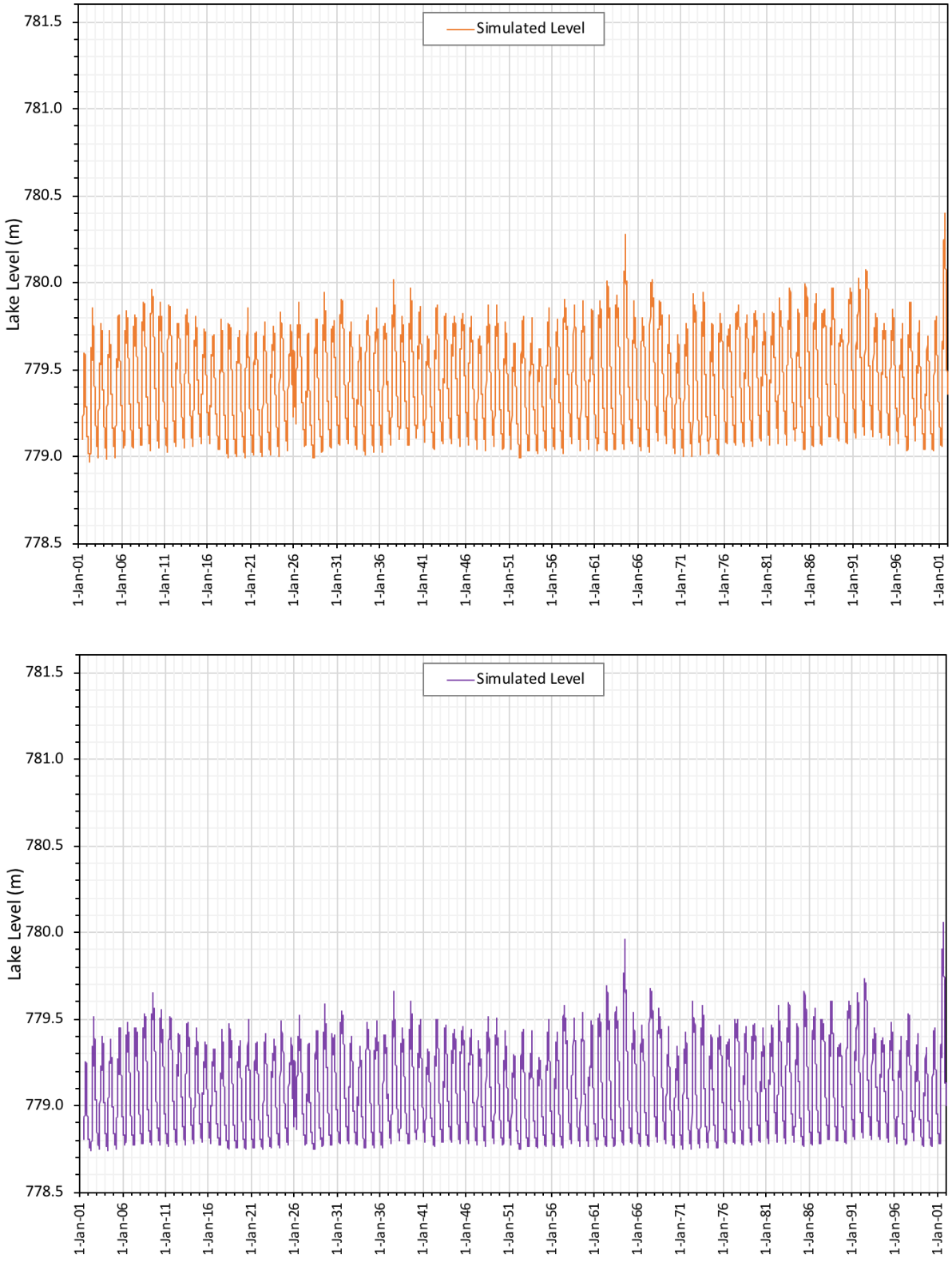

Figure S-16. Kluane Lake simulated levels without the Glacier contribution – 1901-2001. Top: using Estimated 1995 open water RC; bottom: using Estimated current open water RC

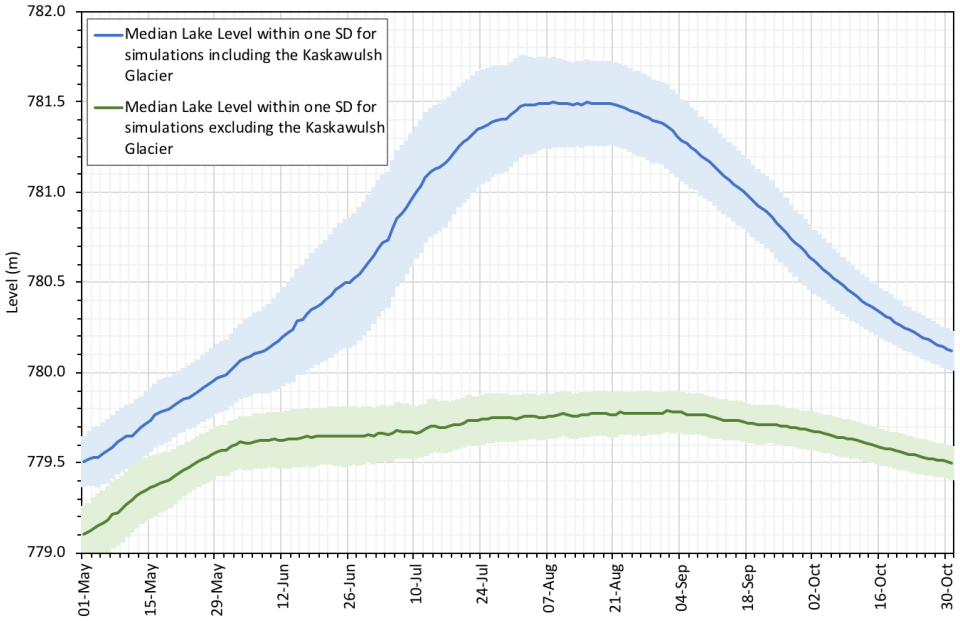

Figure S-17. Kluane Lake median levels with and without the Glacier contribution – 1902-2001 statistics. The Estimated 1995 open water RC is used in the case without glacier

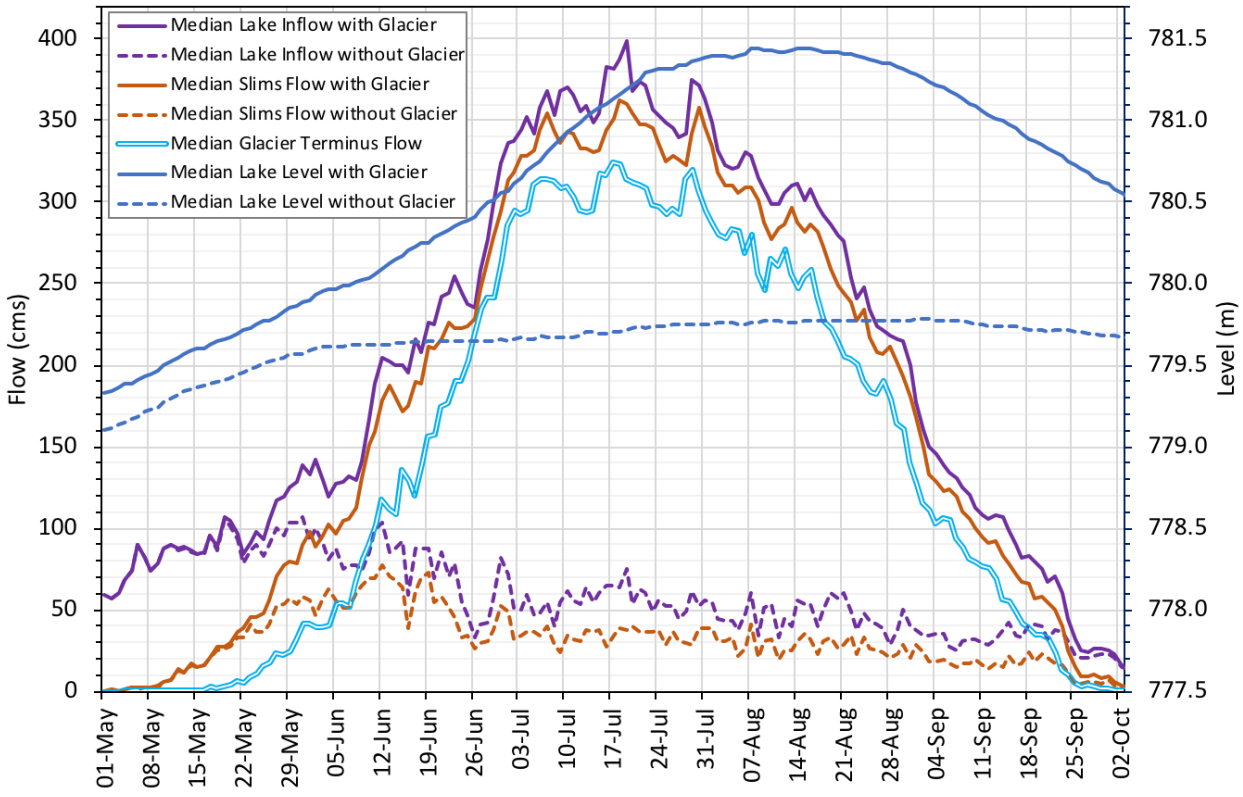

Figure S-18. Kluane Lake median components – 1902-2001 statistics.

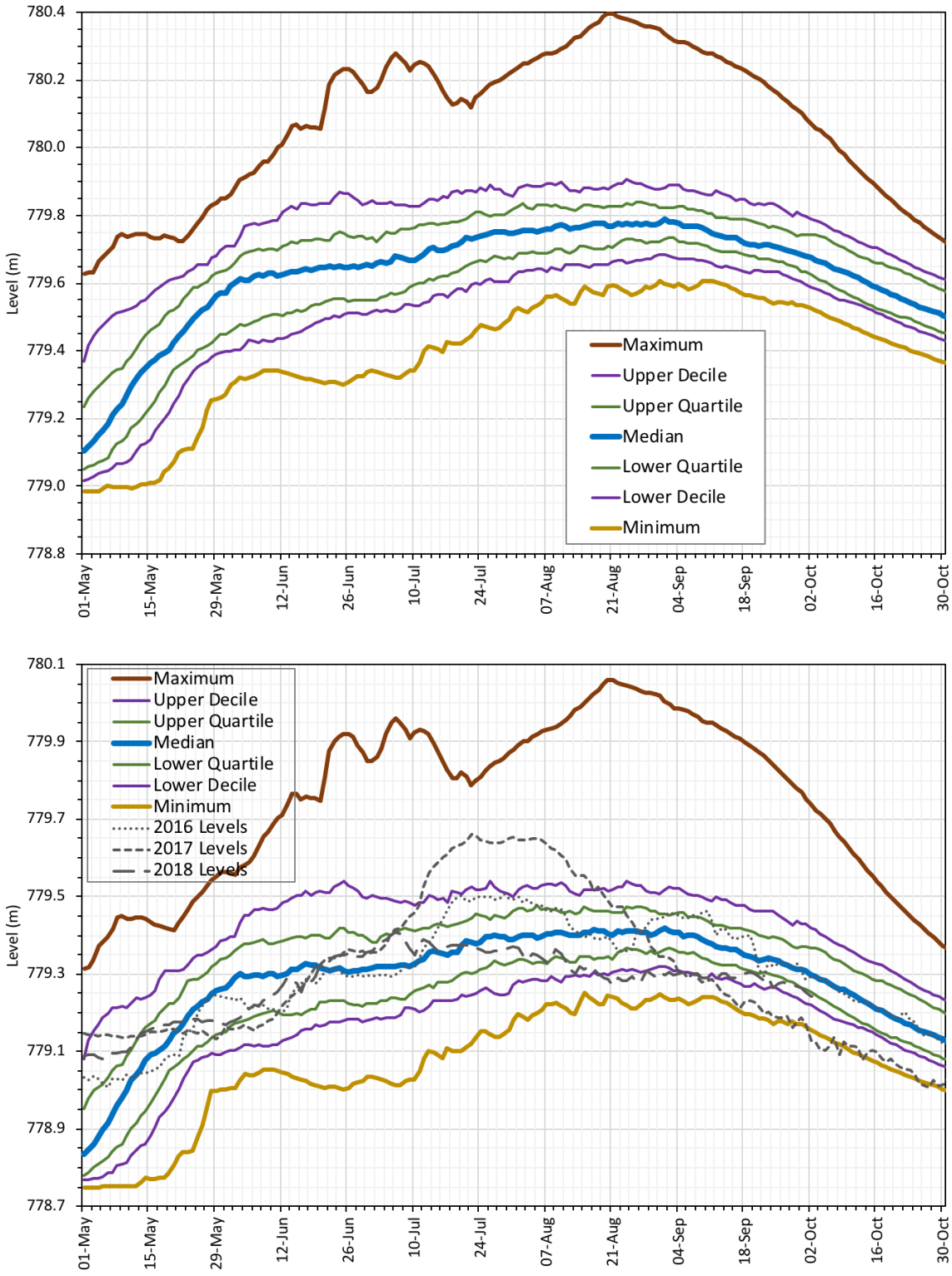

Figure S-19. Kluane Lake levels' percentiles without the Glacier contribution – 1902-2001. Top: using Estimated 1995 open water RC; bottom: using Estimated current open water RC.

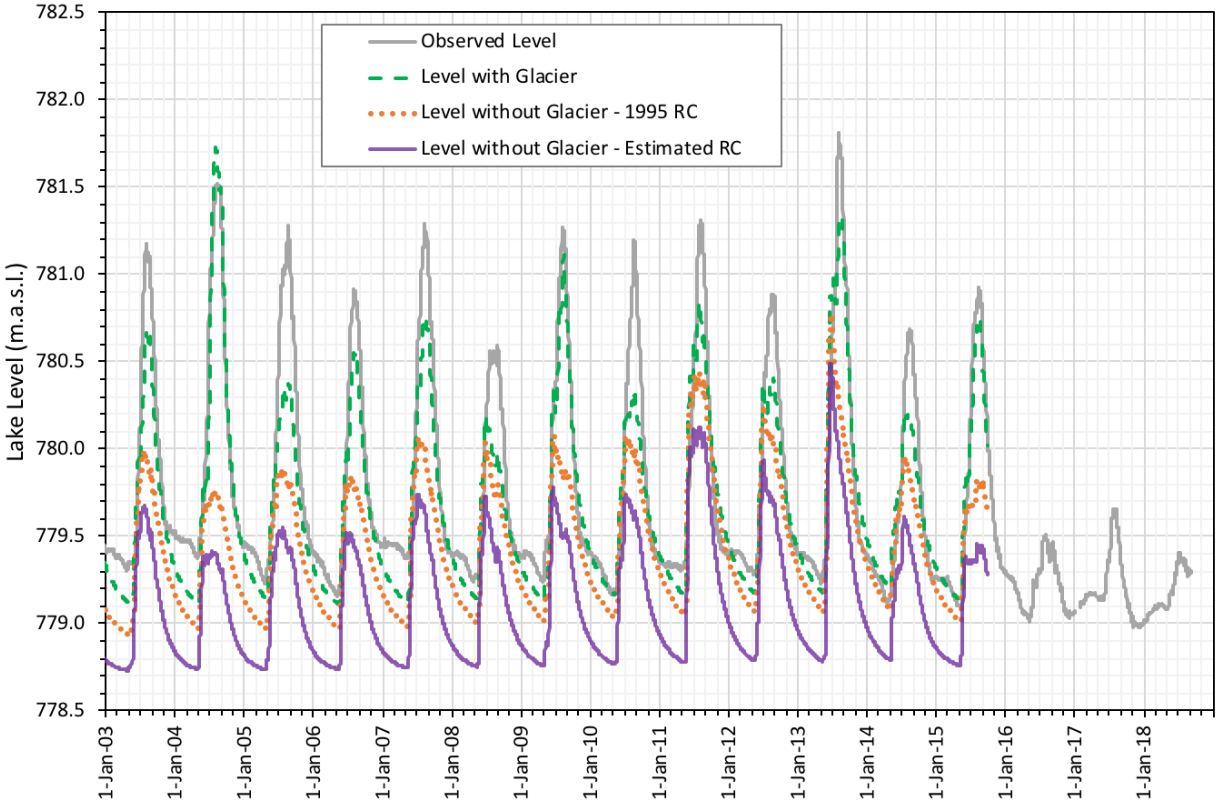

Figure S-20. Kluane Lake simulated levels using Current WRF-GEM-CaPA – 2003-2015.

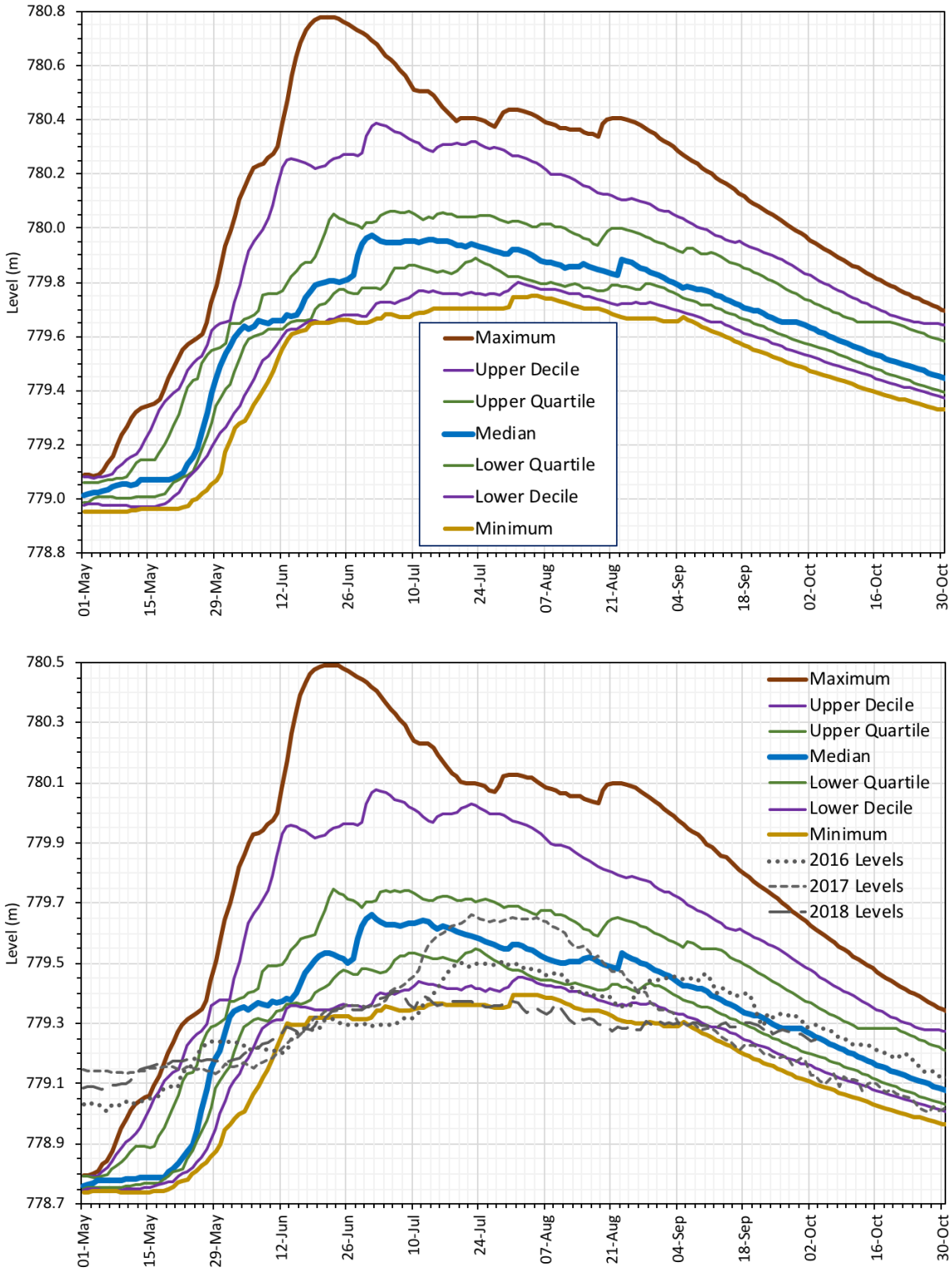

Figure S-21. Kluane Lake levels' percentiles without the Glacier contribution for Current Climate – 2003-2015. Top: using Estimated 1995 open water RC; bottom: using Estimated current open water RC.

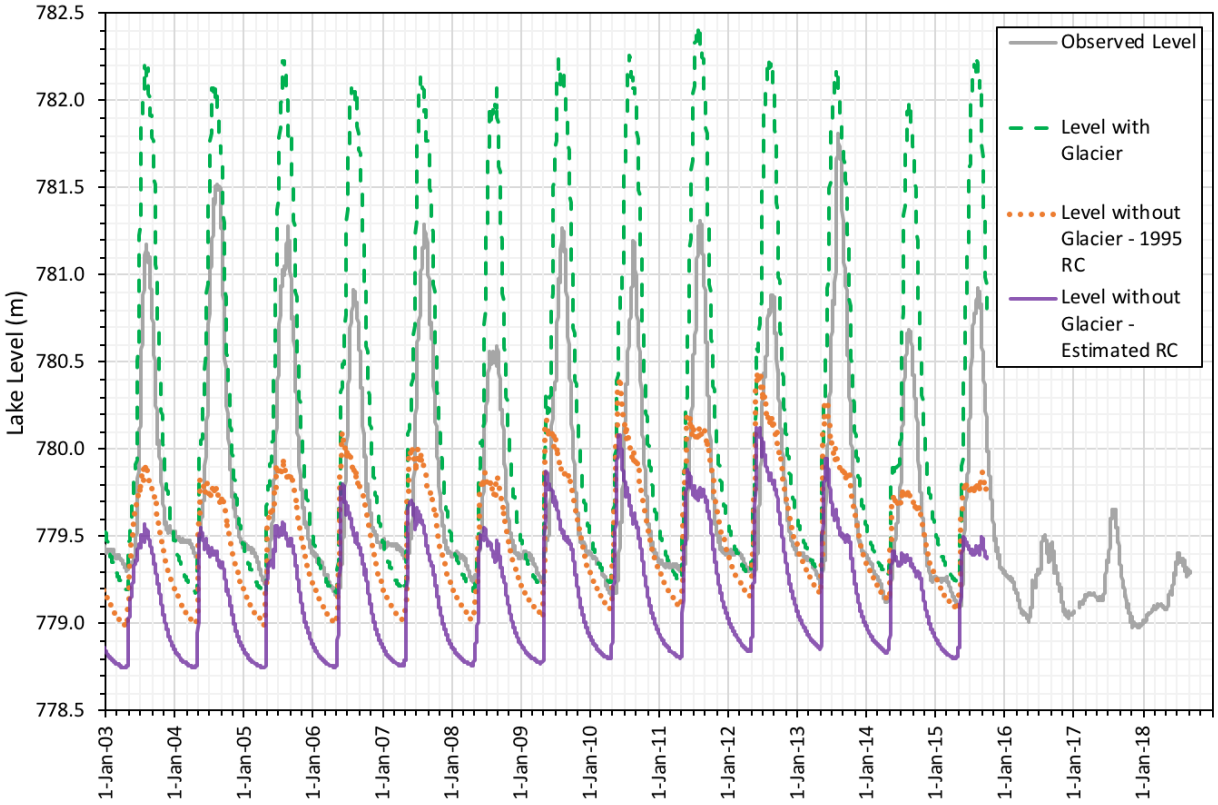

Figure S-22. Kluane Lake simulated levels using Future WRF-GEM-CaPA – 2003-2015.

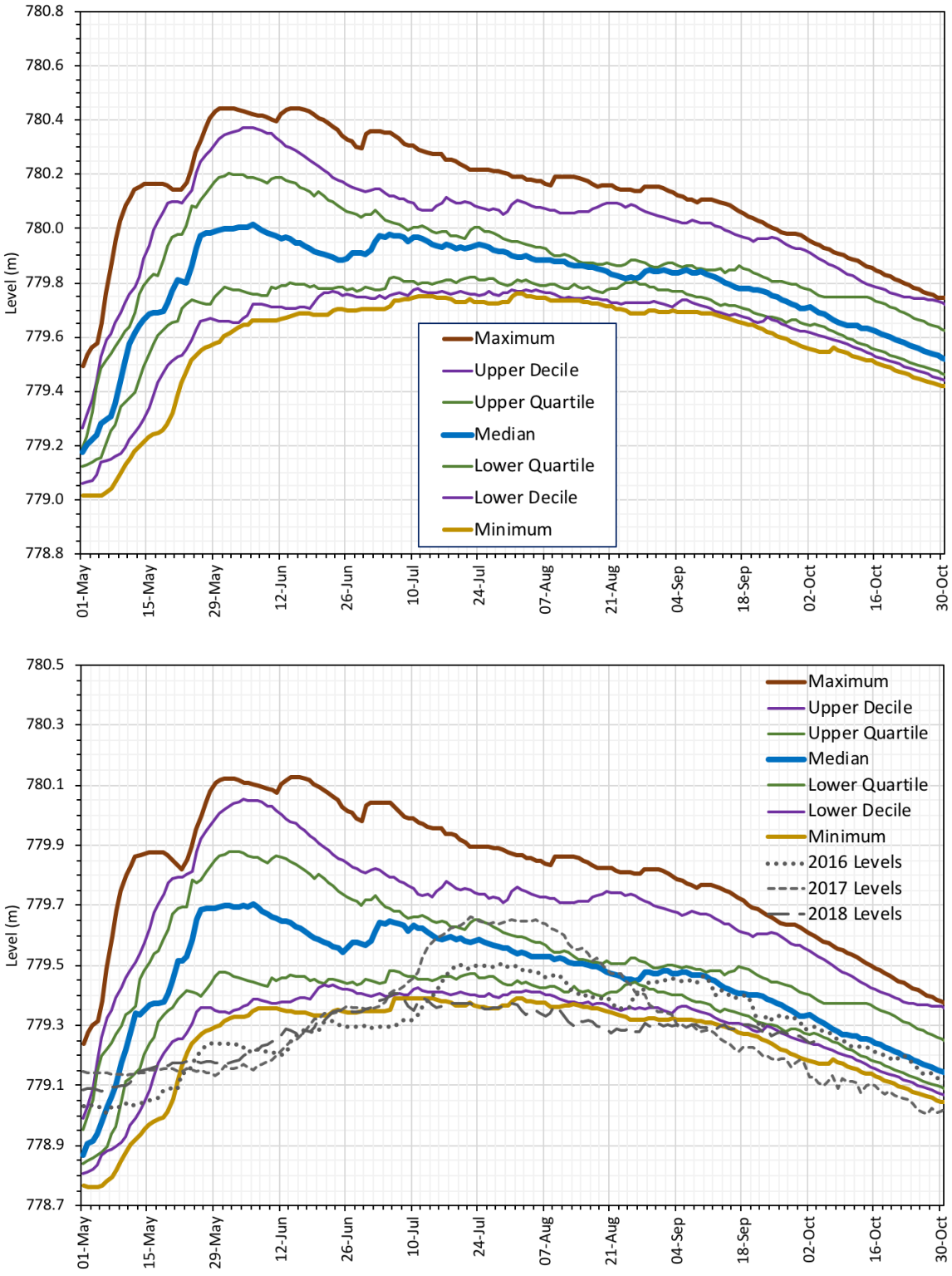

Figure S-23. Kluane Lake levels' percentiles without the Glacier contribution for Future Climate – 2086-2100. Top: using Estimated 1995 open water RC; bottom: using Estimated current open water RC

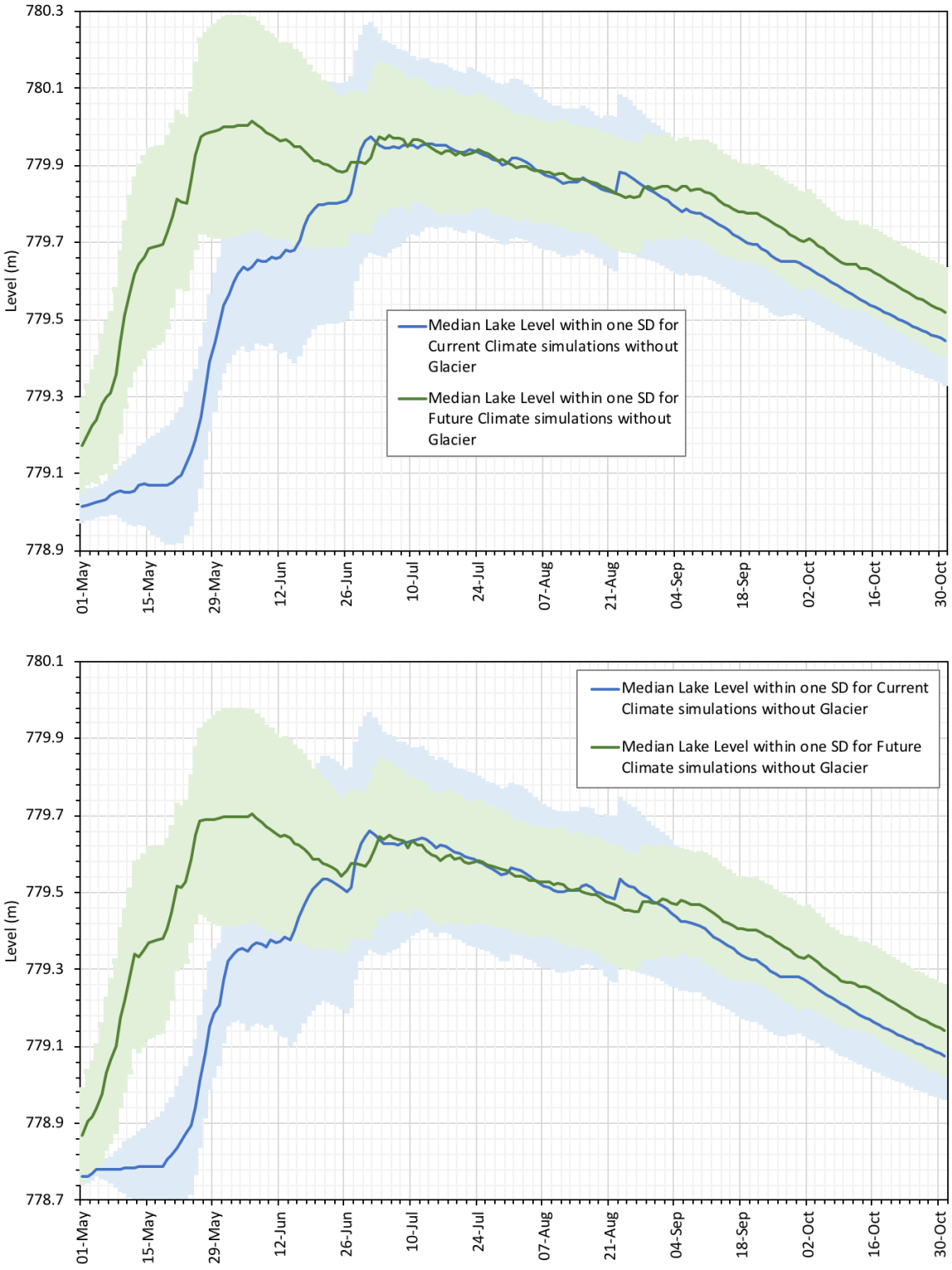

Figure S-24. Kluane Lake levels' medians within one standard deviation, without the Glacier contribution, for Current and Future Climates. Top: using estimated 1995 open water RC; bottom: using estimated current (2015) open water RC

Appendix: CLASS component of MESH

(description drawn from Pomeroy et al., 2016)

It should be noted that CLASS is frequently updated and so new versions may deviate from the following description. CLASS calculates the energy and water balances of the land surface from an initial starting point, making use of atmospheric forcing data to drive the calculation. When CLASS is run in coupled mode with an atmospheric model, the forcing data are passed to it at each time step from the parallel atmospheric model simulation. CLASS then produces surface parameters such as albedo and surface radiative and turbulent fluxes, which are in turn passed back to the atmospheric model. CLASS can also be run in uncoupled or offline mode, with forcing data derived from a separate atmospheric model run or from field measurements.

Mass and Energy Budget Calculation in CLASS

The surface energy balance equation for a non-vegetated surface is:

$$Q^* + H + \lambda E = G_0 \qquad \text{A.1}$$

with the net radiation, Q*:

$$Q^* = K^* + L^* \qquad \text{A.2}$$

where K* and L* are the net shortwave and longwave radiative fluxes, respectively, absorbed at the surface, H is the sensible heat flux, λE is the latent heat flux and G0 is the surface heat flux into the ground or snowpack. K* depends on incoming shortwave radiation, K↓, and surface albedo, α, as:

$$K^* = (1-\alpha) K^{\downarrow} \qquad \text{A.3}$$

L* is calculated as the difference between incoming longwave radiation, L↓, and the radiation emitted by the surface, which is assumed to radiate as a black body:

$$L^* = L^{\downarrow} - \sigma T_0^4 \qquad \text{A.4}$$

where σ is the Stefan-Boltzmann constant and T_0 is the surface temperature. The surface heat flux is calculated from the surface layer temperatures.

CLASS solves the non-linear surface energy balance equation iteratively using the Newton-Raphson method, with a maximum of five iterations. Iterative solutions are also found in BATS, CLM, MAPS, Noah-MP, SiB2, VIC and VISA. The surface temperature, T_0, at each iteration step is updated if the residual of the energy balance, RESID, is greater than 5.0 Wm^{-2}, using:

$$T_0 = T_{0-} - \frac{RESID}{\frac{d\left(\sigma T_0^4\right)}{dT} + \frac{d\left(H\right)}{dT} + \frac{d\left(\lambda E\right)}{dT}} \qquad \text{A.5}$$

where the subscript – denotes values calculated prior to incrementing T_0.

Turbulent Transfer Calculation

First-order closure is most commonly used for estimating turbulent fluxes of heat and moisture between the atmosphere and land surface. The widely applied bulk aerodynamic formulae are given by:

$$H = \rho c_p C_H u\left(z\right)\left[T_0 - T\left(z\right)\right] \qquad \text{A.6}$$

for sensible heat flux (H), and by:

$$\lambda E = \rho L_V C_H u\left(z\right)\left[q_0 - q\left(z\right)\right] \qquad \text{A.7}$$

for latent heat flux (λE). In these equations CH is the scalar transfer coefficient assumed to be the same for both sensible and latent heat at reference height z, u is the wind speed, T is the temperature, and q is the specific humidity with the subscript 0 indicating that it is the state at the surface.

Similarly, the momentum flux (τ) is given by:

$$\tau = -\rho C_D u\left(z\right)^2 = -\rho u_*^2 \qquad \text{A.8}$$

where CD is the drag coefficient and u* is the friction velocity. The drag and transfer coefficients depend on atmospheric stratification, which is commonly parameterized using Monin-Obukhov similarity theory or a Richardson number approach.

Variations of Obukhov length parameterizations are also used in the ECMWF land surface model, CLM, JULES, Noah-MP, SWAP, and VISA. The Obukhov length, L, is the height above which buoyant production of turbulence dominates over shear production. L is used to characterize atmospheric stratification and is given by:

$$L = -\frac{u_*^3 T_v\left(z\right)}{\kappa g Q_{v,0}} \qquad \text{A.9}$$

where κ is the von Kármán constant, T_v is the air virtual temperature, g is acceleration due to gravity and $Q_{v,0}$ is the virtual temperature heat flux at the surface. The drag and scalar exchange coefficients are given by:

$$C_D = \frac{\kappa^2}{\left[ln\left(\frac{z}{z_0}\right) - \psi_m(\zeta) \right]^2} \qquad \text{A.10}$$

$$C_H = \frac{\kappa^2}{\left[ln\left(\frac{z}{z_0}\right) - \psi_m(\zeta) \right]\left[ln\left(\frac{z}{z_{0h}}\right) - \psi_h(\zeta) \right]} \qquad \text{A.11}$$

where z_0 and z_{0h} are the surface roughness lengths for momentum and scalar transfer, respectively, and ψ_m and ψ_h are stability functions for momentum and scalar exchange.

The stability functions are given by the integrals:

$$\psi_{m,h} = \int_0^{z/L} \frac{1-\phi_{m,h}(\zeta)}{\zeta} \mathrm{d}\zeta \qquad \text{A.12}$$

where ϕ_m and ϕ_h are the universal functions for momentum and scalar exchange, respectively. Examples of those used in JULES (Dyer, 1974) for unstable conditions, and in Beljaars and Holtslag (1991) for stable conditions are:

$$\Phi_m(\zeta) = \begin{cases} (1-a\zeta)^{-1/4}, -1 < \zeta < 0 \\ 1+\zeta+b\zeta(c-d\zeta)e^{-d\zeta}, \zeta \geq 0 \end{cases} \qquad \text{A.13}$$

$$\Phi_h(\zeta) = \begin{cases} (1-a\zeta)^{-1/2}, -1 < \zeta < 0 \\ 1+\zeta(1+b\zeta)^{-1/2}+b\zeta(c-d\zeta)e^{-d\zeta}, \zeta \geq 0 \end{cases} \qquad \text{A.14}$$

where $a = 16$, $b = 2/3$, $c = 6$ and $d = 0.35$ are coefficients determined experimentally.

Values for roughness lengths are flow dependent; however, the most common approach used in land surface models is to use a constant value. The roughness length for heat and moisture transfer (z_{oh}) is smaller than that for momentum (z_0); z_{oh} is commonly parameterized as a fraction of z_0. CLASS uses $z_0/z_{oh} = 3.0$ (also in IAP94). JULES and ISBA use $z_0/z_{oh} = 10.0$. The roughness length for momentum of snow is set to 0.001 m, whereas z_0 vegetation are specified parameters.

CLASS does not employ the combination approach to evapotranspiration such as developed by Penman (1948) and enhanced by Monteith (1965). Rather, it uses a Dalton-type bulk transfer approach with adjustments for unsaturated surfaces using resistance formulations to link vegetation and soil to the atmosphere. The surface evaporation efficiency coefficient, β, is used to calculate the soil surface specific humidity and, therefore, affects the magnitude of latent heat fluxes. β characterizes water availability in the near-surface soil layer. If there

is snow cover or water ponded on the surface, then β is set to 1.0 and the surface specific humidity is set to the saturation specific humidity.

CLASS uses the relationship from Lee and Pielke (1992) to calculate β as a function of volumetric soil moisture content θ:

$$\beta = \begin{cases} 1.0, & | \quad \theta_{l,1} > \theta_{fc,1} \\ 0.25\left[1-\cos\left(\pi\dfrac{\theta_{l,1}}{\theta_{fc,1}}\right)\right]^2, & 0.04 \le \theta_{l,1} \le \theta_{fc,1} \\ 0.0, & | \quad \theta_{l,1} < 0.04 \end{cases} \qquad \text{A.15}$$

where $\theta_{fc,1}$ is the field capacity of the first soil layer and is calculated from the soil saturated hydraulic conductivity, which is calculated using the widely applied Clapp and Hornberger (1978) relationships. This cosine relationship is also used in CLM. Alternative parameterizations that focus on critical and wilting points are used in Noah-MP, JULES and MOSES.

Ground Heat Flux

The ground heat flux, G_0, is calculated by deriving a linear equation as a function of T_0 by assuming that the variation of temperature within a soil or snow layer with depth can be expressed using a quadratic equation. For bare ground, the linear equation for G_0 has slope and intercept as functions of the average temperatures, thicknesses, and top and bottom thermal conductivities of the top three soil layers as:

$$G_0 = a_1\overline{T_1} + a_2\overline{T_2} + a_3\overline{T_3} + a_4T_0 + a_5 \qquad \text{A.16}$$

where $\overline{T_1}$, $\overline{T_2}$ and $\overline{T_3}$ are the average temperatures of the first, second and third soil layers, respectively, and the (a_i , $i=1,5$) terms are the coefficients. For snow-covered ground, the linear equation for G_0 has slope and intercept as functions of the average temperature, thickness and thermal conductivity of the snowpack. Snowmelt occurs in two ways: if the solution of the surface energy balance results in $T_0 > 0°C$ or if the energy balance calculations for the snowpack results in a snowpack temperature $T_S > 0°C$.

CLASS uses six soil layers, typically with depths of 0.10, 0.35, 1.10, 2.10, 3.10 and 4.10 m below ground surface. The finite-difference scheme of the one-dimensional heat conservation equation is applied to each soil layer, giving the change in average soil layer temperature, $\overline{T_i}$, over time step $\Delta t = 1800$ s as:

$$\overline{T_i}(t+\Delta t) = \overline{T_i}(t) + \left[G(z_{i-1},t) - G(z_i,t)\right]\frac{\Delta t}{C_i \Delta z_i} \pm S_i \qquad \text{A.17}$$

where $G(z_{i-1}, t)$ and $G(z_i, t)$ are the conductive heat fluxes at the top and bottom of soil layer i, C_i is the soil volumetric heat capacity, Δz_i is the layer thickness and Si is included for cases of freezing or thawing, or groundwater percolation. The conductive heat fluxes between soil layers are calculated from average layer temperatures by assuming that temperatures within each layer vary according to a quadratic function of depth.

Soil

The soil layer moisture contents are calculated using a conservation equation analogous to that for heat. For average layer volumetric liquid water content, $\overline{\theta_{l,i}}$ is:

$$\overline{\theta_{l,i}}(t+\Delta t) = \overline{\theta_{l,i}}(t) + \left[F(z_{i-1},t) - F(z_i,t)\right]\frac{\Delta t}{\Delta z_i} \qquad \text{A.18}$$

where F(zi-1, t) and F(zi, t) are the liquid water flow rates at the top and bottom of soil layer i. Changes in frozen water content, $\overline{\theta_{l,i}}$, occur if $\overline{T_i}(t+\Delta t) > 0°C$ while ice is present, or if $\overline{T_i(t+\Delta t)} < 0°C$ while $\overline{\theta_{l,i}}$ is greater than a limiting value of 0.04. Below the surface, F(zi) are calculated as one-dimensional Darcian fluid flow as used in most land surface models. Soil water vapor movement and liquid water movement according to temperature gradients are ignored. Soil water suction and hydraulic conductivities are calculated based on soil texture from the widely applied Clapp and Hornberger (1978) relationships. F(0) is the infiltration rate at the surface.

Most land surface models have analytical infiltration schemes due to the computationally expensive requirements of numerical schemes. CLASS uses the two-stage Mein and Larson (1973) analytical infiltration parameterization for uniform soils and constant rainfall intensity. Two-stage refers to separate calculations for pre-ponded and ponded infiltration rates, relaxing the Green and Ampt (1911) assumption of constant head at the surface. The infiltration rate is given by:

$$F(0) = \begin{cases} K_w(\psi_W + Z_f)/Z_f, & |\, t < t_p \ (unsaturated) \\ K_w(\psi_W + Z_f + Z_p)/Z_f, & |\, t \geq t_p \ (saturated) \end{cases} \qquad \text{A.19}$$

where KW is the hydraulic conductivity at the wetting front, ψ_w is the soil water potential at the wetting front, Z_f is the infiltration depth and Z_p is the ponding depth, t is the infiltration

time and t_p is the ponding start time. Green–Ampt-type infiltration schemes are used in SWAP and as an option in CRHM.

Zhao and Gray (1997; 1999) used results from a physically based numerical model to develop a general parametric expression for estimating infiltration into frozen soils in prairie and boreal forest environments. The relationship related infiltration to total soil saturation (liquid + frozen water) and temperature at the beginning of snowmelt, the soil surface saturation during melt and the infiltration opportunity time. Infiltration calculations are grouped into three categories:

Restricted – infiltration is completely restricted due to impermeable surface conditions such as ice lens formation;

Limited – capillary flow predominates and infiltration is primarily controlled by soil physical properties; occurs when potential infiltration [equation A.20] is less than liquid water available for infiltration

Unlimited – gravity flow predominates and water infiltrates; occurs when surficial soil is unfrozen, ice lens is absent and soil water holding capacity exceeds potential infiltration.

A parametric equation is used for the limited infiltration case:

$$F(0) = CS_0^{2.92}\left(1 - S_I\right)^{1.64}\left(\frac{273.15 - T_I}{273.15}\right)^{-0.45} t_0^{0.44} \quad T_I \le 273.15 \qquad \text{A.20}$$

where C is an empirical constant equal to 2.10 and 1.14 for prairie and forest soils, respectively, S_0 is the soil surface saturation, $S_I = \theta_I / \theta_0$ is the pre-melt pore saturation of the upper soil layer with θ_I being the volumetric soil moisture (liquid + frozen water) at the start of infiltration, T_I is the pre-melt temperature of the upper soil layer and t_0 is the infiltration opportunity time. t_0 is estimated from SWE as:

$$t_0 = 0.65SWE - 5 \qquad \text{A.21}$$

The maximum amount of water that can infiltrate in the limited case, the water storage potential (W_{sP}), is constrained as:

$$W_{sP} = 0.6\theta_0\left(1 - S_I\right)z_p \qquad \text{A.22}$$

where z_p is depth of a highly permeable surface layer (e.g., thickness of organic layer or depth of surface-connected cracks).

The thermal and hydraulic properties of each of the modelled soil layers are determined differently for different ground types. Soil thermal conductivities are used to calculate heat

fluxes between soil layers, and at the soil-atmosphere and soil-snow interfaces, thus affecting the magnitudes of non-radiative fluxes. CLASS uses the parameterization of Côté and Konrad (2005) for soil thermal conductivity. Soil thermal conductivity, λ_{soil}, is calculated using a relative thermal conductivity, λ_r, which has a value of 0.0 for dry soils, λ_{dry}, and 1.0 at saturation, λ_{sat}:

$$\lambda_{soil} = \left[\lambda_{sat} - \lambda_{dry} \right] \lambda_r + \lambda_{dry} \qquad \text{A.23}$$

λ_r is calculated from the degree of saturation, Sr, as follows

$$\lambda_r = \frac{\breve{} \, S_r}{1 + \left(\breve{} \, - 1 \right) S_r} \qquad \text{A.24}$$

where $\varkappa$ is an empirical coefficient.

λ_{dry} is calculated using an empirical relationship with different coefficients for mineral and organic soils:

$$\lambda_{dry} = 0.75 \exp(-2.76\theta_0) \quad \text{for mineral soils} \qquad \text{A.25}$$

$$\lambda_{dry} = 0.30 \exp(-2.0\theta_0) \quad \text{for organic soils} \qquad \text{A.26}$$

where θ_0 is the soil porosity. λ_{sat} is calculated using the linear averaging approach of de Vries (1963), as suggested by Zhang et al. (2008), rather than geometric averaging used in Côté and Konrad.

$$\lambda_{sat} = \lambda_W \theta_p + \lambda_{soil} (1 - \theta_0) \qquad \text{A.27}$$

$$\lambda_{sat} = \lambda_I \theta_p + \lambda_{soil} (1 - \theta_0) \qquad \text{A.28}$$

where λ_W and λ_I are the thermal conductivities of water and ice, respectively.

Snowpack

The snowpack is modelled as a single layer of variable depth using the same equations for the surface energy balance and heat fluxes as presented previously. Incoming shortwave radiation, K↓, is allowed to penetrate the snow surface, decreases exponentially with depth following Beer's law and can be absorbed by the underlying soil.

Blowing snow involves the horizontal redistribution and sublimation of snow. Despite its importance to mass budgets in high altitude and high latitude cold regions (e.g., Pomeroy

and Li, 2000), these processes have yet to receive widespread parameterization in hydrological models and land surface schemes. Blowing snow calculations are included in a few land surface and hydrological models as options: CRHM and VIC. PBSM calculates blowing snow transport and sublimation rates for steady-state conditions using mass and energy balances. PBSM was initially developed for application over the Canadian Prairies, characterized by relatively flat terrain and homogeneous crop cover. Refer to Pomeroy and Gray (1990), Pomeroy and Male (1992), Pomeroy et al. (1993) and Pomeroy and Li (2000) for details on algorithm development.

PBSM is for fully developed blowing snow conditions and is therefore restricted to minimum fetch distances of 300 m following measurements by Takeuchi (1980). Blowing snow transport fluxes are the sum of snow transport in the saltation and suspension layers, F_{salt} and F_{susp}, respectively. Saltation of snow must be initiated before snow transport can occur in the suspension layer and blowing snow sublimation can occur. F_{salt} is calculated by partitioning the atmospheric shear stress into that required to free particles from the snow surface, to that applied to non-erodible roughness elements (vegetation stalks or shrubs) and to that applied to transport snow particles (Pomeroy and Gray, 1990):

$$F_{salt} = \frac{c_1 e \rho u_t^*}{g}\left(u^{*2} - u_n^{*2} - u_t^{*2}\right) \qquad \text{A.29}$$

where c1 is the dimensionless ratio of saltation velocity to friction velocity ($u_p/u^* = 2.8$), e is the dimensionless efficiency of saltation ($1/4.2u^*$), and u_n^* and u_t^* refer to the portions of u^* applied to non-erodible roughness elements, usually exposed vegetation, and the exposed snow surface itself. u_n^* is calculated using an algorithm developed by Raupach et al. (1993) for wind erosion of soil that relates the partitioning of the shear stress to the geometry and density of roughness elements. u_t^* is calculated based on the air temperature using an empirical equation developed by Li and Pomeroy (1997a). The aerodynamic roughness length differs during blowing snow events from during non-blow snow events. z_0 is controlled by the saltation height and is given by:

$$z_0 = \frac{c_2 c_3 u^{*2}}{2g} + c_4 \beta \qquad \text{A.30}$$

where c_2 is the square root of the ratio of the initial vertical saltating particle velocity to u^*, c_3 is the ratio of z_0 to saltation height (0.07519; Pomeroy and Gray, 1990), c_4 is a drag coefficient for grain stubble (0.5; Lettau, 1969) and β is the dimensionless roughness element density.

Fsusp is calculated as a vertical integration from a reference height near the top of the saltation layer, h^*, to the top of blowing snow boundary layer (z_b), given by Pomeroy and Male (1992):

$$F_{susp} = \frac{u^*}{k} \int_{h^*}^{z_b} \eta(z) ln\left(\frac{z}{z_0}\right) \mathrm{d}z \qquad \text{A.31}$$

where η is the mass concentration of blowing snow (kg m^{-3}) at height z. z_b is governed by the time available for the vertical diffusion of snow particles from h^*, calculated using turbulent diffusion theory and the logarithmic wind profile. h^* increases with friction velocity and is estimated using an empirical equation presented in Pomeroy and Male (1992). For fully developed flow it is constrained at $z_b = 5$ m. Note that as suspended snow diffuses from the saltation layer, saltation must be active for suspension to proceed.

The sublimation of blowing snow particles is calculated as a vertical integration of the sublimation rate of a single ice particle. Assuming particles to be in thermodynamic equilibrium, the sublimation rate of a single ice sphere is controlled by radiative energy exchange, convective heat transfer to the particle, turbulent transfer of water vapor from the particle to the atmosphere and latent heat from sublimation (Schmidt, 1972). Sublimation calculations are highly sensitive to ambient humidity, temperature and wind speed (Pomeroy et al., 1993; Pomeroy and Li, 2000).

Small-scale variations in topography and vegetation result in snow redistribution by wind, interception by vegetation and variable melt rates that produce spatially heterogeneous snow covers. Patchy snow covers ensue as snowmelt progresses and affect both the direction and magnitude of sensible and latent heat fluxes. Most land surface models represent patchy snow covers using snow depletion curves whereby fractional snow-covered area, f_S, is a function of average snow mass or depth. The following linear function is used in CLASS, ECMWF model and SiB2:

$$f_S = \min\left(\frac{d_S}{d_0}, 1\right) \qquad \text{A.32}$$

where d_S is snow depth and d_0 is a threshold parameter set to 0.10 m.

The density of fresh fallen snow affects heat transfer within snowpacks and the atmosphere. There are no physically based parameterizations of fresh snow density in use as they require detailed simulations of crystal size, shape and packing; rather there are a number of empirical functions based on combinations of air temperature, humidity and wind speed. CLASS calculates fresh snow density as a function of air temperature using an equation presented by Hedstrom and Pomeroy (1998):

$$\rho_{S,f} = 67.92 + 51.25 \exp\left(\frac{T(z) - T_m}{2.59}\right) \qquad \text{A.33}$$

for air temperatures below 0°C, and using an equation from Pomeroy and Gray (1995):

$$\rho_{S,f} = 119.17 + 20.0\left(T(z) - T_m\right) \qquad \text{A.34}$$

for air temperatures at or above 0°C.

Snow density generally increases over time due to grain metamorphism, compaction from the weight of overlying snow and the refreezing of meltwater. Snow density is commonly used to parameterize thermal conductivity, liquid water content and, indirectly, snow cover fraction (Pomeroy and Brun, 2001). CLASS uses an empirical equation in which the density of snow, ρ_S, increases exponentially from the fresh snow value, $\rho_{S,f}$, to a maximum possible snow density, $\rho_{S,max}$.

$$\frac{d\rho_S}{dt} = \frac{0.01\left(\rho_S - \rho_{S,max}\right)}{3600} \quad \text{A.35}$$

$$\rho_S\left(t+\Delta t\right) = \rho_{S,max} + \left[\rho_S\left(t\right) - \rho_{S,max}\right]\exp\left(\frac{-0.01\Delta t}{3600}\right) \quad \text{A.36}$$

where the value 0.01/3600 is an empirically determined time scale. The maximum snow density is calculated from snow depth following Tabler et al. (1990):

$$\rho_{S,max} = A_S - \frac{204.70}{d_S}\left[1.0 - exp\left(\frac{d_S}{0.673}\right)\right] \quad \text{A.37}$$

where AS is set to 700.0 kg m^{-3} for snowpacks near 0°C, and to 450.0 kg m^{-3} for colder snowpacks following Brown et al. (2006). Similar empirical parameterizations are used in the ECMWF land surface model and ISBA.

Snow albedo exerts a strong control on the timing of snowmelt and land surface-climate feedbacks. Albedo depends on physical characteristics of snowpacks (i.e., grain structure, depth, contaminants) and also on the solar angle and spectral distribution of radiation. In CLASS, snow albedo is modelled using empirical exponential decay functions. Snow albedo, α_S, decreases exponentially from a fresh snow value of 0.84 using the function

$$\alpha_S\left(t+\Delta t\right) = \left[\alpha_S\left(t\right) - \alpha_{S,old}\right]\exp\left(-\frac{0.01\Delta t}{3600}\right) \quad \text{A.38}$$

where $\Delta t = 1800$ s. The background old snow albedo, $\alpha_{S,old}$, is set to 0.50 if the melt rate is non-negligible or the snowpack temperature is greater than -0.01°C, otherwise $\alpha_{S,old} = 0.70$. The snow albedo is reset to 0.84 if a snowfall greater than or equal to 0.1 mm occurs. Similar empirical parameterizations are used in ISBA, the ECMWF land surface model and Noah-MP.

The thermal conductivity of snow, λ_S, is used along with the vertical temperature gradient to calculate the heat flux through the snowpack. Most models parameterize an effective thermal conductivity as a quadratic or power function of snow density. CLASS uses an empirical equation from Sturm et al. (1997):

$$\lambda_S = \begin{cases} 3.233\times10^{-6}\rho_S^2 - 1.01\times10^{-3}\rho_S + 0.138, & |\rho_S \geq 156.0 \\ 0.234\times10^{-3}\rho_S + 0.023, & |\rho_S < 156.0 \end{cases} \quad \text{A.39}$$

The retention of liquid water in snowpacks controls the timing of runoff. Gravitational drainage of liquid water from snowpacks can be rapid due to high porosity and preferential flow pathways, and capillary forces maintain an irreducible water content. Some highly detailed snow models calculate vertical water velocities; however, this can make a model much more computationally expensive, potentially unstable and differences are only realized on short time scales. Rather, most land surface models drain liquid water from snowpacks once a holding capacity is exceeded. CLASS uses a constant snowpack maximum liquid water retention capacity $\gamma_{w,max}$ = 4% by weight. Noah-MP also uses a constant maximum liquid water retention capacity.

Vegetation and Transpiration

In 1802, Dalton showed the rate of evaporation from a water surface is directly proportional to the differences between the saturation vapor pressures at the surface temperature of the water and the dew point of the air (Penman, 1947). In CLASS, surface temperature is used to estimate the saturated specific humidity at the surface of the canopy. The implicit assumption in this method is that leaf sub-stomatal cavities are saturated at the temperature of the leaf surface (Verseghy et al., 1993). The humidity gradient can then be determined between the surface and that measured at some reference height above the surface from the air temperature and relative humidity. The flux of water vapor along this gradient also takes into consideration the aerodynamic resistance of the canopy via turbulent transfer and the logarithmic wind profile and the canopy resistance.

This Dalton-type approach is widely used for estimating surface fluxes and is commonly applied in land surface parameterization schemes (Mahrt, 1996; Sellers et al., 1997). This may be attributed in part because the method: 1) can be relatively simple to apply, 2) is driven by surface temperature, which is commonly diagnosed by iterative solutions to the surface energy balance in land surface schemes and 3) provides a direct estimate of the flux-gradient between the surface and atmosphere. The BT method may also be applied to both land surfaces and open water surfaces and has the potential for directly integrating remotely sensed surface temperature data, obtained via field measurements or derived from airborne or satellite imagery.

Based on the model diagnosis of surface temperature from an iterative solution to closing the surface energy balance, the parameterization requires measurements or estimates of air density, surface temperature, vapor pressure, wind speed, vegetation height and soil moisture used in the calculation of r_c :

$$E = \frac{\lambda\rho(q_s(T_s) - q)}{r_a + r_c} \quad \text{A.40}$$

where q_s is the saturated specific humidity (kg kg^{-1}) at the surface temperature (T_s) and q is the specific humidity of the air (kg kg^{-1}).

Application of Equation A.40 to nonsaturated surfaces requires consideration of the resistances of water vapor transfer to the atmosphere. Estimates of the aerodynamic resistance are obtained assuming a logarithmic wind profile formulation:

$$r_a = \frac{\left[\ln \frac{(z-d)}{z_0}\right]^2}{k^2 u} \qquad \text{A.41}$$

where u is the wind speed at the reference height, z, d = 0.67h is the displacement height of the vegetation (m) and k is the von Kármán constant (0.41). Estimates of canopy resistance are obtained using the general model proposed by Jarvis (1976) and the experimental relationships developed by Verseghy et al. (1993) for the multiplicative factors describing environmental stress effects on stomatal control:

$$r_c = r_{cmin} f_1 f_2 f_3 f_4 \qquad \text{A.42}$$

where r_{cmin} represents the minimum unstressed canopy resistance (s m^{-1}). The multiplicative factors describe stomatal control as a representative value of 1 under what may be considered optimal conditions for plant growth and a value >1 under stressed conditions. f_1 increases under conditions when light is limiting and is a function of the incoming solar radiation, K↓ (W m^{-2}), required for photosynthesis:

$$f_1(\mathrm{K}\downarrow) = \max\left(1.0, \left(500 / \mathrm{K}\downarrow - 1.5\right)\right). \qquad \text{A.43}$$

f_2 is a function of the vapor pressure, e, deficit (m_b) required to maintain water and nutrient uptake to the plant, which increases as the plants ability to transmit water from the soil rooting zone is exceeded:

$$f_2(\Delta e) = \max(1.0, (\Delta e / 5.0)). \qquad \text{A.44}$$

f_3 is a function of soil moisture supply, specifically the soil moisture tension, ψ (m), which increases with decreasing soil moisture:

$$f_3(\psi) = \max(1.0, \psi / 40.0) \qquad \text{A.45}$$

where ψ is derived using the Campbell power law function for specific soil texture classes based on the air entry tension, ψ_{ae}, porosity, φ, a pore size distribution index, b, and soil moisture, θ, (Campbell, 1974):

$$\psi = \psi_{ae}\left(\frac{\varphi}{\theta}\right)^{b} \quad \text{A.46}$$

f4 is a function of temperature with an operating range between 0 and 40°C:

$$f_4(T) = 1.0 \text{ if T} < 40°\text{C or} > 0°\text{C} \quad \text{A.47}$$

or

$$f_4(T) = 5000/r_{c\,min} \text{ if T} > 40°\text{C or} < 0°\text{C}$$

and indexes the range of temperatures at which transpiration may be considered to occur.

Appendix References

Beljaars, A. C. M. and Holtslag, A. M. (1991). Flux parameterization over land surfaces for atmospheric models. *Journal of Applied Meteorology,* **30,** 327-34.

Brown, R., Bartlett, P., Mackay, M. and Verseghy, D. (2006). Estimation of snow cover in CLASS for SnowMIP. *Atmosphere-Ocean,* **44,** 223-38.

Campbell, G. S. (1974). A simple method for determining unsaturated conductivity from moisture retention data. *Soil Science,* **117(6),** 311-14.

Clapp, R. B. and Hornberger, G. M. (1978). Empirical equations for some soil hydraulic properties. *Water Resources Research,* **14,** 601-4.

Côté, J. and Konrad, J. M. (2005). A generalized thermal conductivity model for soils and construction materials. *Canadian Geotechnical Journal,* **42,** 443-58.

De Vries, D. A. (1963). Thermal properties of soils. In *Physics of Plant Environment,* ed. W. R. van Wijk. Amsterdam: North-Holland Publishing Company, pp. 210-35.

Dyer, A. J. (1974). A review of flux-profile relationships. *Boundary-Layer Meteorology,* **7,** 363-72.

Green, W. H. and Ampt, G. (1911). Studies of soil physics, part I - the flow of air and water through soils. *Journal of Agricultural Science,* **4,** 1-24.

Hedstrom, N. R. and Pomeroy, J. W. (1998). Measurements and modelling of snow interception in the boreal forest. *Hydrological Processes,* **12,** 1611-25.

Jarvis, P. G. (1976). The interpretation of the variations in leaf water potential and stomatal conductance found in canopies in the field. *Philosophical Transactions of the Royal Society of London Series B-Biological Sciences, A Discussion on Water Relations of Plants,* **273,** 593-610.

Lee, T. J. and Pielke, R. A. (1992). Estimating the soil surface specific humidity. *Journal of Applied Meteorology,* **31,** 480-4.

Lettau, H. (1969). Note on aerodynamic roughness-parameter estimation on the basis of roughness element description. *Journal of Applied Meteorology,* **8,** 828-32.

Li, L. and Pomeroy, J. W. (1997). Estimates of threshold wind speeds for snow transport using meteorological *data. Journal of Applied Meteorology,* **36,** 205-13.

Mahrt, L. (1996). The bulk aerodynamic formulation over heterogeneous surfaces. *Boundary-Layer Meteorology,* **78**, 87-119.

Mein, R. G. and Larson, C. L. (1973). Modeling infiltration during a steady rain. *Water Resources Research,* **9**, 384-94.

Monteith, J. L. (1965). Evaporation and environment. *Symposia of the Society for Experimental Biology,* **19**, 205-34.

Penman, H. L. (1947). Evaporation in nature. *Reports on Progress in Physics,* **11**, 366-88.

Penman, H. L. (1948). Natural evaporation from open water, bare soil and grass. *Proceedings of the Royal Society of London Series A, Mathematical and Physical Sciences,* **193**, 120-46.

Pomeroy, J. W. and Brun, E. (2001). Physical properties of snow. In *Snow Ecology: an Interdisciplinary Examination of Snow-Covered Ecosystems,* ed. H. G. Jones, J. W. Pomeroy, D. A. Walker and R. W. Hoham. Cambridge, UK: Cambridge University Press, pp. 45-118.

Pomeroy, J. W. and Gray D. M. (1990). Saltation of snow. *Water Resources Research,* **26**, 1583-94.

Pomeroy, J. W. and Gray, D. M. (1995). *Snowcover Accumulation, Relocation and Management. National Hydrology Research Institute Science Report No.* **7**. Saskatoon, SK: Environment Canada.

Pomeroy, J. W. and Li, L. (2000). Prairie and arctic areal snow cover mass balance using a blowing snow model. *Journal of Geophysical Research D: Atmospheres,* **105(D21)**, 26619-34.

Pomeroy, J. W. and Male D. H. (1992). Steady-state suspension of snow. *Journal of Hydrology,* **136**, 275-301.

Pomeroy, J. W., Gray, D. M. and Landine, P. G. (1993). The Prairie Blowing Snow Model: characteristics, validation and operation. *Journal of Hydrology,* **144**, 165-92.

Raupach, M. R., Gillette, D. A. and Leys, J. F. (1993). The effect of roughness elements on wind erosion threshold. *Journal of Geophysical Research D: Atmospheres,* **98**, 3023-9.

Schmidt, R. A. (1972). *Sublimation of Wind-transported Snow - a Mode!.* Forest Service Research Paper RM-90. Fort Collins, CO: Rocky Mountain Forest and Range Research Station, United States Department of Agriculture.

Sellers, P. J., Dickinson, R. E., Randall, D. A. *et al.* (1997). Modeling the exchanges of energy, water, and carbon between continents and the atmosphere. *Science,* **275**, 502-9.

Sturm, M., Holmgren, J., Konig, M. and Morris, K. (1997). The thermal conductivity of seasonal snow. *Journal of Glaciology,* **43**, 26-41.

Tabler, R. D., Benson, C. S., Santana, B. W. and Ganguly, P. (1990). Estimating snow transport from wind speed records: estimates versus measurements at Prudhoe Bay, Alaska. In *Proceedings of the 58th Western Snow Conference,* 17-19 April 1990, Sacramento, CA, pp. 61-78.

Takeuchi, M., Vertical profiles and horizontal increase of drift snow transport, J. *Glaciol.*, **26(94)**, 481-492, 1980.

Verseghy, D. L., McFarlane, N. A. and Lazare, M. (1993). A Canadian land surface scheme for GCMs: II. Vegetation model and coupled runs. *International Journal of Climatology,* **13**, 347-70.

Zhang, Y., Carey, S. K. and Quinton, W. L. (2008). Evaluation of the simulation algorithms and parameterization methods for ground thawing and freezing in permafrost regions. *Journal of Geophysical Research,* **113**.

Zhao, L. and Gray, D. M. (1997). A parametric expression for estimating infiltration into frozen soils. *Hydrological Processes,* **11**, 1761-75.

Zhao, L. and Gray, D. M. (1999). Estimating snowmelt infiltration into frozen soils. *Hydrological Processes,* **12**, 1827-42.

References

Barnett, A.P. (1974). Hydrological studies of the Slims River, Yukon, June-August 1970. In *Icefields Ranges Research Project, Scientific Results*, ed. V.C. Bushnell and M.G., Marcus. American Geographical Society, New York and Arctic Institute of North America, Montreal, Quebec, **Vol. 4**, pp. 143-150.

Bostock, H.S. (1969). Kluane Lake, Yukon Territory, its drainage and allied problems. *Geological Survey of Canada*. Paper 69-28.

Brabets, T. P., Wang, B., and Meade, R. H. (2000). Environmental and hydrologic overview of the Yukon River Basin, Alaska and Canada. USGS Water-Resources Investigations Report 99-4204, Anchorage, Alaska.

Bryan, M. L. (1972). Variations in quality and quantity of Slims River water, Yukon Territory. *Can. J. Earth Sci.*, **9**, 1469-1478.

Cannon, A.J. (2018). Multivariate quantile mapping bias correction: An N-dimensional probability density function transform for climate model simulations of multiple variables. *Climate Dynamics*, **50(1-2)**, 31-49.

Donald, J.R. (1992). Snowcover depletion curves and satellite snow-cover estimates for snowmelt runoff modelling. Ph.D. Thesis, University of Waterloo, Ontario, Canada, 232 pp.

Fahnestock, R.K. (1969). Morphology of the Slims River. In *Icefield Ranges Research Project, Scientific results*, ed. V.C. Bushnell and R.H. Ragle. American Geographical Society, NY, and Arctic Institute of North America, Montreal, Quebec, **Vol. 1**, pp. 161-172.

Johnson, P. (1986). Holocene Paleohydrology of the St. Elias Mountains, British Columbia and Yukon. *Géographie physique et Quaternaire*, **40(1)**, 47-53.

Kouwen, N. (1988). WATFLOOD: A Micro-Computer based Flood Forecasting System based on Real-Time Weather Radar. *Canadian Water Resources Journal*, **13(1)**, 62-77.

Kouwen, N., Soulis, E. D., Pietroniro, A., Donald, J., and Harrington, R. A. (1993). Grouping Response Units for Distributed Hydrologic Modelling. *ASCE J. of Water Resources Management and Planning*, **119(3)**, 289-305.

Li, Y., Kurkute S. and Chen L. (2018). Projected Changes over Western Canada Using Convection-Permitting Regional Climate Model. In *31st Conference on Climate Variability and Change, 98th American Meteorological Society Annual Meeting*, Austin, Texas.

Pietroniro, A., Fortin, V., Kouwen, N., Neal, C., Turcotte, R., Davison, B., Verseghy, D., Soulis, E. D., Caldwell, R., Evora, N., and Pellerin, P. (2007). Development of the MESH modelling system for hydrological ensemble forecasting of the Laurentian Great Lakes at the regional scale. *Hydrol. Earth Syst. Sci.*, **11**, 1279-1294.

Pomeroy J.W., MacDonald M., Dornes P. and Armstrong R. (2016). Water Budgets in Ecosystems. In *A Biogeoscience Approach to Ecosystems*, ed. E.A. Johnson and Y.E. Martin, Cambridge University Press, **Ch. 4**, 88-132 pp.

Shugar, D. H., Clague, J. J., Best, J. L., Schoof, C., Willis, M. J., Copland, L., and Roe, G. H. (2017). River piracy and drainage basin reorganization led by climate-driven glacier retreat. *Nature Geoscience*, **10**, 370-375.

Skamarock, W. C., Klemp, J.B., Duhdia, J., Gill, D.O., Barker, D.M., Duda, M.G., Huang, X.Y., Wang, W., and Powers, J.G. (2008). A description of the Advanced Research WRF version 3. NCAR Tech. Note NCAR/TN-475+STR, 113 pp.

Smith, C.A.S., Webb, K.T., Kenney, E., Anderson, A., and Kroetsch, D. (2011). Brunisolic soils of Canada: Genesis, distribution, and classification. *Can. J. Soil Sci.*, **91(5)**, 695-717.

Soulis, E. D., Kouwen, N., Pietroniro, A., Seglenieks, F. R., Snelgrove, K. R., Pellerin, P., Shaw, D. W. and Martz, L. W. (2005). A framework for hydrological modelling in MAGS. In *Prediction in Ungauged Basins: Approaches for Canada's Cold Regions*, ed. C. Spence, J.W. Pomeroy and A. Pietroniro. Canadian Water Resources Association, pp. 119-138.

Soulis, E. D., Snelgrove, K. R., Kouwen, N., and Seglenieks, F. R. (2000). Towards closing the vertical water balance in Canadian atmospheric models: coupling of the land surface scheme CLASS with the distributed hydrological model WATFLOOD. *Atmosphere-Ocean*, **38(1)**, 251-269.

Uppala, S.M., Kållberg, P.W., Simmons, A.J., Andrae, U., Da Costa Bechtold, V., Fiorino, M., Gibson, J.K., Haseler, J., Hernandez, A., Kelly, G.A., Li, X., Onogi, K., Saarinen, S., Sokka, N., Allan, R.P., Andersson, Arpe, K., Balmaseda, M.A., Beljaars, A.C.M., Van de Berg, L., Bidlot, J., Bormann, N., Caires, S., Chevallier, F., Dethof, A., Dragosavac, M., Fisher, M., Fuentes, M., Hagemann, Holm, E., Hoskins, B.J., Isaksen, L., Janssen, P.A.E.M., Jenne, R., McNally, A.P., Mahfouf, J-F., Morcrette, J-J., Rayner, N.A., Saunders, R.W., Simon, P., Sterl, A., Trenberth, K.E., Untch, A., Vasiljevic, D., Viterbo, P. and Woollen, J. (2005). The ERA-40 re-analysis. *Quart. J. Meteo. Soc.*, **131**, 2961-3012.

Verseghy, D.L. (1991). CLASS – a Canadian land surface scheme for GCMs, I. Soil model. *Int. J. Climatol.*, **11**, 111-133.

Verseghy, D.L. (2000). The Canadian land surface scheme (CLASS): Its history and future, *Atmosphere-Ocean*, **38(1)**, 1-13

Verseghy, D.L., McFarlane, N.A., and Lazare, M. (1993). CLASS – a Canadian land surface scheme for GCMs, II. Vegetation model and coupled runs. *Int. J. Climatol.*, **13**, 347-370.

Wahl, H. (2004). Climate. In *Ecoregions of the Yukon Territory: Biophysical properties of Yukon landscapes*, ed. C.A.S. Smith, J.C. Meikle and C.F. Roots. Agriculture and Agri-Food Canada, PARC Technical Bulletin No. 04-01, Summerland, British Columbia, pp. 19-23.

Weedon, G. P., Gomes, S., Viterbo, P., Österle, H., Adam, J.C., Bellouin, N., Boucher, O. and M. Best, M. (2010). The WATCH forcing data 1958–2001: A meteorological forcing dataset for land surface and hydrological models. Technical Report No. 22, 41 pp.

Weedon, G. P., Gomes, S., Viterbo, P., Shuttleworth, W. J., Blyth, E., Osterle, H., Adam, J. C., Bellouin, N., Boucher, O., and Best, M. (2011): Creation of the WATCH forcing data and its use to assess global and regional reference crop evaporation over land during the twentieth century. *J. Hydrometeorol.*, **12**, 823–848.